

NASA Contractor Report 189688

**STRATOSPHERIC AIRCRAFT EXHAUST PLUME AND
WAKE CHEMISTRY STUDIES**

R.C. Miake-Lye, M. Martinez-Sanchez, R.C. Brown,
C.E. Kolb, D.R. Worsnop, M.S. Zahniser, G.N. Robinson
J.M. Rodriguez, M.K.W. Ko, R-L. Shia, N.D. Sze,
L. Fox, S.C. Wofsy, and P. Davidovits

**AERODYNE RESEARCH, INC.
Billerica, Massachusetts**

**Contract NAS1-19161
October 1992**



National Aeronautics and
Space Administration

Langley Research Center
Hampton, Virginia 23665-5225

(NASA-CR-189688) STRATOSPHERIC
AIRCRAFT EXHAUST PLUME AND WAKE
CHEMISTRY STUDIES (Aerodyne
Research) 109 p

N93-12299

Unclass

G3/46 0125232

TABLE OF CONTENTS

CHAPTER 1 - HSCT AIRCRAFT EMISSIONS DATA	1
SUMMARY	1
INTRODUCTION AND BACKGROUND	1
MEASUREMENT APPROACHES	3
NO _x ESTIMATION METHODS	5
EMISSION INDICES	7
AIRFRAME EMISSIONS	11
CONCLUDING REMARKS	15
ACKNOWLEDGMENTS	15
REFERENCES	15
CHAPTER 2 - PLUME AND VORTEX REGIME	
MODELING OF MIXING AND CHEMISTRY	18
SUMMARY	18
INTRODUCTION	18
PLUME MIXING AND CHEMISTRY	21
VORTEX WAKE DYNAMICS	26
SUMMARY AND CONCLUSIONS	40
ACKNOWLEDGMENTS	41
REFERENCES	41
APPENDIX A - BUOYANT TURBULENT JET IN A CO-FLOW	44
APPENDIX B - A MODEL FOR TURBULENT VORTEX RING EVOLUTION	45
CHAPTER 3 - LAGRANGIAN BOX MODEL OF	
WAKE DISPERSAL	48
INTRODUCTION	48
PHOTOCHEMICAL CALCUALTIONS	50
RADIATIVE CALCULATIONS	54
DISCUSSION AND CONCLUSIONS	55
REFERENCES	57
CHAPTER 4 - LABORATORY STUDIES OF	
STRATOSPHERIC HETEROGENEOUS	
CHEMISTRY	83
INTRODUCTION	83
PERTURBATIONS FROM AIRCRAFT EMISSIONS	85
OVERVIEW OF EXPERIMENTAL PROGRAM	85
HETEROGENEOUS KINETIC STUDIES	86
STRATOSPHERIC AEROSOL THERMODYNAMICS	92
CURRENT RESULTS AND STRATOSPHERIC	
IMPLICATIONS	97
RELEVANCE OF EXPERIMENTAL RESULTS TO	
STRATOSPHERIC FLIGHT	100
REFERENCES	101

Chapter 1

HSCT Aircraft Emissions Data*

SUMMARY

Estimates are given for the emissions from a proposed High Speed Civil Transport (HSCT). This advanced technology supersonic aircraft would fly in the lower stratosphere at a speed in the range of roughly Mach 1.6 to Mach 3.2 (470 to 950 m/sec or 920 to 1850 knots). Because it would fly in the stratosphere at an altitude in the range of 15 to 23 km commensurate with its design speed, the potential exists for its exhaust effluents to perturb the chemical balance in the upper atmosphere. The first step in beginning to determine the nature and magnitude of any chemical changes in the atmosphere due to these proposed aircraft is to identify and quantify the chemically important species they emit.

This chapter summarizes relevant earlier work dating back to the Climatic Impact Assessment Program (CIAP) studies of the early 1970's and current propulsion research efforts at NASA and at its High Speed Research Program (HSRP) contractors' laboratories. Recent work funded by HSRP is providing estimates of the chemical composition of an HSCT's exhaust and these emission indices (EIs) are presented. Other aircraft emissions that are not due to combustion processes are also summarized and these emissions are found to be much smaller than the exhaust emissions. It is anticipated that future advances in propulsion technology, in experimental measurement techniques, and in understanding of upper atmospheric chemistry may affect these estimates of the amounts of trace exhaust species or their relative importance, and revisions are expected to become necessary in the future.

INTRODUCTION AND BACKGROUND

The upper atmosphere has been perturbed by anthropogenic chemicals. Most notable of these are the chlorofluorocarbons (CFCs), which are implicated in the depletion of stratospheric ozone and the creation of the Antarctic ozone hole. Because of the variety of technical advantages they offered, these chemically inert species were developed for industrial processes and consumer products before it was realized that they were *photo*-chemically reactive in the upper atmosphere. While an understanding of the detailed chemical balance and how it is affected by perturbations due to pollutants is still being developed, it is with an awareness of actual anthropogenic effects on the stratosphere that the exhaust emissions from the proposed HSCTs are being analyzed.

The exhaust species under most scrutiny at present are the oxides of nitrogen, NO and NO₂, collectively denoted NO_x. The potential for catalytic destruction of ozone by exhaust NO_x in the stratosphere was recognized¹ in the early 1970's when the U.S. supersonic transport (SST) was being studied. The Climatic Impact Assessment Program (CIAP) was undertaken to consolidate and extend existing knowledge of the chemistry, physics, and technology of supersonic flight in the stratosphere and the effects of the consequential exhaust emissions. The results and conclusions of that program are summarized in its proceedings²⁻⁵ and monographs⁶⁻¹¹. The state of knowledge and technology on the present subject of aircraft emissions as of 1975 is represented in the Second Monograph⁷ on 'Propulsion Effluents in the Stratosphere'.

* This chapter also is published as Chapter 2 of NASA Reference Publication 1272, "The Atmospheric Effects of Stratospheric Aircraft: A First Program Report"

Aircraft propulsion technology has advanced in the intervening years such that the reasons the U.S. SST was not considered viable can now be addressed with technical improvements¹²⁻¹⁴. The evolution of such technically improved engines has actually made NO_x reduction more difficult as the combustor pressure and temperatures have risen to improve propulsion efficiency. Yet reduction of NO_x levels below that achieved with SST-era technology appears to be necessary to avoid large stratospheric ozone depletion. In order to do this, combustors must be improved, requiring the results from current research aimed at controlling local temperatures and equivalence ratios throughout the combustion process. A pivotal question concerns the quantitative effects on the atmosphere of the reduced levels of exhaust trace species emitted from the advanced technology propulsion systems that would power the proposed HSCT.

The understanding of stratospheric chemistry and transport has also made enormous strides. The role of heterogeneous chemistry, in particular, was not apparent when commercial stratospheric flight was last considered. An awareness of chemistry on the surface of condensed water and/or condensed aqueous solutions has grown out of the need to understand the Antarctic ozone hole. Now this heterogeneous chemistry must be accounted for in the global stratospheric chemical balance, but also must be assessed for a possible role in the wake of stratospheric aircraft. In the aircraft wake, the locally high (relative to ambient concentrations) trace species concentrations may encounter condensed water in the condensation (contrails) in the exhaust behind the aircraft.

Additional data concerning condensation nuclei (CN) emitted by the aircraft are needed to understand the possible role of heterogeneous chemistry, both globally and in the wake. These CN are essential for the formation of contrails and their number density affects the contrail particle sizes and number densities. The chemical nature of the CN surfaces control their ability to condense water, newly formed soot typically having a small fraction of its number density as active CN.

CN in the form of ambient condensed sulfate particles, exhaust carbonaceous soot particles, and possibly other exhaust particulates are necessary to initiate the condensation process that can occur under some conditions in the proposed stratospheric flight paths. Measurements of CN number densities and knowledge of their condensation properties are necessary to predict droplet lifetimes and settling distances and thus their role in wake chemistry and transport and in global stratospheric aerosol loading.

Once a condensed surface is present, additional chemical species must be accounted for, and additional chemical reactions occurring on the condensed phase/vapor interface must be introduced in the overall chemical balance. HNO₃ and N₂O₅ formed by further reactions of NO_x, have been shown to figure prominently in the heterogeneous chemistry occurring in polar stratospheric clouds (PSCs) that drives the Antarctic ozone hole. These species could also react with aerosols in the contrail if and when concentrations of species and particles are sufficiently high for long enough times.

The list of chemically relevant exhaust species now goes beyond the major combustion products of CO₂ and H₂O and the trace species NO_x. A fuller set of 'odd-nitrogen' compounds termed NO_y, including NO_x, NO₃, N₂O₅, HNO₃, and (although not an exhaust species) ClONO₂, must be considered as aerosol-active species, as well as SO₂ and soot particles. The total unburned hydrocarbons (THC) and CO in the exhaust represent combustion inefficiencies and play a role in important stratospheric HO_x (OH, HO₂) chemistry.

The measurement techniques used to measure these species will be discussed in the next section followed by a brief summary of how engine emissions are being projected for the next generation of low NO_x , sustained supersonic propulsion systems. The projected estimates will be discussed in a following section and compared with past measurements on related, predecessor engines. Finally, a set of estimates for emissions from the aircraft that are not due to the propulsion system will be reviewed.

MEASUREMENT APPROACHES

Quantitative measurements of exhaust emissions are carried out only in ground-based facilities. In fact, emissions have rarely been measured during aircraft flight, and only qualitative results were obtained¹⁵⁻¹⁷. Ground-based measurements of entire engines must be performed in a test facility that can reproduce ambient conditions, including pressure and temperature, if quantities appropriate to high altitude flight are to be measured. Such tests are exceedingly expensive¹⁸ and require considerable preparation and support, so there is strong motivation to perform simpler measurements on components of the engine separately in smaller laboratory based facilities.

Primarily, these simpler measurements consist of reproducing the flow conditions in a trial combustor or a simplified version of one and making measurements at its exit. The flow into and out of the combustor can be calculated reliably for a chosen engine cycle. The more benign conditions encountered during laboratory component testing increase the accuracy of individual measurements.

Most gaseous species are measured using continuous sampling probes that take a small flow of the exhaust gases from the component to the measurement instrument, controlling the temperature and flow velocity, and thus the delay to measurement. The species currently being measured routinely include CO_2 , H_2O , CO , NO , NO_2 , SO_2 , and the total unburned hydrocarbons (THC)¹⁹⁻²⁰, both as an undifferentiated sum of total C as well as individual hydrocarbon species in more detailed batch sampling studies²¹⁻²³. Batch samples are analyzed using gas chromatography and/or mass spectroscopy to quantify the various hydrocarbon species present, as well as H_2 , O_2 , N_2 , CO , and CO_2 . Particulates in the form of carbonaceous soot have been a concern for decades; originally attempts were directed toward reducing the visible smoke leaving with the exhaust. These particulate emissions have typically been reported as an SAE 'smoke number' (SN)²⁰ that can be related to total particulate mass fairly reliably²⁴ but, when particle size distributions, number densities, and CN-activity are needed, this measurement approach is not adequate. More detailed sizing measurements have been performed²⁵, but are not routine.

Chemiluminescence detectors have been used to measure NO as well as NO_x . For NO_x measurements, the NO_2 fraction of the NO_x is first converted to NO and the chemiluminescence generated when the net NO reacts with ozone is quantified¹⁹. NO_2 is determined from the difference between an NO measurement and the corresponding NO_x measurement. NO_x measurements have conventionally been reported as the total mass of NO_2 plus the mass equivalent of NO oxidized to NO_2 . Thus NO_x is conventionally reported as the NO_2 gram equivalent of the total measured species^{19,26}, independent of the oxidation state (even though it is typically mostly NO near the exit of gas turbine engines). This convention, unfortunately, has not always been stated explicitly, generating some confusion in interpreting these numbers in the broader community. In this chapter, NO , NO_2 , and NO_x emissions will all be reported as gram equivalents of NO_2 . Generally, other NO_y species (e.g. HNO_3) have not been measured to determine if significant levels are present.

While chemiluminescent NO_x measurements have been and continue to be the standard NO_x measurement technique, ultraviolet absorption measurements of NO were made as part of the CIAP program²⁷. A large discrepancy was observed between NO measured using absorption and NO_x quantified by collecting exhaust with a relatively crude probe and analyzing it with a chemiluminescent instrument; the UV absorption being up to 4-5 times larger than the chemiluminescent NO_x measurement²⁸. This discrepancy was largest in high temperature and high velocity flows such as would be encountered in the supersonic exhaust from any HSCT engine. Improvements in probe design and line-of-sight measurement methods may allow these differences to be resolved, but a quotable reference study addressing the discrepancies between optical and sampling measurements appears to be lacking. Given the need for accurate and reliable emissions estimates required for modeling the stratospheric impact of these vehicles, these differences must be understood and an optimal measurement strategy adopted.

Flame ionization has been used to quantify the total unburned hydrocarbons (THC), while non-dispersive infrared techniques are used to measure CO, CO_2 , and water vapor¹⁹. SO_2 is directly related to the sulfur content of the fuel and thus is not controlled by combustor design. When SO_2 is measured, a non-dispersive ultraviolet technique is employed. The SAE SN is measured for particulates emissions by collecting particles as a known volume exhaust sample is drawn through a filter and quantifying the change in the filter's reflectance²⁰.

Radical species, particularly OH, may be chemically active in the exhaust leaving the engine nozzle. Although it is not one of the standard exhaust species usually reported, superequilibrium OH concentrations were measured in the exhaust of a turbojet for supersonic flight conditions during CIAP²⁷. The observed superequilibrium ratio was large (> 10) in non-afterburning operation, while near unity for afterburning cases. Thus OH concentrations and chemical effects are expected to be dependent on engine configuration and cycles (duct-burning versus turbofan/turbojet). If an important role in exhaust chemical processing of NO_y and CN is established, some reliable measurement of OH would be necessary.

The measurement of a species in the exhaust flow determines its local concentration or mass fraction, but with the variety of combustor designs, engine cycles and bypass ratios being considered for these engines, different amounts of air end up in the exhaust for a given fuel flow rate. It has been convenient to normalize the emission rate, on a mass basis, of a given species by the mass flow rate of fuel. Thus an emission index (EI X) is defined as

$$\text{EI}_{(Y)X} = \frac{(\text{g/s species X})}{(\text{kg/s fuel})} \quad (1)$$

Emissions expressed as volume fractions require conversion using species molecular masses¹⁹ in order to arrive at an EI. For nearly complete combustion, calculation of an emission index effectively normalizes by the rate of enthalpy addition to the air as it passes through the engine.

The preceding subscript (Y) is not a standard notation but will be used in this chapter to indicate that the emission index of species X is being reported as the mass equivalent of species Y. This notation resolves any possible ambiguities associated with reporting NO_x EIs and allows the reporting convention in terms of NO_2 to be explicitly indicated. THC is also a mixture of compounds and its EIs are reported in terms of CH_2 , CH_α (where α is the fuel atomic hydrogen/carbon ratio)¹⁹,

or CH_4 – the latter will be used here. A missing preceding subscript for a pure species will be taken to mean that its EI is in terms of its own mass, i.e. Y is identical to X. Clearly, EIs can only be meaningfully summed if the subscripts match.

It is worth emphasizing that the normalization used in defining the EI does not account for propulsion efficiency and so does not represent the best overall reduction of net emissions from an engine. For instance, if a particular scheme reduced $\text{EI}_{(\text{NO}_2)} \text{NO}_x$ by 10% but required 15% greater overall fuel flow rate to achieve the same thrust, there would be a penalty due to both poorer fuel consumption and greater emissions. The Environmental Protection Agency Parameter (EPAP) for landing-takeoff cycle conditions²⁹ represents a means of including the propulsion performance in the emissions estimation method. A similar approach could be used to compare engines in supersonic cruise operation for HSCT stratospheric impact assessment.

Further, the total performance of the aircraft is not being considered – the most likely relationship being a greater aircraft weight resulting from emission reduction procedures^{12–14}. Greater aircraft weight translates into more fuel burned and thus an increase in net emissions for a given EI. Thus, the net emissions from an HSCT will depend on the total aircraft design, not simply on an EI. On the other hand, combustor design will be optimized by lowering the important EIs and, since improved combustor design will lower NO_x emissions for any given propulsion system or airframe configuration, lowering EIs is a key factor in improving the overall emissions performance of an aircraft.

NO_x ESTIMATION METHODS

Extensive NO_x emissions measurements have been performed over the years on many existing engines and engine components. Development work is proceeding towards a 'low NO_x ' HSCT combustor, but a complete prototype engine is still a long way from the test cells. Estimates for the expected emission performance of a given design are calculated by using semi-empirical correlations that have been developed and refined throughout the past emission measurement programs. These correlations account for the experimentally observed pressure and temperature dependences of the net NO_x emission for a given combustor. Insofar as changes in combustor design do not alter the overall chemical kinetics, the correlations can be used to guide the combustor development efforts.

The essentially square-root dependence of $\text{EI}_{(\text{NO}_2)} \text{NO}_x$ on combustor pressure and the exponential dependence on combustor inlet temperature were used in correlations for CIAP work and current correlations have evolved from them. Over the range of combustor designs measured to date, these dependencies have been demonstrated to fit the observed data well, with a single multiplicative coefficient reflecting a given combustor's overall emission performance. For example, GE Aircraft Engines uses a correlation:

$$\text{EI}_{(\text{NO}_2)} \text{NO}_x = 0.0986 \left[\frac{p_3}{1 \text{ atm}} \right]^{0.4} \exp \left(\frac{T_3}{194.4 \text{ K}} - \frac{H_0}{53.2 \text{ g H}_2\text{O/kg dry air}} \right) \quad (2)$$

for their 'dual annular' low NO_x combustor for the NASA ECCP³⁰ clean combustor program. In the correlation, p_3 is the combustor inlet pressure, and T_3 is the combustor inlet temperature. The effect of ambient humidity, H_0 in grams of water per kilogram dry air, is to reduce NO_x production but at the low humidity levels encountered in the stratosphere, this correction will be

negligible. GEAE's previous combustors used in the CF6 series engines are also approximated by this correlation with the multiplicative constant (0.0986) increased by 25% and a constant value of 2.2 added to the entire expression for the CF6-80C, and a 35% increase and 1.7 added for the CF6-50C.

The coefficient of GEAE's correlation is affected by the specific combustor design, including the residence time that a parcel of reacting fluid remains within the combustor. This particular effect is included parametrically in the correlations of Pratt and Whitney and NASA by referencing a representative combustor velocity. These two correlations are the same except that NASA's does not correct for water vapor effects and both include a reciprocal reference velocity, V_{ref} , dependence appropriate to the combustor flow and a dependence on T_4 , the combustor exit temperature, reflecting the temperature rise due to combustion heat release.

$$EI_{(NO_2)} NO_x \sim \frac{p_3^{0.5} T_4}{V_{ref}} \exp\left(\frac{T_3}{288 \text{ K}} - \frac{H_0}{53.2 \text{ g H}_2\text{O/kg dry air}}\right) \quad (\text{P\&W}) \quad (3)$$

$$EI_{(NO_2)} NO_x \sim \frac{p_3^{0.5} T_4}{V_{ref}} \exp\left(\frac{T_3}{288 \text{ K}}\right) \quad (\text{NASA LeRC}) \quad (4)$$

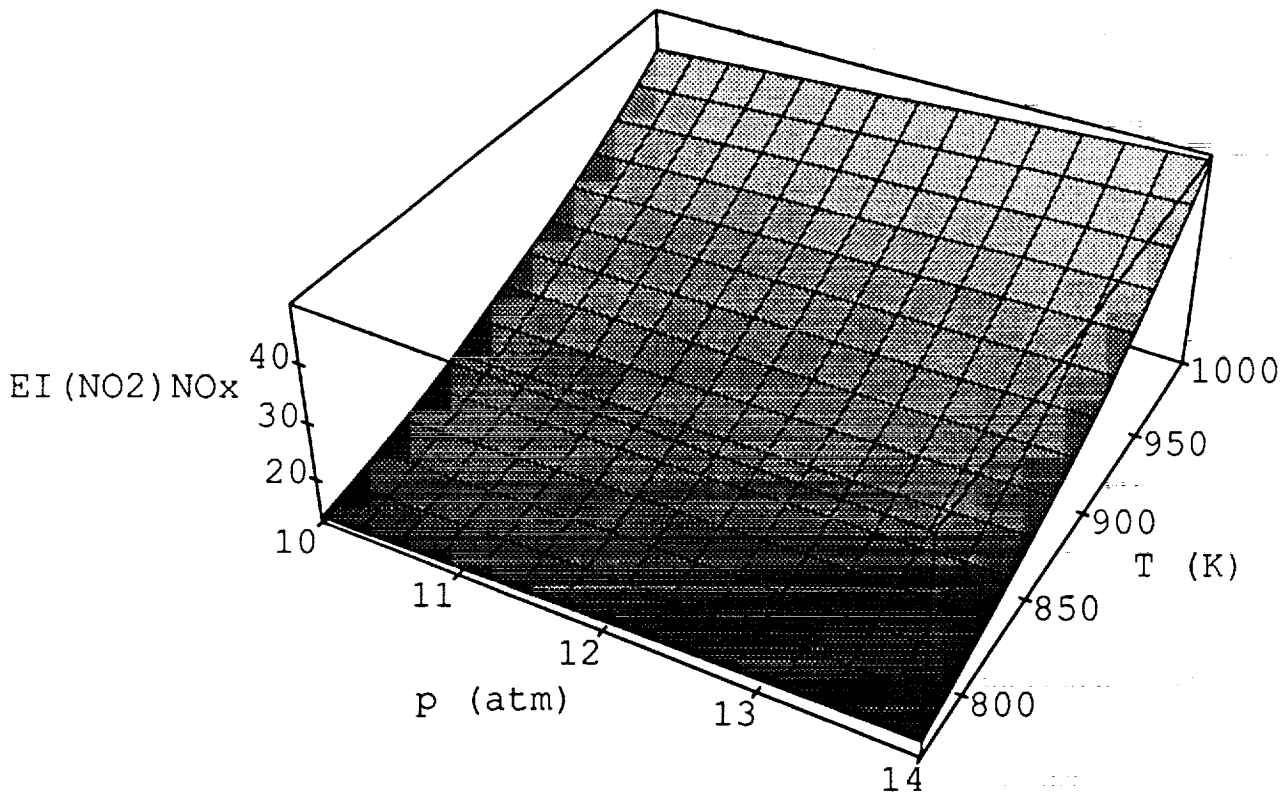


FIG. GEAE's correlation of $EI_{(NO_2)} NO_x$ as a function of $10 \text{ atm} \leq p_3 \leq 14 \text{ atm}$ and $770 \text{ K} \leq T_3 \leq 1000 \text{ K}$ for the ECCP technology combustor.

The general functional dependence of these correlations is shown in the figure below, where $EI_{(NO_2)}NO_x$ is plotted using the GEAE correlation for pressures from 10 to 14 atmospheres and temperatures between 770 K and 1000 K. Pratt and Whitney's and NASA's correlations have a similar functional form for reasonable values of T_4 , allowing for the combustion heat release and overall equivalence ratio. For $T_4 \sim T_3 + 1100$ K, a multiplicative constant can be chosen for the P&W/NASA correlation so that the temperature and pressure dependences agree with the GE correlation within 5-10%.

For estimating $EI_{(NO_2)}NO_x$ for the Lean, Premixed, Prevaporized (LPP) combustor, GEAE uses the correlation³¹:

$$EI_{(NO_2)}NO_x = t_{res} \exp \left(-72.28 + 2.8 T_{adia}^{0.5} - \frac{T_{adia}}{38.02} \right) , \quad (5)$$

where t_{res} is the combustor residence time in ms and T_{adia} is the adiabatic flame temperature in Kelvins.

These correlations are used to estimate the emissions performance of a combustor for conditions that have yet to be tested. Indeed, the most promising candidate NO_x reduction schemes have not yet been tested at the conditions expected in HSCT combustors. Promising experiments³² indicate that advanced combustor concepts may achieve significant reductions at p_3 , T_3 appropriate to HSCT engine cycles. However this indication is based on experiments at less severe operating conditions extrapolated to the desired p_3 , T_3 . Future experiments will clarify the performance on this combustor approach at the anticipated HSCT conditions and further test the correlations for an as yet uncalibrated technology.

EMISSION INDICES

Emission indices were measured for several engines intended for supersonic flight during the 1970's^{18,33,34}. The results of some measurements from this time period are tabulated below. Included are measurements of the one supersonic civilian transport that has operated commercially, the Olympus engine of the Concorde airplane. An important distinction must be made in comparing these emission indices to those calculated for the proposed HSCT engine. The increased propulsion efficiency inherent in the designs for the HSCT dictate higher combustor inlet temperatures (and pressures) than were used in the 1970's engines. The NO_x produced at these more severe conditions would be much higher than that measured in these earlier engines if the same combustor technology was used. Substantial improvements in the combustor design; improving the mixing, controlling the local equivalence ratio, and minimizing the residence time; are required to decrease the NO_x emissions relative to these engines while simultaneously maintaining the higher operating pressure ratios, and thus combustor inlet temperatures, necessary for the required cycle efficiency.

Also in the table included are emissions measurements for two afterburning military turbojet engines^{18,33,34}. The measurements for the J58 engines were in preparation for the YF-12 in-flight NO_x field measurements. The study of these engines demonstrated trends of EIs versus altitude, fuel-air ratio, Mach number, and the presence or absence of afterburning for a specific engine. The optimized design of an engine designed to fly within a narrow range of flight conditions may not necessarily reflect all of these trends, however.

While it is significant that $EI_{(NO_2)NO_x}$ was reduced by a factor of ~ 2 during afterburning operation, this cannot be employed as a reduction method for HSCT propulsion. The reduction is due to the afterburning fuel being consumed at lower pressure and temperature after expansion through the turbine, but this is coupled to increased EI CO, EI THC, and, most notably, substantial increases in specific fuel consumption and possibly more total NO_x produced. Increases in specific fuel consumption, in particular, could not be tolerated for sustained supersonic cruise in an economically viable commercial aircraft.

TABLE 1

Measured 1970's Supersonic Engine Emission Indices			
Species	Olympus 593 ¹⁸	YJ93-GE-3 ¹⁸	J58 ^{33,34}
CO	1.4 – 4.6	3.4 – 38.7	1 – 120
$(NO_2)NO_x$	17 – 20	1.81 – 12.03	2 – 20
$(NO_2)NO$	16 – 19	1.83 – 10.69	
NO_2	0.2 – 1.3		
$(CH_4)THC$		0.03 – 0.8	0.03 – 12

Pratt and Whitney's calculated emissions performance for their proposed Turbine Bypass Engine (TBE)³⁵ is included in Table 2. General emissions levels are given, but engine cycles have been optimized to different degrees for each case so, for example, the fact that $EI_{(NO_2)NO_x}$ is slightly greater for Mach 2.4 should not necessarily be construed as greater NO_x emissions for that case. The changes in CO_2 and H_2O emissions at Mach 3.2 relative to the lower speeds are due to a fuel change. The higher velocity flight conditions require a different fuel (JP-7 instead of the more commonly used Jet A) with a higher thermal stability and a concomitant increase in the H/C and H_2O/CO_2 ratios. The soot/particulate EI is calculated from the SAE Smoke Number, which is a quantitative measure of particulate emissions but is not directly based on the emitted particulate mass²⁰.

TABLE 2

Pratt and Whitney Estimates for Engine Emission Indices ³⁵			
Species	Mach 1.6 18.3 km	Mach 2.4 19.8 km	Mach 3.2 21.3 km
CO ₂	3165.5	3165.5	3117
H ₂ O	1233	1233	1350
CO	1.1	1.3	1.9
(NO ₂)NO _x	5.3	6.4	5.1
(NO ₂)NO	4.5	5.4	4.3
NO ₂	0.8	1.0	0.8
SO ₂	1.0	1.0	1.0
soot/particulates	0.02	0.02	0.02
(CH ₄)THC	0.1	0.1	0.2
SAE Smoke Number	18.4	19.7	14.0
Fuel	Jet A	Jet A	JP-7

The calculated emissions performance of GE Aircraft Engines' Variable Cycle Engine³⁶ (VCE) is quantified in Table 3. The NO_x emissions were based on the correlation of *eqn. 5*.

TABLE 3

GE Aircraft Engines Estimates for Engine Emission Indices ³⁶		
Species	Mach 2.4 16.8 km	Mach 3.2 21.3 km
CO ₂	3156	3135
H ₂ O	1240	1290
CO	< 5	< 6
(NO ₂)NO _x	5.7	7.0
(NO ₂)NO	5.1	6.3
NO ₂	0.6	0.7
SO ₂	1.2	1.2
soot/particulates	-	-
(CH ₄)THC	< 0.1	< 0.1
SAE Smoke Number	«1	«1
Fuel	Jet A	JP-7

MTU Motoren- und Turbinen-Union in Munich Germany estimates emissions performance of HSCT engines³⁷ for both existing technology and expected future technology as indicated in Table 4.

TABLE 4

MTU Estimates for Engine Emission Indices ³⁷		
Species	Mach 2 14.8 – 18.2 km	Mach 3 19.9 – 23.6 km
Advanced Proven Technology		
CO	4.0	4.0
$(NO_2)NO_x$	26 – 21	19 – 15
$(CH_4)THC$	0.4	0.4
Future Technology (15 to 20 years)		
CO	2.6	2.6
$(NO_2)NO_x$	11 – 9	8 – 7
$(CH_4)THC$	0.3	0.3

In CIAP, consensus predictions were formulated³⁸ for exhaust emissions for anticipated emission reduction technologies to be used in the SST program. Those predictions were for technological development that was never pursued to the demonstration of its potential. However, they serve as a point of reference for current predictions and are included in Table 5. The last column in Table 5 gives the range of emission indices being considered for preliminary assessments.

TABLE 5

Estimates for HSCT EIs in the Stratosphere			
Species	CIAP Turbojet ³⁸	CIAP Duct-burning ³⁸	HSRP/AESA Current Range
CO_2			3120 – 3170
H_2O			1230 – 1350
CO	3	15 – 30	1.1 – 6
$(NO_2)NO_x$	3 – 14	3 – 12	5 – 50†
$(NO_2)NO$			4 – 45†
SO_2			0 – 1
soot/particulates	0.02	0.02	—
$(CH_4)THC$	0.1 – 0.5	3 – 10	<0.1 – 0.2

† The upper value represents existing proven technology that is not likely to be used in its current form in a future HSCT aircraft.

The range of CO_2 , and H_2O emissions are purely a function of fuel composition – changes in these emissions are related to changes in fuel composition that increase its thermal stability as becomes necessary around Mach 3. SO_2 is also a function of the fuel itself – all the fuel sulfur is emitted as SO_2 . CO and THC emission estimates will have a broad range as long as both duct burning and unaugmented turbojet or low-bypass turbofan options are being considered, but are nonetheless bounded by fuel consumption constraints for an economically viable vehicle.

NO_x emissions have the greatest range, as well as the greatest possibilities for control within the operational envelope that an HSCT will function. The upper limit is conservative, in the sense that it uses an estimate made with the GE correlation for the GEAE/NASA ECCP combustor for which measurements have been made. The low value of 5 is not a firm prediction of future technology, but rather an HSRP goal. These low values make use of extrapolations employing the correlations and basic laboratory data, sometimes using gaseous fuel experiments³¹, to estimate the best performance foreseeable at this time. It is hoped that, in the course of the current HSRP effort, these ranges in particular can be narrowed.

AIRFRAME EMISSIONS

The exhaust from the engines is the largest quantity of material left in the flight path by an airplane. However, the exhaust species that are directly involved in ozone chemistry are trace species. Because they comprise a small fraction of the total exhaust mass, the relative amounts of other minor emissions from the proposed HSCT need to be quantified to evaluate their potential contribution to the total aircraft emissions. These additional airframe emissions, as distinguished from the engine emissions contained in the exhaust, originate from 1) aircraft systems involved in controlling or supporting flight operations and 2) passenger systems providing services onboard. Estimates for these two classes of emissions for an HSCT will be made in the following subsections.

The various fluids carried on the aircraft could potentially leak from the vehicle and find their way into the atmosphere. In making the following estimates, some worst-case assumptions will be made by assuming that an estimate for a fluid loss corresponds to an emission into the stratosphere. In fact, lost fluid could remain primarily within the aircraft, and that which escapes may do so when the plane is on the ground or during takeoff, landing, or while passing through the troposphere. The emissions escaping the vehicle at high altitude cruise could settle out of the stratosphere without vaporizing at the low temperatures (200-250 K) encountered. The estimates given are intended to provide a crude upper bound for the quantities of these species that might be released in the stratosphere. If any of these estimates suggest that an airframe emission species is important to stratospheric chemistry, more refined quantitation would be required to model its effects.

Since the exhaust emissions are reported as emission indices (EIs) in grams of emitted species per kilogram fuel burned, a comparison of those exhaust EIs and the aircraft emissions requires a correspondence relating these two quantities. Aircraft emissions are not caused by the consumption of fuel in any direct sense, but rather are associated with 1) routine operation and thus flight time or number of flights, or 2) random, unusual events with some small frequency of occurrence. Conversion of these aircraft emissions to an equivalent emission index (EEI) will be made by using an estimate of the fuel burn rate appropriate for the generalized design of a Mach 2.4 HSCT aircraft and making the conversion from time to fuel mass.

Aircraft Systems

All the mechanical and electrical systems needed to control an HSCT in flight have not yet been designed in detail, so the amounts of materials carried onboard or used during operation cannot be specified. Corresponding quantities from existing aircraft cannot be substituted without qualification, since particular systems can be very configuration dependent; beyond that, the HSCT is a substantially different vehicle from a subsonic aircraft, thus its systems may differ significantly

from those aircraft for which quantities are available. On the other hand, the types of systems needed are basically the same as those currently in use, and available information on existing aircraft can be used to provide crude estimates of emissions due to these sources.

The most ample fluid carried is, of course, the engine fuel. The economical use of fuel is a driving criterion in designing the aircraft, so little unburned fuel is allowed to escape the aircraft. Fuel is dumped very occasionally if too much is being carried for a safe landing, but this is an emergency measure carried out when approaching a landing and the aircraft is below about 2 km. Thus, fuel is not dumped in the stratosphere. Fuel tanks may be vented during flight, releasing some vaporized fuel, and this may be a bigger factor for a supersonic aircraft with significant skin heating than it is for subsonic aircraft, but no estimate for such vapor loss has yet been obtained.

Hydraulic fluid is used to control mechanical devices in the aircraft, and regular maintenance requires replenishing the hydraulic system reservoirs. Boeing³⁹ estimates that regular seepage or leakage amounts to 20 gallons (70 kg) of hydraulic fluid (composed of phosphate esters) lost from the hydraulic systems per year per airplane. In addition, aircraft are designed with redundant hydraulic systems to ensure control should one system fail. Failures are rare events, even so; an estimate of an average loss rate by Boeing³⁹ is 1 gallon (3 kg) per year per airplane due to system failure. (This is based on a loss of 6 gallons of fluid on average in an event that occurs 50 times in 10^6 flight hours, as extracted from reliability reports for existing subsonic commercial aircraft, and 3311 flight hours per year per airplane for these subsonic transports.) While it will be assumed that these 70 kg per year per airplane (or 2×10^4 kg/ 10^6 flight hours) of phosphate esters are deposited in the stratosphere, for the low vapor pressure hydraulic fluids especially, it is not likely that this emission could appear in the stratosphere as a chemically reactive species.

Oil is used as a lubricant for the engines, as well as some auxiliary devices; infrequently some oil is discharged due to accidental leaks. Some oil/air mist may be vented from the oil reservoir tanks⁴⁰. Some oil is consumed within the engine, as well – some of it being burned in the combustor, some exiting with the exhaust. The emissions due to oil consumed within the engine would be quantified in a measurement of the total exhaust emissions and thus really represent an engine emission indiscernible from the emissions due to fuel consumption. It is worth noting however, that as an engine ages, changes in oil consumption may result in changes in exhaust emissions as well.

Accidental leakage of oil, like hydraulic fluid, will not necessarily leave the aircraft, nor will that which leaves necessarily remain in the stratosphere. However, as an upper bound, Boeing³⁹ quotes a value of 5 incidences in 10^6 flight hours releasing on average 20 kg of oil. This amounts to a loss of 0.3 kg per year per aircraft of a fluid composed primarily of long chain aliphatic hydrocarbons with trace additives of phosphate esters and metal compounds.

Other less quantifiable emissions⁴¹ could arise from the venting of the lead-acid and/or nickel-cadmium batteries used for reserve power; this would result in negligible amounts of H₂ and O₂ being released. (Emissions due to mists of KOH and H₂SO₄ electrolytes would be even smaller and not likely to leave the aircraft.) Auxiliary power units (APUs) are small gas-turbine engines that would not be used in cruise typically and would emit much smaller amounts of exhaust not unlike the main engines. Windshield washer fluid is more likely to be used at lower altitudes, and the glycol solution used is unlikely to amount to even a small fraction of the 'blue ice' emissions

(see below). Finally, novel anti-icing techniques may make use of glycol solutions that would be carried on board, although not used in the stratosphere above hazardous clouds, but emissions due to this fluid, too, are not expected to amount to any more than the 'blue ice' fluids at stratospheric altitudes.

Passenger Systems

A variety of systems within the airplane's cabin are devoted to serving the passengers on board. Several refrigeration systems are typically available for air conditioning, refrigeration of food and drink in the galley, and sometimes cooling of avionics (more correctly an aircraft system need). Until replacement refrigerants are found, these systems will contain CFCs, and any leakage that exits the aircraft in the stratosphere will be depositing CFCs where they are photochemically active. Douglas⁴¹ estimates that 0.2 kg per year per airplane is typically used to maintain a representative aircraft's refrigerant systems.

Galley cooling and avionics cooling do not necessarily require CFC-based refrigeration (recirculating liquids are currently employed in some situations), so the amount of refrigerant aboard a yet-to-be-developed airplane could be minimized, if direct deposition in the stratosphere must be minimized. In a similar vein, fire extinguishers on current aircraft contain halons⁴¹ – a source of bromine and chlorine when photochemically activated in the stratosphere. Whether there is any greater risk due to stratospheric flight with CFCs and halons (or their replacements) than flight in the upper troposphere with existing aircraft would determine the need for replacement or closer control of leaks and accidental release on board an HSCT. For long-lived halocarbons, release in the lower stratosphere is not substantially different from release at the surface.

Lavatory holding tanks have received some media attention over the past several years as a result of mishaps attributed to 'blue ice' – lavatory fluid that has leaked from the holding tank due to faulty maintenance, frozen in the cold atmosphere, and then broken free. This has caused damage to the aircraft by being ingested in the engine or to property on the ground from impact. From the point of view of safety, this is a major problem and efforts have been directed at totally eradicating any possibility of leakage. As far as emissions are concerned, the low (and probably decreasing) frequency of occurrence and the likely substantial descent before complete vaporization suggest that lavatory fluids will not contribute to the total aircraft emissions in the stratosphere. Based on 1 incident involving 30 kg per 10^6 flight hours, Boeing³⁹ estimates that less than 1 cup of fluid is lost per year per aircraft using current reliability data.

For subsonic aircraft, oxygen service is available for passengers 'in the event of sudden loss of cabin pressure'. While this service is seldom used, some system leakage might occur from gaseous systems⁴² (used for crew and perhaps passengers for high altitude flight). Chemical O₂ generation packs⁴³ as used in many subsonic airplanes would only emit during use. Purity requirements for passenger respiration units limit Cl, CO, and CO₂ levels to 0.1, 20, 1000 ppmv respectively, so even if used, only oxygen with trace impurities is released. However oxygen is a major atmospheric constituent and even a major release of gas from the emergency oxygen system could not affect stratospheric chemistry. The substantially lower static pressures in the stratosphere necessitate more sophisticated depressurization safety measures for HSCTs. Potential emissions from such safety systems must be evaluated, particularly if they use fluids not already used in other systems.

Calculation of Equivalent Emission Indices for Airframe Emissions

To compare the amounts of these airframe emissions with those from the engine, an equivalent emission index will be defined. Simply, the average emission amount in grams released in a given flight time will be divided by the total amount of fuel used during cruise in the same time period, i.e.

$$EEI_X = \frac{\text{average emission rate of } X \text{ g/s}}{\text{fuel burn rate kg/s}} \quad (6)$$

Using the total of 3311 flight hours per year per aircraft for the existing subsonic aircraft (as used above) to arrive at a mean emission rate from the subsonic reliability data and taking a fuel burn rate of 9 kg/s as representative for Mach 2.4 flight, the emission estimates noted above can be converted to EEIs for HSCT cruise and are listed in Table 6. Note that a similar value of 3100 stratospheric flight hours is considered representative for HSCT flight³⁹ as well. Again, it is assumed that all the lost fluids are emitted and vaporized in the stratosphere, which in many of these cases is not likely to happen and so these quantities should be interpreted as upper bound estimates.

TABLE 6

Upper Bound Estimates for Airframe Emissions in the Stratosphere		
Emission	kg / 10 ⁶ flight hours	Equivalent Emission Index
Aircraft Systems		
lubrication oil burst	1×10^2	3×10^{-6}
hydraulic fluid burst	1×10^3	3×10^{-5}
hydraulic fluid leaks	2×10^4	5×10^{-4}
fuel dump	n/a†	n/a†
fuel vent	no estimate	no estimate
Passenger Systems		
refrigerants	1×10^2	4×10^{-6}
'blue ice'	30	1×10^{-6}

† Not Applicable. Fuel is not dumped at stratospheric altitudes. Corresponding tropospheric quantities would be 3×10^6 kg / 10⁶ flight hours, EEI = 0.1³⁹.

Referring to Tables 2-4, it is apparent that the largest stratospheric airframe emission is substantially smaller than the smallest engine emission and several orders of magnitude smaller than NO_x emissions. Recalling that the airframe emissions are upper bound estimates, it appears that these airframe emissions can be neglected relative to those from the engine. One notable exception might be refrigerants and gaseous fire extinguishers; if these species are highly photochemically active, the effects of direct deposition in the stratosphere need to be assessed. If there are no highly reactive catalytic effects of any of the other airframe emissions, it appears that their contribution to the net aircraft emissions may be neglected.

CONCLUDING REMARKS

Estimates have been provided for the emissions from a proposed HSCT in stratospheric flight. The emissions from the aircraft are expected to be dominated by the effluents from the engine and the emissions from the airframe are probably negligible. Current estimates for the NO_x emissions have been calculated by engine companies for the proposed engine cycles using correlations that have been developed over the past several decades of NO_x reduction programs. These estimates will have to be validated with future tests of components and full engines as development proceeds.

More complete measurements of particulate size distributions and number densities and of aerosol-active species will be required if heterogenous chemistry is to be accurately modeled, both in the wake of individual airplanes and globally. New measurements of NO_y speciation will be necessary to completely catalog the 'odd-nitrogen' emissions and to resolve uncertainties in measuring high temperature, high velocity exhaust gases with a sampling probe.

ACKNOWLEDGMENTS

The author would like to thank the contributors (Refs. 35-37, 39-41) for their materials and discussions concerning their inputs and R.W. Niedzwiecki and J.D. Holdeman of NASA Lewis Research Center for references and useful discussions. Many useful comments and suggestions were received from the several reviewers of an earlier draft of this chapter.

REFERENCES

1. Johnston, H. (1971) "Reduction of Stratospheric Ozone by Nitrogen Oxide Catalysts from Supersonic Transport Exhaust", *Science* 173, 517-522.
2. Barrington, A. E., ed. (1972) *Climatic Impact Assessment Program, Proceedings of the Survey Conference*, February 15-16, 1972, DOT-TSC-OST-72-13.
3. Broderick, A. J., ed. (1973) *Proceedings of the Second Conference on the Climatic Impact Assessment Program*, DOT-TSC-OST-73-4.
4. Broderick, A. J., and Hard, T. M., eds. (1974) *Proceedings of the Third conference on the Climatic Impact Assessment Program*, DOT-TSC-OST-74-15.
5. Hard, T. M., and Broderick, A. J., eds. (1976) *Proceedings of the Fourth Conference on the Climatic Impact Assessment Program*, DOT-TSC-OST-75-38.
6. CIAP Monograph 1, (1975) "The Natural Stratosphere of 1974", DOT-TST-75-51.
7. CIAP Monograph 2, (1975) "Propulsion Effluents in the Stratosphere", DOT-TST-75-52.
8. CIAP Monograph 3, (1975) "The Stratosphere Perturbed by Propulsion Effluents", DOT-TST-75-53.
9. CIAP Monograph 4, (1975) "The Natural and Radiatively Perturbed Troposphere", DOT-TST-75-54.
10. CIAP Monograph 5, (1975) "The Impacts of Climatic Change on the Biosphere", DOT-TST-75-55.
11. CIAP Monograph 6, (1975) "Economic and Social Measures of Biologic and Climatic Change", DOT-TST-75-56.

12. Boeing Commercial Airplane Co. (1989) 'High-speed civil transport study' NASA CR-4234.
13. Boeing Commercial Airplane Co. (1989) 'High-speed civil transport study - Summary' NASA CR-4234.
14. Douglas Aircraft Co. (1989) 'Study of high-speed civil transports' NASA CR-4235.
15. Holdeman, J.D. (1973) 'Dispersion of turbojet engine exhaust in flight' NASA TN D-7382.
16. Farlow, N. H., Watson, V. R., Loewenstein, M., Chan, K. L., Hoshizaki, H., Conti, R. J., and Meyer, J. W. (1974) "Measurements of Supersonic Jet Aircraft Wakes in the Stratosphere", Second International Conference on the Environmental Impact of Aerospace Operations in the High Atmosphere, American Meteorology Society, Boston, pp. 53-58.
17. Hoshizaki, H., et al. (1975) in CIAP Monograph 3, Chapter 2.
18. Broderick, A. J., et al. (1975) in CIAP Monograph 2, Chapter 4.
19. Aerospace Recommended Practice ARP 1256A (1980) 'Procedure for the continuous sampling and measurement of gaseous emissions from aircraft turbine engines' SAE.
20. Aerospace Recommended Practice ARP 1179A (1980) 'Aircraft gas turbine engine exhaust smoke measurement' SAE.
21. Spicer, C.W., Holdren, M.W., Lyon, F.F., and Riggin, R.M. (1985) 'Composition and Photochemical reactivity of Turbine Engine Exhaust' ESL-TR-84-61.
22. Spicer, C.W., Holdren, M.W., Miller, S.E., Smith, D.L., Smith R.N., and Hughes, D.P. (1988) 'Aircraft Emissions Characterization' ESL-TR-87-63.
23. Stumpf, S.A. and Blazowski, W.S. (1976) 'Detailed investigations of organic compound emissions from aircraft gas turbine engines' I.E.E.E. Annals No. 75CH1004-I-27-1.
24. Blazowski, W. S., and Sawyer, R. F. (1975) in CIAP Monograph 2, Chapter 3.
25. Low, H.C., Scott, C.J., and Veninger, A. (1990) 'Correlated Fuel Property Effects on an F402-RR-406A (Pegasus) Engine Combustor' ASME Paper 90-GT-276.
26. Federal Register (July 17, 1973) 'Emission standards and test procedures for aircraft' Vol. 38, No. 136, 19088-19102; (July 22, 1974) 'Supersonic aircraft pollution' Vol. 39, No. 141, 26653-26655; (March 24, 1978) 'Control of air pollution from aircraft and aircraft engines' Vol. 43, No. 58, 12614-12634; (December 30, 1982) 'Control of air pollution from aircraft and aircraft engines; Emission standards and test procedures' Vol. 47, No. 251, 58462-58474.
27. McGregor, W. K., Seiber, B. L., and Few, J. D. (1973) in the Second Conference on CIAP, 214-229.
28. Few, J. D., and Lowry, H. S., III (1981) Reevaluation of Nitric Oxide Concentration in Exhaust of Jet Engines and Combustors, AEDC-TR-80-65.
29. Jones, R. E. (1978) "Gas Turbine Engine Emissions-Problems, Progress and Future", *Prog. Energy Combust. Sci.* 4, 73-113.

30. Gleason, C.C. and Bahr, D.W. (1979) 'Experimental Clean Combustor Program (ECCP)' NASA CR-135384.
31. Roffe, G., and Venkataramani, K.S. (1978) "Emission Measurements for a Lean Premixed Propane/Air System at Pressures up to 30 Atmospheres" NASA CR159421.
32. Tacina, R.R. (1990) 'Low NO_x potential of gas turbine engines' AIAA paper 90-0550.
33. Holdeman, J.D. (1976) 'Exhaust emission calibration of two J-58 afterburning turbojet engines at simulated high-altitude, supersonic flight conditions' NASA TN D-8173.
34. Holdeman, J. D. (1976) "Measurements of Exhaust Emissions from Two J-58 Engines at Simulated Supersonic Cruise Flight conditions", ASME paper 76-GT-8.
35. Hasel, K. L.; Pratt & Whitney; East Hartford, CT; personal communication.
36. Matulaitis, J. A.; GE Aircraft Engines; Cincinnati, OH; personal communication.
37. Albers, M., and Hourmouziadis, J.; MTU; Munich, FRG; personal communication.
38. Grobman, J., and Ingebo, R. D. (1975) in CIAP Monograph 2, Chapter 5.
39. Gerstle, J. H., and Stander, C.; Boeing; Seattle, WA; personal communication.
40. Daggett, D.; Rolls-Royce, Inc.; Atlanta, GA; personal communication.
41. Hamilton, G.L.; Douglas Aircraft Co.; Long Beach, CA; personal communication.
42. Aerospace Standard AS 8010A (1986) 'Aviator's breathing oxygen purity standard' SAE.
43. Aerospace Standard AS 1304 (1973) 'Continuous flow chemical oxygen generators' SAE.

Chapter 2

Plume and Vortex Regime Modeling of Mixing and Chemistry*

SUMMARY

The environmental perturbations caused by the exhaust of a High Speed Civil Transport (HSCT) depend on the deposition altitude and the amount and composition of the emissions. The chemical evolution and the mixing and vortical motion of the exhaust need to be analyzed to track the exhaust and its speciation as the emissions are mixed to atmospheric scales. Elements of an analytic model of the wake dynamical processes are being developed to account for the roll-up of the trailing vorticity, its breakup due to the Crow instability, and the subsequent evolution and motion of the reconnected vorticity. The concentrated vorticity is observed to wrap up the buoyant exhaust and suppress its continued mixing and dilution. The chemical kinetics of the important pollutant species will be followed throughout the plume and wake. Initial plume mixing and chemistry are calculated using an existing plume model (SPF – Standard Plume Flowfield) with additional H/C/O, OH/SO₂, and NO_y chemistry and equilibrium H₂O condensation included. The species tracked include those that could be heterogeneously reactive on the surfaces of the condensed solid water (ice) particles when condensation occurs and those capable of reacting with exhaust soot particle surfaces to form active contrail and/or cloud condensation nuclei (ccn).

INTRODUCTION

The Anglo-French Concorde has shown that commercial supersonic air transportation is feasible. However, since it began commercial operations in the mid-1970s, the Concorde has served a low-volume, premium-fare market with its dozen-plus fleet. Technological advances in the intervening years have created the potential for a large fleet of more economical High Speed Civil Transports (HSCTs) that could serve a large commercial market,^{1,2} including trans-Atlantic and Pacific Rim routes in particular. With this possible development, attention has refocused³ on the environmental impact of a much larger fleet of airplanes operating in a flight regime close to that of the Concorde.

The potential effects of these aircraft on the chemical balance in the stratosphere—and on stratospheric ozone levels in particular—are a primary environmental concern. Atmospheric modelers^{4,5} have already begun to make estimates of the effects of the exhaust effluents of HSCTs on stratospheric chemistry. In doing so, a range of estimated emissions from the as-yet-undeveloped HSCT engines are deposited directly at representative altitudes and latitudes in their models. It is the purpose of the present study to provide initial estimates of chemical and physical changes that may occur between the exhaust leaving the engine and its deposition as a quiescent air mass in the stratosphere.

The exhaust from the large engines propelling a 250⁺ passenger supersonic airplane will be introduced into the ambient surroundings as a supersonic coflowing jet. Recent studies of supersonic mixing^{6,7} indicate that supersonic convective Mach numbers suppress mixing in free shear layers, an effect that will need to be accounted for in following the initial exhaust dilution. As this initial dilution is occurring, the vortex sheet shed by the lifting surfaces of the airplane is

* This chapter has been presented as AIAA paper 91-3158 at the Aircraft Design and Systems Meeting, 23-25 September 1991, Baltimore, MD. Also accepted for publication in *J. Aircraft*.

rolling up and being concentrated in a trailing vortex pair by mutual induction of the distributed vorticity. This vorticity field will begin to affect the diluting exhaust stream and will subject the exhaust to local conditions that are sufficiently different from ambient that significant changes in stratospheric exhaust deposition could result. The vorticity field behind a highly loaded supersonic aircraft configuration can differ dramatically from that of typical subsonic transports.

In the Climatic Impact Assessment Program of the early 1970s, a related study⁸ was performed using contrail data collected under that program and then-current understanding of chemistry, condensation physics, and vortex wake development. Just as supersonic flight technology has made great bounds since that time, revolutionary advances have recently been made in atmospheric chemistry. Great strides in the understanding of the stability and development of vortex wakes were being made concurrently with the CIAP program and continued since then and were not fully incorporated into that early study. Thus, while not starting completely anew, the present study represents a significant departure from the CIAP study and will provide a more comprehensive assessment of the chemistry and fluid physics occurring in the vortex wake.

The elements of an analytic model of these processes must include the dynamics of the vortex wake, from roll-up to breakup and dissipation; its interaction with the diluting hot exhaust; the gas-phase exhaust species chemistry; the heterogeneous chemistry occurring on condensed aerosols and soot particles; and the condensation physics governing the creation, or lack thereof, of the condensed aerosols needed for heterogeneous reactions. The stratospheric impact of the net result of all these elements will be felt through their displacement of the exhaust through vortical or buoyant transport⁹ or possible sedimentary removal of reactive species, as in polar stratospheric cloud (PSC) denitrification (and dehydration) of the polar stratosphere.^{10,11} Any major chemical repartitioning of the exhaust species that is not washed out by subsequent photochemical conversions may significantly affect the composition of the chemical inputs to the global models. An understanding of the structure, motions and persistence of the vortex wake will also be necessary for any attempt to measure the exhaust from an HSCT in flight and for evaluating the wake hazard created for following aircraft.

The analysis reported below represents the development of these several elements of a comprehensive exhaust plume/wake model for supersonic aircraft in cruise conditions. Gas-phase nozzle chemistry and plume chemistry are described in the next section and have been applied to understanding the engine exit plane conditions and the subsequent chemical evolution and condensation physics in the initial exhaust mixing region using extensions of a standard aircraft "plume" code. This chemistry will be applied in the vortex wake regime as well, as a refined model of its dynamics is finalized. The analytical basis for the vortex wake model is presented in the following section. The integration of these elements and requirements for further development are discussed in the last summary section.

TABLE 1.
Reaction List for HSCT Internal Engine Flow Model

reaction	rate constant ($\text{cm}^3 \text{molecule}^{-1} \text{s}^{-1}$)		
	A	N	$E/R (\text{K})$
$2\text{H} + \text{M} = \text{H}_2 + \text{M}$	1.50×10^{-29}	-1.3	0.0
$2\text{O} + \text{M} = \text{O}_2 + \text{M}$	5.20×10^{-35}	0.0	-900.0
$\text{H} + \text{O} + \text{M} = \text{OH} + \text{M}$	1.30×10^{-29}	-1.0	0.0
$\text{OH} + \text{H} + \text{M} = \text{H}_2\text{O} + \text{M}$	6.10×10^{-26}	-2.0	0.0
$\text{CO} + \text{O} + \text{M} = \text{CO}_2 + \text{M}$	1.70×10^{-33}	0.0	1510.0
$2\text{OH} = \text{H}_2\text{O} + \text{O}$	3.50×10^{-16}	1.4	-200.0
$\text{OH} + \text{H}_2 = \text{H}_2\text{O} + \text{H}$	1.06×10^{-17}	2.0	1490.0
$\text{OH} + \text{H} = \text{H}_2 + \text{O}$	8.10×10^{-21}	2.8	1950.0
$\text{OH} + \text{O} = \text{H} + \text{O}_2$	7.50×10^{-10}	-0.5	30.0
$\text{OH} + \text{CO} = \text{CO}_2 + \text{H}$	2.80×10^{-17}	1.3	-330.0
$\text{H} + \text{O}_2 + \text{M} = \text{HO}_2 + \text{M}$	1.77×10^{-30}	-1.0	0.0
$\text{H} + \text{HO}_2 = 2\text{OH}$	2.80×10^{-10}	0.0	440.0
$\text{HO}_2 + \text{H} = \text{H}_2 + \text{O}_2$	1.00×10^{-10}	0.0	1070.0
$\text{HO}_2 + \text{H}_2 = \text{H}_2\text{O}_2 + \text{H}$	5.00×10^{-11}	0.0	13100.0
$2\text{OH} + \text{M} = \text{H}_2\text{O}_2 + \text{M}$	1.60×10^{-33}	-3.0	0.0
$2\text{HO}_2 = \text{H}_2\text{O}_2 + \text{O}_2$	3.00×10^{-12}	0.0	0.0
$\text{H}_2\text{O}_2 + \text{OH} = \text{H}_2\text{O} + \text{HO}_2$	2.90×10^{-12}	0.0	160.0
$\text{NO} + \text{O} = \text{O}_2 + \text{N}$	6.31×10^{-15}	1.0	20820.0
$\text{O} + \text{N}_2 = \text{NO} + \text{N}$	3.02×10^{-10}	0.0	38370.0
$\text{NO} + \text{H} = \text{OH} + \text{N}$	4.37×10^{-10}	0.0	25370.0
$\text{NO}_2 + \text{H} = \text{NO} + \text{OH}$	5.76×10^{-10}	0.0	740.0
$\text{NO}_2 + \text{O} = \text{NO} + \text{O}_2$	1.66×10^{-11}	0.0	300.0
$\text{N}_2\text{O} + \text{O} = 2\text{NO}$	1.15×10^{-10}	0.0	13400.0
$\text{N}_2\text{O} + \text{H} = \text{N}_2 + \text{OH}$	1.26×10^{-10}	0.0	760.0
$\text{NO}_2 + \text{M} = \text{NO} + \text{O} + \text{M}$	1.82×10^{-08}	0.0	33000.0
$2\text{NO}_2 = 2\text{NO} + \text{O}_2$	3.31×10^{-12}	0.0	13500.0
$\text{HO}_2 + \text{OH} = \text{H}_2\text{O} + \text{O}_2$	2.40×10^{-08}	-1.0	0.0
$\text{HO}_2 + \text{O} = \text{OH} + \text{O}_2$	2.90×10^{-11}	0.0	-200.0
$\text{HO}_2 + \text{M} = \text{H} + \text{O}_2 + \text{M}$	2.00×10^{-05}	-1.2	24363.0
$\text{CO} + \text{O}_2 = \text{CO}_2 + \text{O}$	4.20×10^{-12}	0.0	24000.0
$\text{CO} + \text{HO}_2 = \text{CO}_2 + \text{OH}$	2.50×10^{-10}	0.0	11900.0
$\text{H}_2\text{O}_2 + \text{H} = \text{H}_2\text{O} + \text{OH}$	4.00×10^{-11}	0.0	2000.0
$\text{H}_2\text{O}_2 + \text{O} = \text{OH} + \text{HO}_2$	1.60×10^{-17}	2.0	2000.0
$\text{CO}_2 + \text{O} = \text{CO} + \text{O}_2$	2.80×10^{-11}	0.0	26500.0
$\text{NO}_2 + \text{OH} + \text{M} = \text{HNO}_3 + \text{M}$	2.20×10^{-22}	-3.2	0.0

PLUME MIXING AND CHEMISTRY

Internal Engine Flow/Finite-Rate Kinetics Model

The internal flow for a hypothetical Mach 2.4 engine design was modeled under realistic engine operating conditions using the ODK PACKAGE code¹² for reacting flows. Emphasis was given to estimating nonequilibrium concentrations of OH and HNO₃ at the nozzle exit plane since emission levels for these species are not currently being measured by propulsion laboratories and they were expected to strongly influence subsequent heterogeneous and homogeneous exhaust plume chemical kinetics.

The finite-rate kinetics for the internal engine flow were simulated using the reaction set consisting of 35 reversible reactions given in Table 1. These reactions were selected from kinetic data bases for hydrocarbon and nitrogen combustion chemistry. The hydrocarbon combustion reaction rate parameters were taken from a recent compilation¹³ of kinetic rate data for methane combustion. Rate parameters for the reactions describing the nitrogen combustion chemistry were taken from the recent review by Miller and Bowman.¹⁴

TABLE 2.
Internal Engine Flow Properties*

	combustor equil.	turbine equil.	turbine ODK	mixing chamber equil.	ODK	exit plane equil.	ODK
p (atm)	13.609	11.3	11.3	1.18	1.20	0.042	0.042
T (K)	2050.0	1398.0	1383.0	1046.0	1049.0	430.0	434.0
time (s)	NA	0.0033	0.0033	0.006	0.006	0.0009	0.0009
Mach no.	NA	2.17	2.17	0.26	0.26	2.85	2.84
CO	1.20×10^{-4}	1.52×10^{-7}	2.44×10^{-5}	2.02×10^{-11}	1.07×10^{-5}	5.67×10^{-31}	1.09×10^{-5}
CO ₂	6.84×10^{-2}	5.94×10^{-2}	5.93×10^{-2}	3.22×10^{-2}	3.24×10^{-2}	3.22×10^{-2}	3.24×10^{-2}
H	3.26×10^{-6}	1.21×10^{-9}	1.54×10^{-6}	3.52×10^{-14}	1.49×10^{-9}	0.0	6.12×10^{-9}
HNO ₃	3.28×10^{-10}	2.09×10^{-11}	6.24×10^{-10}	3.06×10^{-11}	4.46×10^{-9}	4.78×10^{-12}	4.07×10^{-8}
HO ₂	1.61×10^{-6}	1.93×10^{-8}	6.97×10^{-7}	3.05×10^{-10}	1.04×10^{-7}	1.03×10^{-20}	9.77×10^{-8}
H ₂	2.84×10^{-5}	7.91×10^{-8}	7.87×10^{-6}	2.70×10^{-11}	1.07×10^{-6}	4.17×10^{-28}	1.03×10^{-6}
H ₂ O	7.61×10^{-2}	6.62×10^{-2}	6.61×10^{-2}	3.57×10^{-2}	3.59×10^{-2}	3.57×10^{-2}	3.59×10^{-2}
H ₂ O ₂	1.90×10^{-7}	2.61×10^{-9}	1.65×10^{-8}	7.23×10^{-11}	2.56×10^{-8}	3.66×10^{-19}	2.44×10^{-8}
NO	5.99×10^{-3}	5.54×10^{-4}	5.20×10^{-3}	4.85×10^{-5}	2.81×10^{-3}	1.66×10^{-11}	2.81×10^{-3}
NO ₂	2.17×10^{-5}	3.16×10^{-6}	7.29×10^{-6}	1.76×10^{-6}	8.72×10^{-6}	1.70×10^{-9}	8.73×10^{-6}
N ₂	7.47×10^{-1}	7.54×10^{-1}	7.52×10^{-1}	7.66×10^{-1}	7.68×10^{-1}	7.66×10^{-1}	7.68×10^{-1}
N ₂ O	1.08×10^{-6}	3.31×10^{-8}	7.89×10^{-7}	3.45×10^{-9}	4.30×10^{-7}	8.74×10^{-16}	4.30×10^{-7}
O	7.95×10^{-5}	2.76×10^{-7}	3.23×10^{-5}	2.17×10^{-10}	1.56×10^{-7}	1.22×10^{-27}	1.55×10^{-7}
OH	9.41×10^{-4}	1.93×10^{-5}	2.09×10^{-4}	1.39×10^{-7}	4.21×10^{-6}	8.13×10^{-19}	3.40×10^{-6}
O ₂	9.23×10^{-2}	1.11×10^{-1}	1.08×10^{-1}	1.56×10^{-1}	1.56×10^{-1}	1.57×10^{-1}	1.56×10^{-1}

* species concentrations are in mole fraction

To simulate the internal engine flow, equilibrium calculations were first performed to determine the chemical composition of the flow from the combustor as a function of temperature and pressure.

ODK calculations were then performed in three stages to characterize the chemical and physical properties of the flow through the turbine, mixing chamber and nozzle. For each stage, the pressure and temperature at the initial and end axial points were constrained to be consistent with representative GE engine parameters.¹⁵ In addition, when necessary, the mixture was diluted to account for the mixing in of bypass air. Nozzle exit plane species mole fractions obtained by this method are compared against equilibrium predictions in Table 2.

Although the one dimensional exit plume results shown in Table 2 can only approximate the chemistry and flow dynamics of anticipated HSCT engines, they do confirm that significantly non-equilibrium levels of CO, NO, NO₂, HNO₃ and OH can be anticipated at the engine nozzle exit plane. While the engine development community has long accepted the non-equilibrium nature of CO and NO_x emissions, there has been less appreciation of the high (> ppm) levels of OH emitted by gas turbine systems. The predictions presented here are consistent with the optical absorption measurements performed on the YJ93-GE-3 under stratospheric cruise conditions by McGregor *et al.*¹⁶ during the CIAP program. In that study, mole fractions of exit plane OH exceeded 2×10^{-5} and 4×10^{-5} for cruise power settings equivalent to Mach 2.6 operation at 66 kft and Mach 2.0 at 55 kft.

HSCT Plume Flow/Finite-Rate Chemical Kinetics Model

The standard plume flowfield code, SPF-2,¹⁷ was used to characterize the chemical and physical properties of the combustion exhaust plume associated with an advanced high altitude supersonic aircraft. Model simulations used GE parameters¹⁵ for a hypothetical Mach 2.4 engine to specify initial exhaust emission parameters and 1990 atmospheric models¹⁸ to specify the ambient atmospheric parameters. The SPF code was modified to include an initial estimate of the degree of H₂O condensation based on thermodynamic equilibrium. Initial examination of the plume chemistry focused on the evolution of NO_x, including an evaluation of the impact of ozone oxidation mechanisms and the percentage conversion to HNO₃, as well as SO_x oxidation cycles.

Initial Conditions The species concentrations and thermodynamic properties used as initial conditions in model simulations of the plume chemistry and mixing are given in Table 3. This includes ambient free stream conditions and the initial conditions for the exhaust at the nozzle exit plane. Exit plane species distributions are based either on reported emission indices (g equiv/kg fuel) or on ODK calculations for the internal engine flow. An exit plane OH mole fraction of 1×10^{-5} representing a rough mean between calculated ODK value shown in Table 2 and the measurements of McGregor *et al.*¹⁶ was adopted for these plume calculations. For NO_x, an emission index¹⁹ EI_(NO₂)NO_x of 5 was used²⁰ assuming 10% NO₂ and 90% NO on a molar basis. Ambient free-stream conditions are given for three representative cases. These correspond to the atmospheric conditions appropriate for January 1 and June 1 at a latitude of N47 and June 1 at N85. In all three cases, the altitude was \sim 18 km. Ambient conditions were obtained from AER's 1990 atmospheric chemistry data base.¹⁸

TABLE 3.
Initial Conditions for HSCT Plume Flowfield Model*

	exhaust	free stream		
	case 1	case 2	case 3	
latitude		N47	N47	N85
altitude(km)		18.4	17.85	18.3
date		June 15	January 1	January 1
p(atm)		0.0734	0.0712	0.0573
T (K)	5.61×10^2	2.19×10^2	2.17×10^2	2.05×10^2
v (ft/s)	4.30×10^3	2.34×10^3	2.32×10^3	2.26×10^3
CO	2.37×10^{-5}	1.99×10^{-8}	1.98×10^{-8}	1.69×10^{-8}
CO ₂	3.17×10^{-2}	3.50×10^{-4}	3.50×10^{-4}	3.50×10^{-4}
H	1.00×10^{-7}	1.43×10^{-20}	2.81×10^{-21}	0.0
H ₂	0.0	5.18×10^{-7}	5.19×10^{-7}	5.20×10^{-7}
H ₂ O	3.02×10^{-2}	4.20×10^{-6}	4.20×10^{-6}	4.86×10^{-6}
HO ₂	0.0	1.02×10^{-12}	3.30×10^{-13}	0.0
H ₂ O ₂	0.0	3.51×10^{-12}	2.11×10^{-12}	0.0
N ₂	0.779	0.790	0.790	0.790
NO	4.32×10^{-5}	2.43×10^{-10}	5.87×10^{-11}	0.0
NO ₂	4.80×10^{-6}	8.50×10^{-10}	4.29×10^{-10}	0.0
O	0.0	6.06×10^{-13}	3.11×10^{-13}	0.0
OH	1.00×10^{-5}	1.27×10^{-13}	2.76×10^{-14}	0.0
O ₂	0.159	0.210	0.210	0.210
O ₃	0.0	2.48×10^{-6}	2.46×10^{-6}	3.02×10^{-6}
HNO ₃	0.0	3.71×10^{-9}	3.32×10^{-9}	7.39×10^{-9}
NO ₃	0.0	1.23×10^{-12}	1.71×10^{-12}	0.0
N ₂ O ₅	0.0	3.57×10^{-10}	6.09×10^{-10}	0.0
SO ₂	6.91×10^{-6}	0.0	0.0	0.0

* species concentrations are in mole fraction

TABLE 4.
SPF Equilibrium H₂O Condensation Predictions

	case 1	case 2	case 3
latitude	N47	N47	N85
altitude(km)	18.4	17.85	18.3
date	June 15	January 1	January 1
T(K)	219.3	216.7	205.2
p(atm)	0.0734	0.0712	0.0573
SPF Equilibrium H ₂ O			
Condensation predictions	no	no	yes
Condensation algorithm			
predictions (Ref. 21)	never	uncertain	always

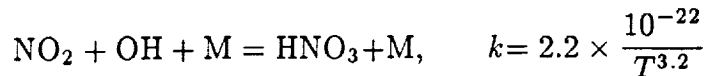
H₂O Condensation The SPF-2 code was modified to predict the degree of H₂O condensation during the plume expansion as part of an initial investigation into the potential role of heterogeneous kinetic processes in affecting plume chemistry. Condensation was treated using the standard vapor pressure test for thermodynamic equilibrium. It was assumed that the any condensed H₂O particulates that formed would not significantly modify the flow mixing dynamics. A summary of the SPF equilibrium H₂O condensation predictions are given in Table 4 for the three case runs described by the free stream ambient conditions in Table 3. For comparison, condensation predictions based on Appleman's equilibrium, fully-mixed condensation algorithm²¹ are also listed in Table 4. In general, the agreement between these two approaches is good.

Plume Chemistry

The reaction set used to simulate the exhaust plume finite-rate chemical kinetics is listed in Table 5. Rate parameters for these reactions are based on a 1990 NASA evaluation²² of the chemical kinetics data for use in stratospheric modeling. The reaction set includes reactions to describe NO_x/O₃ reactions and SO₂ oxidation kinetics.

Representative model results are presented in Table 6 which lists the plume mole fractions for nitrogen and sulfur oxides, nitric acid, hydroxyl radical and ozone on the plume axis at axial points 500, 1000 and 2000 feet downstream of the nozzle exit plane. The speciation given Table 6 is based on model runs using ambient atmospheric conditions appropriate for June 15 at a N47 latitude (case 1 in Table 3). However, similar results were obtained for model runs with ambient conditions corresponding to January 1 at the same latitude (case 2 in Table 3). The only difference was a 1.7 increase in the mole fraction of N₂O₅.

Mole fraction ratios for NO₂/NO, HNO₃/NO_x and SO₃/SO₂ are also given in Table 6 where, in this case, NO_x corresponds to the sum of NO and NO₂ mole fractions. Based on this data, the SPF model calculations indicate that approximately 11% of the initial SO₂ is oxidized to SO₃. NO is oxidized to NO₂ by entrained ambient O₃. NO₂, in turn, is oxidized primarily by exhaust OH. The NO₂/NO ratio is maintained at 0.10-0.11 while approximately 5% of the NO_x is converted to HNO₃. Previous studies by Hoshizaki *et al.*⁸ concluded that about 10-20% of the NO_x emitted is transformed to HNO₃ in the jet plume region, i.e. 1-10 seconds after the exhaust is emitted. Although this represents a significantly larger percentage conversion than predicted in SPF-2 simulations, the discrepancy can be explained in terms of differences in the rate parameters used. The dominant mechanism for formation of HNO₃ is



In the early work of Hoshizaki *et al.*⁸ this reaction was treated as a simple bimolecular reaction with a rate constant ($k = 4.8 \times 10^{-12}$) orders of magnitude larger than that adopted in the 1990 NASA evaluation²² of the best fit to experimental data over the temperature range of interest.

TABLE 5.
Reactions List for Plume Chemistry/Mixing Model

reaction	rate constant ($\text{cm}^3 \text{molecule}^{-1} \text{s}^{-1}$) $k = A e^{(-E/RT)} / T^N$	A	N	E/R (K)
$\text{H} + \text{O}_2 + \text{M} = \text{HO}_2 + \text{M}$	5.2×10^{-28}	1.6	0.0	
$\text{OH} + \text{O} = \text{H} + \text{O}_2$	2.2×10^{-11}	0.0	240.0	
$\text{OH} + \text{H}_2 = \text{H}_2\text{O} + \text{H}$	5.5×10^{-12}	0.0	-4000.0	
$\text{OH} + \text{OH} = \text{H}_2\text{O} + \text{O}$	4.2×10^{-12}	0.0	-480.0	
$\text{OH} + \text{OH} + \text{M} = \text{H}_2\text{O}_2 + \text{M}$	6.6×10^{-29}	0.8	0.0	
$\text{OH} + \text{HO}_2 = \text{H}_2\text{O} + \text{O}_2$	4.8×10^{-11}	0.0	500.0	
$\text{OH} + \text{H}_2\text{O}_2 = \text{H}_2\text{O} + \text{HO}_2$	2.9×10^{-12}	0.0	-320.0	
$\text{HO}_2 + \text{O} = \text{OH} + \text{O}_2$	3.0×10^{-11}	0.0	400.0	
$\text{HO}_2 + \text{H} = \text{OH} + \text{OH}$	4.2×10^{-10}	0.0	1900.0	
$\text{HO}_2 + \text{H} = \text{H}_2 + \text{O}_2$	4.2×10^{-11}	0.0	-700.0	
$\text{HO}_2 + \text{HO}_2 = \text{H}_2\text{O}_2 + \text{O}_2$	2.3×10^{-13}	0.0	1200.0	
$\text{H}_2\text{O}_2 + \text{O} = \text{OH} + \text{HO}_2$	1.4×10^{-12}	0.0	-4000.0	
$\text{N} + \text{O}_2 = \text{NO} + \text{O}$	1.5×10^{-11}	0.0	-7200.0	
$\text{N} + \text{NO} = \text{N}_2 + \text{O}$	3.4×10^{-11}	0.0	0.0	
$\text{NO} + \text{O} + \text{M} = \text{NO}_2 + \text{M}$	4.7×10^{-28}	1.5	0.0	
$\text{NO} + \text{HO}_2 = \text{NO}_2 + \text{OH}$	3.7×10^{-12}	0.0	480.0	
$\text{NO} + \text{NO}_3 = \text{NO}_2 + \text{NO}_2$	1.7×10^{-11}	0.0	300.0	
$\text{NO}_2 + \text{O} = \text{NO} + \text{O}_2$	6.5×10^{-12}	0.0	240.0	
$\text{NO}_2 + \text{O} + \text{M} = \text{NO}_3 + \text{M}$	8.1×10^{-27}	2.0	0.0	
$\text{NO}_2 + \text{OH} + \text{M} = \text{HNO}_3 + \text{M}$	2.2×10^{-22}	3.2	0.0	
$\text{NO}_2 + \text{NO}_3 + \text{M} = \text{N}_2\text{O}_5 + \text{M}$	9.9×10^{-20}	4.3	0.0	
$\text{NO}_3 + \text{O} = \text{NO}_2 + \text{O}_2$	1.0×10^{-11}	0.0	0.0	
$\text{O} + \text{O}_2 + \text{M} = \text{O}_3 + \text{M}$	3.0×10^{-28}	2.3	0.0	
$\text{O} + \text{O}_3 = \text{O}_2 + \text{O}_2$	8.0×10^{-12}	0.0	-4120.0	
$\text{H} + \text{O}_3 = \text{OH} + \text{O}_2$	1.4×10^{-10}	0.0	-940.0	
$\text{OH} + \text{O}_3 = \text{HO}_2 + \text{O}_2$	1.6×10^{-12}	0.0	-1880.0	
$\text{NO} + \text{O}_3 = \text{NO}_2 + \text{O}_2$	2.0×10^{-12}	0.0	-2800.0	
$\text{NO}_2 + \text{O}_3 = \text{NO}_3 + \text{O}_2$	1.2×10^{-13}	0.0	-4900.0	
$\text{OH} + \text{HNO}_3 = \text{H}_2\text{O} + \text{NO}_3$	7.2×10^{-15}	0.0	1570.0	
$\text{SO} + \text{O}_2 = \text{SO}_2 + \text{O}$	1.4×10^{-13}	0.0	-4550.0	
$\text{SO} + \text{O}_3 = \text{SO}_2 + \text{O}_2$	4.5×10^{-12}	0.0	-2340.0	
$\text{SO}_2 + \text{OH} + \text{M} = \text{HSO}_3 + \text{M}$	7.5×10^{-23}	3.3	0.0	
$\text{HSO}_3 + \text{O}_2 = \text{HO}_2 + \text{SO}_3$	4.0×10^{-13}	0.0	0.0	
$\text{SO} + \text{NO}_2 = \text{SO}_2 + \text{NO}$	1.4×10^{-11}	0.0	0.0	
$\text{SO} + \text{OH} = \text{SO}_2 + \text{H}$	8.6×10^{-11}	0.0	0.0	
$\text{SO}_2 + \text{O} + \text{M} = \text{SO}_3 + \text{M}$	4.0×10^{-32}	0.0	-2000.0	

TABLE 6.
 Plume Centerline NO_x, SO_x and Oxidizer Speciation
 (Mach 2.4; N47; 18.4 km; June 15)

species	mole fractions			
	exit plane	500 ft	1000 ft	2000 ft
OH	1.0×10^{-5}	1.4×10^{-7}	1.4×10^{-8}	1.9×10^{-9}
O ₃	0.0	2.1×10^{-6}	2.4×10^{-6}	2.4×10^{-6}
NO	4.3×10^{-5}	6.2×10^{-6}	2.0×10^{-6}	9.4×10^{-7}
NO ₂	4.8×10^{-6}	6.2×10^{-7}	2.0×10^{-7}	1.0×10^{-7}
NO ₃	0.0	2.1×10^{-11}	4.5×10^{-12}	8.1×10^{-13}
N ₂ O ₅	0.0	2.1×10^{-10}	3.2×10^{-10}	3.4×10^{-10}
HNO ₃	0.0	2.4×10^{-7}	1.1×10^{-7}	5.9×10^{-8}
SO ₂	6.9×10^{-6}	9.5×10^{-7}	3.0×10^{-7}	1.4×10^{-7}
SO ₃	0.0	6.8×10^{-8}	3.2×10^{-8}	1.6×10^{-8}
NO ₂ /NO	0.11	0.10	0.10	0.11
HNO ₃ /NO _x	—	0.035	0.05	0.056
SO ₃ /SO ₂	—	0.07	0.11	0.11

The SO₃ and N₂O₅ created in the exhaust plume will react immediately on contact with contrail droplets or particles to form condensed phase H₂SO₄ and HNO₃, respectively. Exhaust gaseous HNO₃ will also condense onto contrail particles. Each of these species, gaseous SO₃, N₂O₅ and HNO₃ can also be expected to interact with exhaust soot, as can exhaust NO₂²³ and entrained atmospheric O₃,²⁴ to create oxidized soot surfaces capable of nucleating either exhaust contrails or atmospheric acid/water aerosols after plume mix-out. This soot surface conditioning may be an important plume chemical effect since only 1% of the soot particles formed by burning jet fuel can immediately condense water vapor at typical plume supersaturation ratios without such conditioning.²⁵ We plan to incorporate these heterogeneous processes in future plume chemistry models.

VORTEX WAKE DYNAMICS

The scales and regimes involved in the dispersion of pollutants from the exhaust of stratospheric aircraft have been discussed by several authors mainly in connection with the CIAP studies in the 70's.^{26,27} The early part of the process (the first hour) was described in some detail by Hoshizaki *et al.*,²⁸ who called this period "the wake regime". The first few tens of seconds of this period are characterized by the dominant role of the aerodynamic flowfield of the aircraft (first through the momentum of the jet itself, and later through the effect of the aircraft sinking vortex pair). Wake dispersion, after an ill-defined transition, is dominated by environmental effects, such as wind shear.

Based on the analysis of horizontal and vertical photographs of B-52 contrails, Ref. 28 concluded that in a first phase, called the "jet regime", the engine plumes grow by ordinary turbulent mixing to fill the recirculating vortex pair cell (of dimensions roughly 1.2×1.5 times the wing span). The

attraction to the wing tip vortex cores was noted, but dismissed as a minor effect. After this time (~ 10 s), the effluent remains horizontally confined by the cell, but detrainment from the top as the cell descends leads to vertical growth. This "vortex" phase ends at about 100 s with the breakup of the vortex pair, following which the wake remnants gradually lose their organized motion and ambient effects dominate. The effect of the aircraft was noticed, however, for as much as one hour, since different aircraft lead to different dispersion rates on that time scale. This conceptual model (along with the models of Holdeman²⁹ and Nielsen³⁰ which ignored wake interactions) were later also applied to the analysis of supersonic YF-12 flight data. The interpretation of the growth of this wake is complicated by the visualization method used, as will be discussed below.

As will be discussed more fully in later sections, the depth of the pressure and temperature minima induced by the rolled-up wing-tip vortices scale as the square of the Mach number, and inversely with the square of the wing aspect ratio. Thus, what was found to be a minor effect when examining transonic aircraft may become a very important effect for a low aspect ratio supersonic aircraft. The horizontal densitometer scans of B-52 contrails (Hoshizaki *et al.*, Ref. 28) already show two peaks at the expected vortex core locations, and many other observations (see for instance photographs in Ref. 32) indicate the persistence of these two separate, well-defined and non-growing columns of condensation material up to the time of vortex breakdown.

The extent of plume gas trapping in the low pressure troughs caused by the vortical motion, and the degree to which exhaust gas is able to escape and be detrained from the sinking recirculating vortex pair cell determine the effectiveness of the vortex confinement and mixing suppression. These factors are strongly dependent on the relative spanwise location of the engines and the vortex cores, and also on the "attraction" of these cores, as measured by their pressure trough depth. The trapped and the detrained portions of the exhaust gas follow very different dilution and cooling histories. While the classical Appleman²¹ treatment (isobaric mixing of effluent and ambient air) should be applicable to the detrained portion, the portion captured by the vortex cores may undergo significantly lower temperatures during mixing, due to adiabatic expansion into the low pressure of the core. Since, to begin with, stratospheric conditions of interest are typically within $\pm 10^\circ\text{C}$ of the Appleman contrail threshold, these deviations may well initiate ice formation in the cores under conditions for which contrails would not be predicted ordinarily. In addition, the trapped gas dilutes at a much reduced rate, and this may provide ice growth times and/or chemical reaction times much longer than otherwise expected.

Given the stronger confining effect of the vortex cores in a supersonic, as compared to a transonic, aircraft, it is not even clear whether substantial detrainment from the descending vortex pair cell is to be expected in the supersonic case. If vertical detrainment were either absent or strongly reduced, the morphology of the effluent distribution at the end of the vortex wake would be quite different from what has been accepted since the studies in the 1970's. In the YF-12 data of Ref. 31, there was little vertical growth in the wake regime, amounting to as little as 1/4 of that predicted by the "detrainment" model of Ref. 28. Unfortunately, interpretation of these supersonic cruise data is complicated by the fact that the measurement was based on in-flight fuel dumps from the aircraft centerline. Only those portions of the dump which mixed with the warm buoyant plume would be subject to vortex capture, leaving the rest free to detrain.

An additional difference between conventional and supersonic aircraft wakes must be mentioned here. For most conventional aircraft, the vortex pair becomes unstable and breaks up into irregular

vortex rings at about the same time as its vertical motion is arrested by the stable atmospheric stratification. Organized vertical motion would in any case be ended by the latter effect at this point, and the coincidence has led to an identification of "vortex pair breakup" with "vorticity dissipation". In the supersonic case, however, the vortex pair has more vertical momentum, and its vertical motion will continue (in the form of vortex rings) well after the straight vortex system has broken up. This will probably lead to pollutant deposition at lower altitudes (by a few hundred meters) than expected, and also to longer than expected confinement times. The effect may also be significant in terms of wake hazards to other aircraft.

The following section, plus Appendices A and B, provide a more detailed discussion of these effects, based on a series of simplified analytical models which are intended to approximately quantify their relative importance and scales.

Analysis

Aircraft and Vortex Parameters Table 7 summarizes the parameters assumed for our vortex wake analysis. The airplane is a Mach number 2.4 design beginning its cruise at 17.4 km altitude. For estimates of wake properties, an elliptic loading distribution has been adopted, and the vortex roll-up distance was estimated based on Ref. 33.

TABLE 7.
Assumed Aircraft Data for Wake Dynamics

Wing area:	$A_W = 660 \text{ m}^2$	Span:	$b = 39 \text{ m}$
Weight (cruise):	$W = 2.76 \times 10^6 \text{ N}$		
Flight altitude:	$Z = 17.4 \text{ km}$	Aspect Ratio:	$\frac{b^2}{A_W} = 2.30$
Mach No.:	$M = 2.4$	Speed:	$v = 708 \text{ m/s}$
Atmosphere: $\rho = 0.135 \text{ kg/m}^3$, $T = 217 \text{ K}$, $p = 83.8 \text{ mb}$			
Lift coefficient: $C_L = 0.124$			
Exhaust temperature: $T_e = 445 \text{ K}$			
Fuel/air ratio: 0.0155			
Airflow: $m_a = 97 \text{ Kg/s/engine}$			
Exhaust speed (relative): 1430 m/s			
Wake time scale: $\tau = 2 \frac{A_R b}{C_L v} = \frac{\rho v b^3}{W} = 2.04 \text{ s}$			
Vorticity roll-up time: $t_{r.u.} \cong 1.5\tau = 3.07 \text{ s}$			
Vorticity roll-up distance: $x_{r.u.} = vt_{r.u.} = 2170 \text{ m (56 b)}$			
Rolled-up vortex spacing: $2\bar{y} = \frac{\pi}{4}b = 30.6 \text{ m}$			
Centerline vortex circulation: $\Gamma_0 = \frac{4}{\pi} \frac{W}{\rho v b} = 943 \text{ m}^2/\text{s}$			
Self-induced descent velocity: $w_0 = \frac{\Gamma_0}{2\pi(2\bar{y})} = 4.90 \text{ m/s}$			
Vortex break-up time: $t_{v.b.} \cong 15\tau = 30.7 \text{ s}$			
Vortex break-up distance: $x_{v.b.} = vt_{v.b.} = 21,700 \text{ m (556 b)}$			

The structure of the vortices after roll-up has been calculated based on the Betz-Donaldson model,^{33,34} according to which the circulation originally bound to the wing outboard of a spanwise location y_1 will end up rolled into the inner part of the trailing vortex core, within a radius r from its

center—which equals the distance from y_1 to the centroid of the circulation distribution outboard of y_1 . For the assumed elliptic loading, this model predicts a tangential velocity distribution near each core given by

$$\frac{v_\theta}{v} = 0.25 \frac{C_L}{AR} \sqrt{\frac{b}{r}} , \quad (1)$$

where v is the flight speed, C_L the lift coefficient, AR the wing aspect ratio, b the wing span and r the distance to the vortex core. This has been confirmed in tests,³³ and it appears to hold to radii much smaller than the classical core size estimate of Prandtl,³⁴ with the result that v reaches higher values near the core than expected on the basis of a model with all the vorticity concentrated in the Prandtl core. The validity of the Betz-Donaldson model has been debated,³⁵ and no rigorous basis for it seems to exist. We use it here simply as a convenient semi-empirical device.

Using Eq. (1), several quantities of interest can be calculated. The centripetal acceleration v_θ^2/r is, using the parameters in Table 7,

$$g_{\text{centripetal}} \cong \frac{3500}{r^2} \quad (\text{in MKS units}) . \quad (2)$$

With reference to Fig. 1, this gives 26 m/s^2 at the inboard plume location, and 73 m/s^2 at the outboard plume location. This shows that centripetal buoyancy effects will be strong and will compete with (perhaps dominate) those of upwards buoyancy and turbulent detrainment of effluents from the cell's edge. Notice (Eq. (1)) that the peculiar features of the HSCT (small AR , high v) greatly emphasize this effect. For a transonic airplane of the same wing area but with a lift coefficient of 0.5 and an AR of 10, $g_{\text{centripetal}}$ would be less by a factor of 17.2 at the same value of b/r . This makes plume/wake interaction a secondary issue for such aircraft, and may account for its dismissal by Hoshizaki et al.²⁸ and, more generally, for the lack of attention it has elicited so far.

The pressure gradient set up by the vortex follows easily from the hydrostatic radial force balance $\partial p / \partial r = -\rho v_\theta^2 / r$. From Eq. (1) and ignoring the relatively small effects of compressibility the local depression, $\Delta p = p_\infty - p$, is seen to vary as $1/r$. Assuming adiabatic expansion, the corresponding temperature depression is found to be

$$\frac{\Delta T}{T_a} = -\frac{6(\gamma - 1)}{\pi^4} \frac{M^2 C_L^2 b}{AR^2 r} . \quad (3)$$

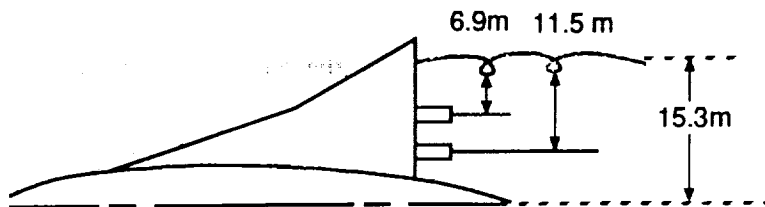


FIG. 1. Engine location with respect to rolled-up vortex core. The core is at $(\pi/4)(b/2)$ from centerline.

For the parameters of Table 7, we find $\Delta T(K) \cong -3.5/r(m)$. Once again, for typical transonic aircraft the corresponding ΔT is less by a factor of 83, making it almost unobservable.

The vortex system is known to break up due to growth of the Crow instability (vortex bursting is unlikely at the moderate C_L of cruise). The estimate for breakup time given in Table 7 ($t_B \cong 15\tau$) is consistent with data of Ref. 36 for a quiescent atmosphere, and is 50% longer than the estimate given by Hoshizaki *et al.*²⁸ for tropospheric conditions.

Turbulent Plume Growth with Buoyancy Effects The initial spread of the engine plumes must be controlled by turbulence generated by the plume/ambient velocity shear. However, centripetal buoyancy effects must be felt strongly, as noted, and will eventually dominate the plume dynamics. The overall dynamics is fairly complex, and we will attack it initially by considering simpler model problems. The first question is the estimation of the time after which buoyancy dominates over jet growth. To this end, we temporarily ignore the shearing of the plume by the vortex flowfield, and consider a buoyant round engine jet in the co-flowing airstream. The analysis is relegated to Appendix A, and is based on the use of a turbulent diffusivity model which combines those of Prandtl³⁷ for a coflowing jet and of Morton, Taylor and Turner³⁸ for a rising linear plume. The resulting jet diameter is found to evolve with distance x as,

$$\frac{D}{D_0} = [1 + \theta G(\xi)]^{1/3}, \quad (4a)$$

where

$$\xi = x/\ell, \quad \ell = \frac{1}{19} \frac{\eta_{ov}}{1 - \eta_{ov}} \frac{c_p T_a}{g_{eff}}, \quad (4b)$$

$$\theta = 0.061 \frac{F \ell}{\rho v_a^2 D_0^3} \quad (4c)$$

and

$$G(\xi) = \xi \sqrt{1 + \xi^2} + \ln(\xi + \sqrt{1 + \xi^2}). \quad (4d)$$

Here, η_{ov} is the overall engine efficiency (fuel heat value to thrust), F is the engine thrust and D_0 is the engine nozzle diameter. The acceleration, g_{eff} , could be either the actual gravitational acceleration, or the centripetal acceleration calculated above.

By examination of Eqs. (4a)–(4d) we can see that when $\xi \ll 1$, $D \cong x^{1/3}$ (jet-dominated regime), and when $\xi \gg 1$, $D \cong x^{2/3}$ (buoyant plume regime). The two are nearly equivalent at $\xi = 2$. For the parameters of Table 7, and using the centripetal g for either engine, we find that $\xi = 2$ is reached when $D/D_0 = 2.17$ (outboard engine) or $D/D_0 = 2.89$ (inboard engine). Thus, by the time centripetal buoyancy becomes the dominant plume growth mechanism, the dilution ratio (proportional to $(D/D_0)^2$) is about 4.7 to 8.3, depending on which engine is considered. For comparison, using "natural" gravity ($g = 9.8 \text{ m/s}^2$), the crossover occurs when $D/D_0 = 4.60$ (dilution ratio = 21), by which time the plumes would fill a substantial fraction of the vortex cell.

The analysis above has not accounted for the effects of compressibility on turbulent jet mixing. Ref. 6 shows substantial mixing suppression when the "convective Mach number", M^* exceeds about 0.5. M^* is measured with respect to an intermediate frame in which both pressure and total pressure are equal for both streams. In the case of equal specific heat ratios, this reduces to

$$M^* = \frac{v_2 - v_1}{a_2 + a_1}. \quad (5)$$

where v and a are the respective flow and sonic velocities of the two streams. In our case (Table 7) $M^* \cong 1.01$, and the initial mixing rate should be reduced by a factor f_c between 0.2 and 0.4.⁶ The factor f_c will then approach unity as mixing proceeds and the relative Mach number decreases. The effect on the above analysis would be that the average f_c would multiply both θ and ℓ .

A Model for Plume-Vortex Interactions The fluid mechanics of the turbulent buoyant jet in the flow field of a concentrated vortex is too complex to be adequately analyzed here, but we will at least account for the salient features in an attempt to estimate the capture time of the engine exhaust into the vortex cores. The following assumptions are made:

- The plume is convected and sheared by the (un-modified) Betz-Donaldson vortex flow. The shearing spreads the plume around a circle centered at the vortex core, at a rate proportional to the difference $v_\theta(r - D/2) - v_\theta(r + D/2)$ where r is the distance to the core and D is the transverse plume size (See Fig. 2).
- The plume cross-section grows by entrainment of ambient air, in proportion to its inward radial velocity times its projected area (Morton-Taylor-Turner model³⁸). No account is taken of axial flow, except that the model is used to estimate a plume diameter as it begins to be affected by the vortex.
- The radial motion is obtained from a momentum balance, using the centripetal buoyancy of Eq. 2.

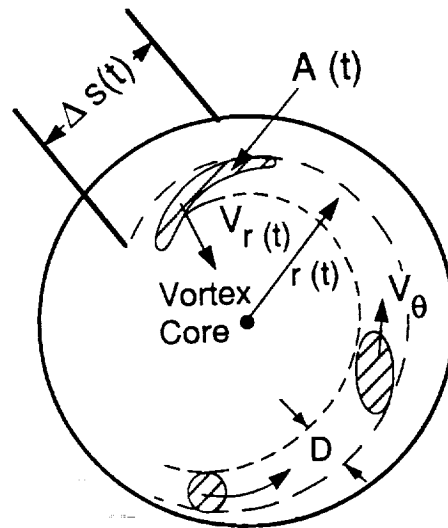


FIG. 2. Geometry of plume trapping in a plane transverse to the flight path.

Letting A be the plume cross-section at a given time, and $\Delta\rho$ the mean density defect in the plume, mass conservation imposes

$$\frac{d}{dt}(A\Delta\rho) = 0 \quad . \quad (6)$$

The entrainment rate assumption gives

$$\frac{dA}{dt} = \alpha \Delta s v_r \quad , \quad (7)$$

where Δs is the tangential plume spread (Fig. 2), v_r is its radial velocity (inwards), and $\alpha \cong 0.94$ is chosen to correspond for the circular cylinder case to the value used in Ref. 28.

Equating the buoyancy force to the rate of momentum increase due to mass accretion gives

$$\alpha \rho_a v_r^2 \Delta s = \frac{v_\theta^2}{r} A \Delta \rho \quad . \quad (8)$$

Finally, the shearing assumption is expressed as

$$\frac{d}{dt} \left(\frac{\Delta s}{r} \right) = D \frac{\partial}{\partial r} \left(\frac{v_\theta}{r} \right) \quad . \quad (9)$$

where D is assumed constant.

Combining Eqs. (6)–(9) with the expression Eq. (1) for v_θ leads to a set of differential equations, for which closed-form solutions can be obtained:

$$\begin{aligned} \frac{v_r t}{b} = 0.61 \alpha \frac{AR}{C_L} \frac{(r_0/b)^{5/2}}{(D_0/b)(\Delta \rho/\rho)_0} & \left[1 + 2.95 \sqrt{\frac{D_0/r_0}{\alpha(\Delta \rho/\rho)_0}} \right. \\ & \left. \left[1 - \left(\frac{r}{r_0} \right)^{5/2} \right] - \left(\frac{r}{r_0} \right)^{5/2} \left(1 + \frac{5}{2} \ln \frac{r_0}{r} \right) \right] \end{aligned} \quad (10)$$

and

$$\begin{aligned} \frac{A}{A_0} = 1 + \frac{2}{\pi} \left(\frac{r_0}{D_0} \right)^2 & \left[\left(\frac{D_0}{r_0} + \frac{\sqrt{D_0/r_0} + 1/2\beta}{\beta} \right) \right. \\ & - \left(\frac{r}{r_0} \right)^2 \left\{ \left(\sqrt{\frac{D_0}{r_0}} + \frac{\ln(r_0/r)}{\beta} \right)^2 + \right. \\ & \left. \left. \frac{1}{\beta} \left(\sqrt{\frac{D_0}{r_0}} + \frac{\ln(r_0/r) + 1/2}{\beta} \right) \right\} \right] \end{aligned} \quad (11)$$

where

$$\beta = \frac{4}{3} \sqrt{\frac{\pi}{4\alpha} \left(\frac{\Delta \rho}{\rho} \right)_0} \quad , \quad (12)$$

and also

$$\Delta \theta = \left(\sqrt{\frac{D_0}{r_0}} + \frac{\ln(r_0/r)}{\beta} \right)^2 \quad , \quad (13)$$

$$\frac{\Delta \rho/\rho}{(\Delta \rho/\rho)_0} = \frac{A_0}{A} \quad . \quad (14)$$

For application, the initial distance r_0 is 6.9 m for the outboard and 11.5 m for the inboard engine. The initial diameter D_0 and dilution (or density depression $(\Delta \rho/\rho)_0$) can only be approximately

selected to account for the turbulent growth rate in the initial jet stage. A rough estimate, based on the arguments of turbulent plume growth (ignoring compressibility effects) gives (for an engine jet diameter of 2 m) initial diameters of 4 m and 5 m for the outboard and inboard engine respectively. Correspondingly, the density depressions $(\Delta\rho/\rho)_0$ are 0.122 and 0.0816, since the value at the engine face is 0.51.

Figs. 3 and 4 show the subsequent evolution of plume-core distance r , angular spread $\Delta\theta$ of the sheared plume and overall dilution ratio A/A_{jet} . Since the radial pressure gradient intensifies towards the vortex center, the radial velocity of the plume is seen to increase with time, despite the progressive dilution. Thus, although it is not clear what distance r to pick as the end of the "capture" process, one can make a reasonable estimate of the "capture time". For instance, Eq. (10) indicates a finite time for $r \rightarrow 0$, and this can also be seen from the downwards turning of the $r(t)$ curves in Figs. 3 and 4. Perhaps a more reasonable capture time can be chosen as that at which r equals the original plume diameter D_0 (after allowing for the initial turbulent spread) or, what is nearly equivalent, that at which the plume has been fully spread into an annulus ($\Delta\theta = 360^\circ$). This gives for the outboard engine about 90 wing spans, by which time the overall dilution (including initial turbulent growth) is about $A/A_{jet} = 28$. The process is slower for the inboard engine, and it takes 350 wingspans to capture that plume, with an overall dilution ratio of 56.

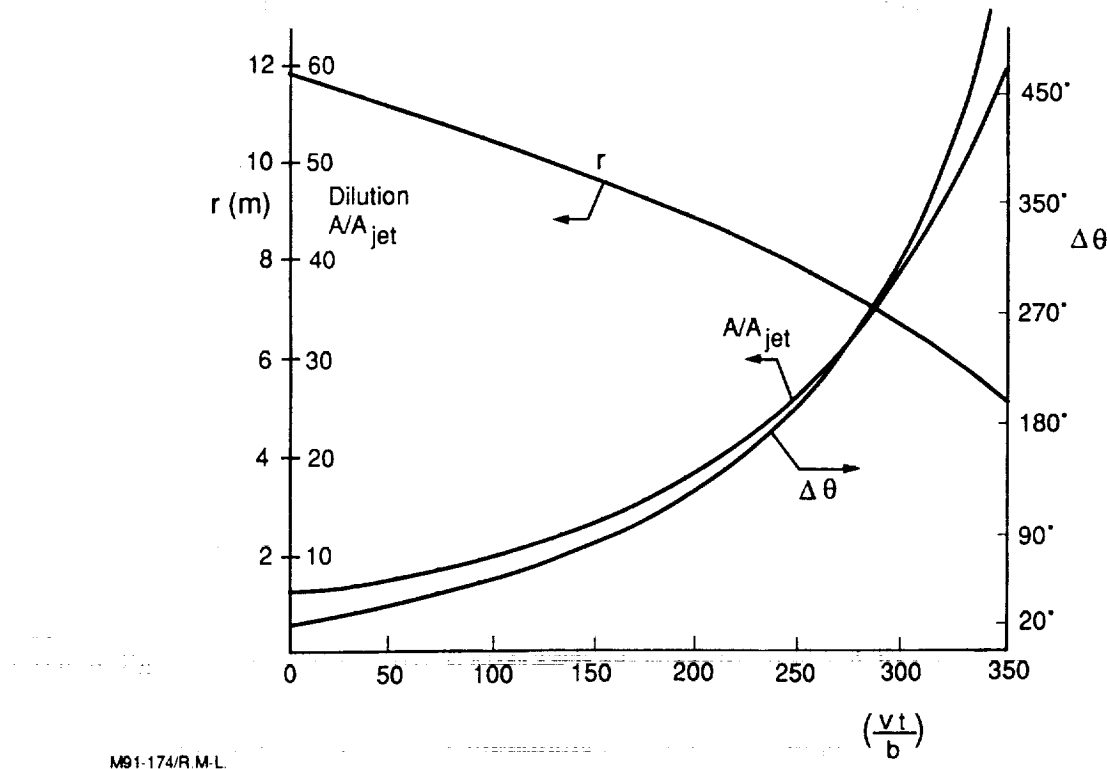


FIG. 3. Inner engine jet mixing and displacement. Initial jet diameter, $D_0 = 5$ m, distance from vortex core, $r_0 = 11.5$ m, and density difference, $(\Delta\rho/\rho)_0 = 0.0816$.

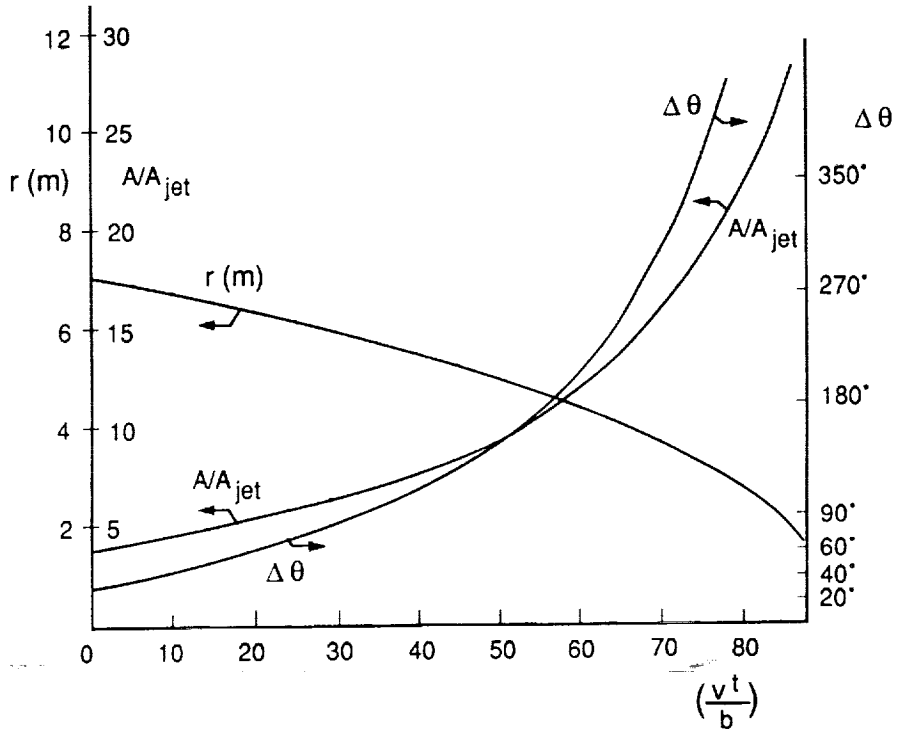


FIG. 4. Outer engine jet mixing and displacement. Initial jet diameter, $D_0 = 4$ m, distance from vortex core, $r_0 = 6.9$ m, and density difference, $(\Delta\rho/\rho)_0 = 0.122$.

The basic wake time scale (Table 7) is $\tau = (2AR/C_L)(b/V)$, in terms of which roll-up takes approximately 1.5τ and break-up takes 15τ (or, for our values of AR and C_L , 56 and 560 wingspans, respectively). We see therefore that a) the time for the plume capture process scales also as the basic time τ (see Eq. (10)), and b) for both engines, the capture time is intermediate between those for roll-up and break-up, as required for validity of the modeling approach.

It is interesting to observe, in connection with point a) above, that, for a given geometry and initial density defect, plume capture occurs at a fixed fraction of wake breakup time, independent of Mach number. Thus, of the two factors which are clearly different between transonic and supersonic aircraft (AR and M), only one, AR , remains to shorten the capture time in relation to wake lifetime. The reason why flight speed does not influence the time ratio is that all processes, including buoyant radial velocity and azimuthal vortex velocity, scale up together as v (see Eqs. (1) and (8)). This fact can be exploited for setting up experimental simulations of these phenomena in water tanks. The Mach number is still important however, in dictating deeper temperature and pressure minima in the supersonic case, and hence strengthening centripetal buoyancy when compared to natural buoyancy. Whether or not these stronger temperature depressions lead to enhanced condensation depends on the degree of dilution ultimately achieved by the captured plume.

The Last Stages of the Vortex Regime

As noted in Table 7, the wake is expected to survive as an organized cylindrical vortex cell for about 22 s. According to our analysis in above, the vortex cores at breakup time may contain a large fraction of the engine exhaust, at a dilution smaller than would have been expected in the absence of the vortices, and at a few degrees lower temperature. In attempting to extrapolate from this point, several questions arise:

- a. For how much longer will the confining effects of vorticity prevent or delay plume dispersion?
- b. Under what conditions will the higher plume vapor concentration and lower temperature lead to contrail formation?
- c. If condensation does occur, will the confinement time be long enough for significant heterogeneous chemical interactions to occur or for particles to grow to precipitation sizes?

Vortex Dynamics After Break-up Unfortunately, the fluid mechanics of the broken-up vortex system is still poorly understood, and so, only very rough estimates can be made on the important question a). Experimental and analytical stability results³⁶ indicate that reconnection due to growth of the Crow instability tends to produce irregular elongated ring vortices with aspect ratios of the order of 4:1. Dhanak and DeBernardinis³⁹ followed numerically the evolution of an elliptical ring vortex of this type and found that, after an oscillation in which the short and long axes interchange positions, the cores touch in the middle and reconnection can be expected, leading to two roughly 2:1 rings. These are then structurally stable, and oscillate as described. The time for subdivision of the original ring is (for our parameters) about 5 s.

If we can ignore temporarily the disturbing effects of wind shear, the smaller rings may continue to descend for some time, as they entrain new air by turbulent diffusion, and consequently grow in size and slow down. Glezer and Coles⁴⁰ did careful measurements of the evolution of circular turbulent rings in water, and showed that similarity exists in this motion provided a "virtual origin" is identified. In Appendix B we show that their results can be explained by means of a simple entrainment hypothesis, for which the entrainment parameter is derived from the data. As explained in Appendix B, the linear dimensions of the ring increase as $(1 + t/t_1)^{1/4}$, where $t_1 = \pi a_0 / 2\beta v_0$ (a_0 = initial core radius, v_0 = initial ring velocity, and $\beta \cong 0.01$). For an estimation, assume in our case an initial ring diameter 1.5 times the linear vortex spacing (i.e., 48 m), and an initial core diameter 0.1 of the ring diameter ($a_0 = 2.4$ m). Since v_0 must be close to the linear vortex pair velocity of 4.9 m/s, we calculate $t_1 = 76$ s.

The effects of atmospheric stratification must be also considered at this point. As the air mass enclosed within the vortex cell sinks into a stably stratified atmosphere, it will undergo adiabatic warming due to the higher pressures encountered, and will develop buoyancy. The effect of this buoyancy will be to eventually lead to an oscillatory vertical motion at the Brunt-Väisälä frequency,

$$N = \sqrt{\frac{g}{T_a} \left(\frac{dT_a}{dz} - \frac{dT}{dz} \right)} , \quad (15)$$

where $(-dT_a/dz)$ is the atmospheric lapse rate, and

$$-\frac{dT}{dz} = \frac{\gamma - 1}{\gamma} \frac{T}{H_p} \quad (16)$$

is the warming rate of the descending air (H_p is the pressure scale height of the atmosphere). However, a second effect of the descent-induced buoyancy is of interest to us. This is the production of vorticity opposite in sense to that of the wing vortices. The mechanism is clear from the 2-dimensional vorticity equation:

$$\frac{\partial \omega / \rho}{\partial t} + \bar{u} \cdot \nabla \left(\frac{\omega}{\rho} \right) = -\frac{1}{\rho} \nabla \left(\frac{1}{\rho} \right) \times \nabla p \quad (17)$$

The pressure gradient ∇p points vertically down, while $-\nabla 1/\rho$ is concentrated on the cell's edges, and points outwards from the cell. Thus, baroclinic vorticity is generating along the cell's edges, in the sense contrary to that in the vortex cores. At the time buoyancy stops the cell's descent, the total counter-vorticity created is also sufficient to cancel that of the wing vortex system, although its distribution is different. We can therefore expect the vortex system, whether in the form of the undisturbed cylindrical vortex cell, or of its successor ring vortices, to vanish in the vicinity of the lowest point of the Brunt-Väisälä cycle. This occurs when $Nt \cong \pi/2$, with the vertical descent distance being then $\Delta z = -w_0/N$ (w_0 = initial descent velocity). This behavior can be clearly seen in the water-tank data of Ref. 36, and was also assumed by, for example, Greene⁴¹ in his model of wake decay.

For our parameters, with $dT_a/dz = 0$, $H_p = 6380$ m, we calculate $N = 0.0210$ radians/s, and the stratification-induced vortex destruction can be expected to happen at $t = \pi/2N = 75$ s, after a total descent of $-\Delta z = 232$ m. Notice that this is 2.4 times longer than the time required for Crow instability to occur, so that a substantial period (44 s) can be anticipated during which the ring vortices formed after breakup can retain their individuality and continue to trap the engine effluent. The amount of turbulent entrainment into the rings in this time can now be estimated from our Appendix B results. With $t_1 = 76$ s, the ring linear dimensions will increase by $(1 + 44/76)^{1/4} = 1.12$, with additional dilution by a factor $(1.12)^3 = 1.41$.

Condensation Considerations A slight modification of the classical Appleman argument²¹ concerning contrail formation will help illustrate the potential vortex effects. Assuming that each kg of burnt fuel produces 1.29 kg of water vapor and 43 MJ of heat, of which the fraction $1 - \eta_{overall} \cong 0.5$ appears as sensible heat in the plume, and that the plume dilutes continuously by isobarically mixing with air at temperature T_a and moisture w_a (g/kg), its average temperature and moisture will evolve together according to

$$T = T_a + 17.7(w - w_a) \quad (18)$$

In Fig. 5, we have represented in a $T-w$ plot the water and ice vapor saturation lines (for an air density of 0.135 kg/m^3). The plume material will, according to Eq. (18) evolve down an inclined straight line of slope $1/17.7$ towards the existing atmospheric conditions (T_a , w_a). If this line intersects the water saturation line, droplets will condense on existing condensation nuclei, and

immediately freeze to form ice particles. These then persist even as the plume dilutes below the water saturation line, and will re-evaporate only after the ice saturation line is re-crossed.

In the presence of the vortex depression, however, both the ambient air and the plume gas are expanding and adiabatically cooling as they mix. Ignoring differences in the specific heat ratios, Eq. (18) must then be modified to

$$T = \left[T_a + 17.7(w - w_a) \right] \left(\frac{p}{p_a} \right)^{\frac{\gamma-1}{\gamma}} \quad (19)$$

where $\gamma = 1.4$. Tracing the plume trajectory in the $T-w$ plane now requires knowledge of the relationship between local pressure at the plume location and dilution at that point.

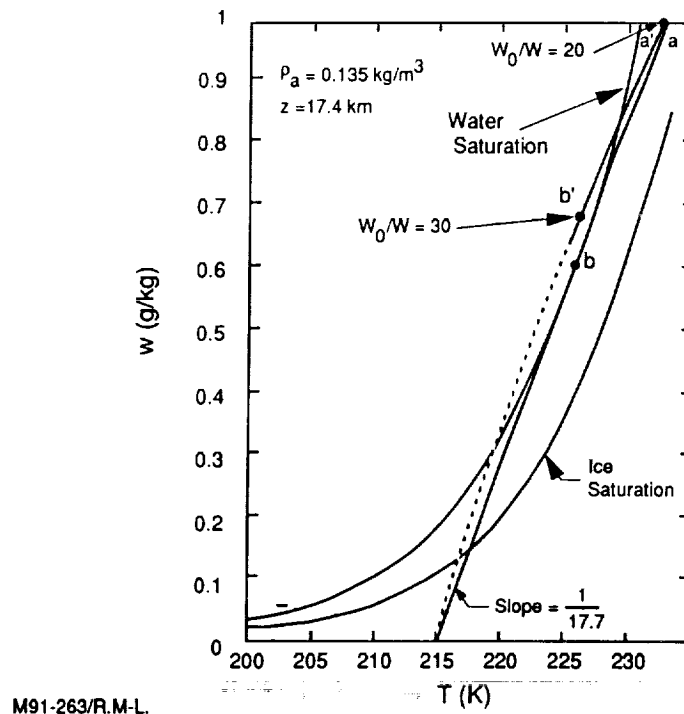


FIG. 5. Temperature—Water vapor content ($T-w$) plane with water and ice saturation curves overlaying exhaust dilution trajectories.

As an example, consider a dry stratosphere at $T_a = 215$ K which, as Fig. 5 shows, is at the threshold for contrail formation for this air density (plume expansion along abc). Using the plume-vortex interaction model we can calculate at each core-plume distance r the corresponding dilution ratio A/A_0 and temperature depression (Eq. (3)). Starting from an engine-exit value $w = 20$ g/kg, we can then calculate the new plume trajectory $a'b'c$ (Fig. 5), which shows definite contrail formation. The last portion of the $a'b'c$ curve is shown dotted, as it corresponds to the poorly understood process of vortex dissipation and final dilution.

The above results indicate an increase by about 2°C of the minimum atmospheric temperature required to form a contrail. The possible global significance of this is best appreciated by reference to Fig. 6, which is the result of straightforward application of Appleman's criterion. The region labelled ALWAYS corresponds to temperatures lower than that at points like c in Fig. 5, where contrails form even in dry air. The region labelled NEVER corresponds to temperatures greater than T_b in Fig. 5, where contrails would not form even in a saturated atmosphere. By inspection of Fig. 6, the cruising altitude range (17-20 km) for a Mach 2.4 aircraft contains a significant proportion of conditions lying no more than a few degrees from the ALWAYS limit. Thus there could be a noticeable impact on the frequency of contrail formation associated with wake-induced cooling. It may be, however, that a more significant effect than this contrail probability increase is the reduced dilution and extra confinement time provided by the wake vortices.

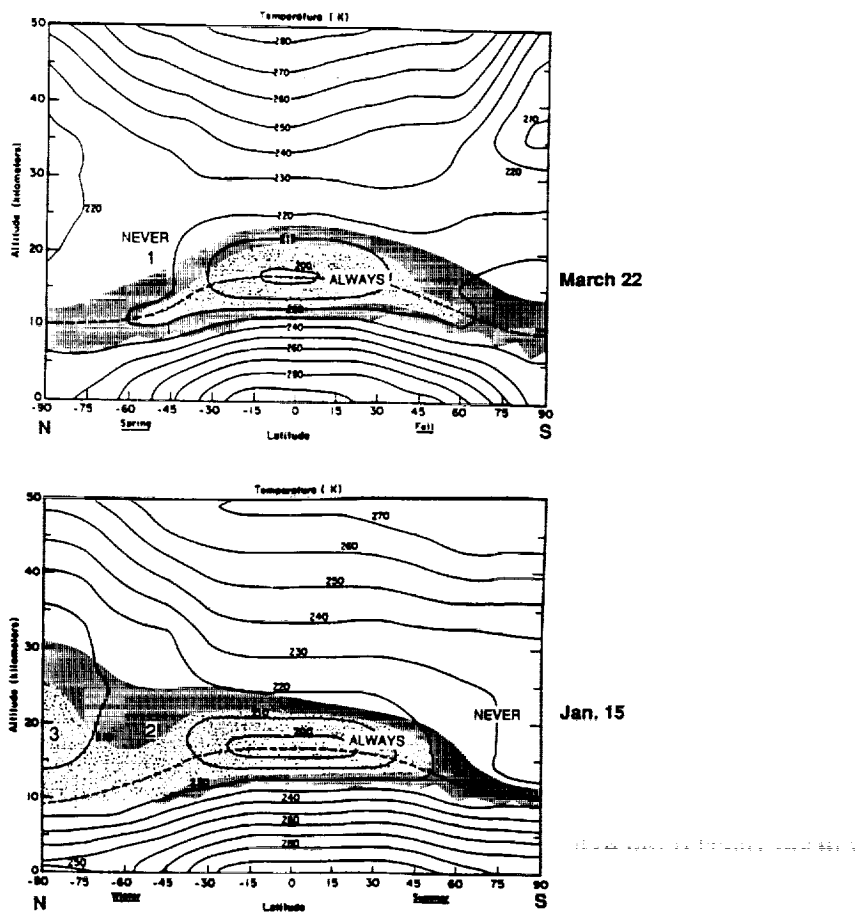


FIG. 6. Predictions using equilibrium, fully-mixed condensation algorithm.

The size to which the contrail ice particles can grow is mainly determined by the concentration of active condensation nuclei (cn) in the plume; kinetic limitations are less important, except perhaps for diameters over $10 \mu\text{m}$. Unfortunately, not much is known about cn production by

engines, and even less about their activation mechanisms. Knollenberg⁴² sampled a Sabreliner contrail in saturated ice conditions and estimated $10^{10}/\text{m}^{-3}$ active ccns at the engine exhaust plane. Rosen and McGregor⁴³ measured photoelectrically the total carbon particle concentration some 600 m behind an F-104 plane. Their data seem to indicate a total particle concentration of about $2.5 \times 10^{10}/\text{m}^{-3}$ extrapolated to the engine exhaust. On the other hand, Hoffmann and Rosen⁴⁴ encountered an 18 hour old SR-71 contrail which had sheared to a horizontal width of 20–0 km (but with a vertical thickness of only 200 m), and estimated emission of 3×10^{13} to $12 \times 10^{14} \text{ m}^{-3}$ particles greater than $0.01 \mu\text{m}$ (not necessarily all active). The fraction of all particles emitted which become active ccns is also uncertain. Hallett *et al.*²⁵ measured a conversion fraction of 1 to 3% for JP-4 fuel, but the 3% level was only achieved after aging for 20 hours.

From the example of Fig. 6, it is possible to have about 50% of the original vapor in the form of ice particles when the ambient temperature is near the contrail threshold. Assuming also 1.29 kg of water/kg of fuel and $p = 50 \text{ mb}$, $T_{exit} = 450 \text{ K}$, and letting $n (\text{m}^{-3})$ be the active nucleus concentration at the engine exhaust, we estimate an eventual mean particle size

$$\bar{R}(\mu\text{m}) \cong \left(\frac{10^{11}}{n} \right)^{1/3} \quad (20)$$

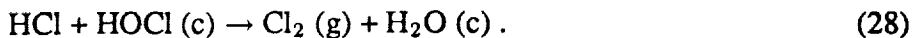
which, for the range of estimates of n given above implies \bar{R} values between 2 and $0.06 \mu\text{m}$. A $2 \mu\text{m}$ radius particle of pure water, falling through dry air at 210 K, would evaporate fully in about 10 s and settle no more than about 1 cm. This would indicate the lack of any contrail settling. However two modifying factors may occur in the case of an HSCT contrail. a) Lean-burner combustors, being developed for emissions reduction, will produce much less soot than conventional burners—perhaps by two or more orders of magnitude. Active ccn levels may be significantly lower still Hallett *et al.*²⁵. This may lead to ccn concentrations approaching background levels and hence (Eq. 20) to much larger particles. b) The extended confinement of exhaust products may lead to the formation of significant surface layers of nitric acid trihydrate (NAT) and other hydrated acid species on the ice particles (see Eqs. 21-28). This would lower their vapor pressure and essentially prevent re-evaporation, with the result of a much larger settling distance for a given particle size.

The acid gas processing of the condensed exhaust water begins with the plume/wake chemical effects described in the previous section. The chemistry modeled there includes the formation of acid gases and their precursors ($\text{HNO}_3/\text{N}_2\text{O}_5$ and $\text{H}_2\text{SO}_4/\text{SO}_3$). These gases are formed through the scavenging of exhaust OH radicals and reaction with entrained atmospheric O_3 . They are then available for heterogeneous chemistry processes that can change exhaust speciation through processes like:



temporarily removing plume and atmospheric acid gases from the gas phase or setting up the liberation of reservoir atmospheric chlorine:





The activation of plume/exhaust soot to ccn will occur on particles through their reaction with acid and oxidizing gases. In future work, we will model both this soot activation process and the kinetic nucleation and growth of contrail particles, a process which depends directly on the degree of plume/wake water vapor supersaturation, determined by the plume/wake temperature and entrainment/detrainment profiles and the number of active condensation nuclei. Particle formation and growth through the wake dispersal regime depend on more than the simple equilibrium H_2O condensation considered in the plume mixing and chemistry section. Clearly, in this heterogeneous chemical environment, the relevant condensation phenomena determine the degree to which gravitational settling can drop the particle and its associated acid gases and exhaust particulates to lower altitudes less conducive to ozone depletion.

SUMMARY AND CONCLUSIONS

The mixing, chemistry and condensation in the exhaust flowfield behind an HSCT were modeled as a first step in following the engine emissions to their eventual deposition in the atmosphere. Finite rate chemistry was simulated internal to an engine for conditions that are representative of engine cycles that would be used in propelling an HSCT. This simulation was used to calculate exhaust emissions at the engine exit plane where super-equilibrium concentrations of CO, NO, NO_2 , HNO_3 and OH were estimated to be present.

The exhaust emissions were followed from the engine exit plane using the standard plume flowfield code, SPF-2. The plume code was initialized using estimated emission indices or calculated exit plane concentrations. The chemical kinetics in the plume code were upgraded for these calculations to include the chemistry for atmospherically active species. NO_x in the plume was partially converted to HNO_3 through reaction with the OH radical to leave over 5% of the NO_x as HNO_3 600 m downstream of the exhaust exit. SO_2 was also oxidized (to SO_3) so that in excess of 10% of the SO_x is available for direct conversion to H_2SO_4 upon contact with condensed H_2O .

Equilibrium water condensation was also added to the upgraded plume code to begin to include some of the condensation phenomena needed to incorporate heterogeneous chemical reactivity in the plume. Contrail formation was predicted for several altitude-latitude-season combinations. These predictions based on equilibrium H_2O condensation were consistent with the Appleman algorithm for contrail occurrence.

The SO_3 , N_2O_5 and HNO_3 produced in the plume react and/or condense on the aqueous exhaust aerosols to form condensed acid solutions. These species as well as NO_2 and entrained atmospheric O_3 can also oxidize carbonaceous soot particles emitted with the exhaust. The oxidative activation of additional nucleation sites affects the size and quantity of condensed particles available for heterogeneous chemistry. The aerosols formed and activated in the plume are subjected to the vortical flowfield in the wake of the airplane, which transports and processes the particles and gases until the wake disperses.

The vortex wake due to a Mach 2.4 airplane was analyzed to estimate its effects on the transport and mixing of the exhaust emissions. For parameters representative of a low aspect ratio supersonic

aircraft, the circulation due to the rolled-up vorticity convects and shears the exhaust plume as it wraps the exhaust gases around the core. Since the emissions are warmer than the ambient, the pressure gradient generated by the vorticity attracts the less dense gas toward the core.

The vorticity has rolled up into a concentrated trailing vortex pair within about 56 wingspans behind the airplane. This vortex wake then propagates in the stratified atmosphere until the mutual interaction between the two vortices of the pair cause reconnection and the formation of elongated elliptical vortex rings at about 560 wingspans. The "capture" of the exhaust plumes by the vortices is dependent on engine placement but, for the case considered, the outboard exhaust is captured at about 90 wingspans while the inboard exhaust takes 350 wingspans. These values depend on the airplane configuration (aspect ratio) but not on its speed (Mach number). However, the speed does affect the intensity of the vortices, their pressure field, and thus the attraction and possibly the confinement of the exhaust.

The same chemistry that occurs in the plume continues as the exhaust is transported and mixed by the vorticity in the wake until wake dispersal, with subsequent atmospheric transport. The kinetics used in calculating the evolution of the plume will be incorporated into the vortex wake model to follow the chemistry from the capture of the exhaust through the dispersal of the wake. The simplified analysis performed in the present study provides insight and estimates of the dominant processes that are occurring throughout the wake and further can be used to generate first order estimates of the flow properties. However it is apparent that the several individual vorticity-induced phenomena are, in fact, strongly coupled and a more detailed, presumably numerical, analysis will be necessary for quantitative estimation of the evolution of the emitted exhaust gases and their transport.

ACKNOWLEDGMENTS

We would like to acknowledge the support of the NASA High Speed Research Program (HSRP) Atmospheric Effects of Stratospheric Aircraft project through contract NAS1-19161. We are also grateful for the engine data provided by F.H. Krause and J.A. Matulaitis of G.E. Aircraft Engines and K. L. Hasel of Pratt & Whitney. We benefited from useful discussions with A.H. Epstein.

REFERENCES

1. Boeing Commercial Airplane Co., "High-speed civil transport study" NASA Contractor Rep. CR-4233, 116 pp., 1989.
2. Douglas Aircraft Co., "Study of high-speed civil transports" NASA Contractor Rep. CR-4235, 168 pp., 1989.
3. Johnston, H.S., Prather, M.J. and Watson, R.T., "The Atmospheric Effects of Stratospheric Aircraft: A Topical Review," NASA Ref. Publ. 1250, January 1991.
4. Douglass, A.R., Carroll, M.A., DeMore, W.B., Holton, J.R., Isakson, I.S.A., Johnston, H.S. and Ko, M.W.K., "The Atmospheric Effects of Stratospheric Aircraft, A Current Consensus," NASA Ref. Publ. 1217, January 1991.
5. Weisenstein, D., Ko, M.K.W., Rodriguez, J.M. and Sze, N.D., "Impact of Heterogeneous Chemistry on Model-Calculated Ozone Changes due to HSCT Aircraft," to be submitted to *Geophys. Res. Letts.*

6. Papamoschou, D., and Roshko, A., "Observations of Supersonic Free Shear Layers," Paper AIAA-86-0162 from AIAA 24th Aerospace Sci. Meeting, Reno, NV, 1986.
7. Gutmark, E., Schadow, K.C. and Wilson, K.J., "Mixing Enhancement in Coaxial Supersonic Jets," Paper AIAA-89-1812 from AIAA 20th Fluid Dynamics, Plasma Dynamics, and Lasers Conference, Buffalo, NY, 1989.
8. Hoshizaki, H., Anderson, L.B., Conti, R.J., Farlow, N., Meyer, J.W., Overcamp, T., Redler, K.O., and Watson, V., "Aircraft Wake Microscale Phenomena," Chapter 2 in CIAP Monograph 3, Department of Transportation Washington, DC, DOT-TST-75-53.
9. Overcamp, T.J. and Fay, J.A., "Dispersion and Subsidence of the Exhaust of a Supersonic Transport in the Stratosphere," *J. Aircraft*, Vol. 10, 1973, pp. 720-728.
10. Wofsy, S.C., Salawitch, R.J., Yatteau, J.H., McElroy, M.B., Gandrud, B.W., Dye, J.E. and Baumgardner, D., "Condensation of HNO₃ on Falling Ice Particles: Mechanism for Denitrification of the Polar Stratosphere," *Geophys. Res. Letts.*, Vol. 17, March Supplement 1990, pp. 449-452.
11. Fahey, D.W., Kelly, K.K., Kawa, S.R., Tuck, A.F., Lowenstein, M., Chan, K.R. and Heidt, L.E., "Observations of Denitrification and Dehydration in the Winter Polar Stratospheres," *Nature*, Vol. 344, 1990, pp. 321-324.
12. Yousefian, Y., Weinberg, M.H. and Haimes, R., "PACKAGE: A Computer Program for the Calculation of Partial Chemical Equilibrium/Partial Chemical Rate Controlled Composition of Multiphase Mixtures Under One-Dimensional Steady Flow," Aerodyne Research, Inc., Report No. ARI-RR-177, February 1980.
13. Tsang, W. and Hampson, R.F., "Chemical Kinetic Data Base for Combustion Chemistry. Part I. Methane and Related Compounds," *J. Phys. and Chem. Ref. Data*, Vol. 15, 1986, pp. 1087-1279.
14. Miller, J.A. and Bowman, C.T., "Mechanism and Modeling of Nitrogen Chemistry in Combustion," *Prog. Energy Combust. Sci.*, Vol. 15, 1989, p. 287.
15. Matulaitis, J.A. and Krause, F.H., GE Aircraft Engines; Cincinnati, OH; personal communications, 1990.
16. McGregor, W.K., Seiber, B.L. and Few, J.D., "Concentrations of OH and NO in YJ93-GE-3 Engine Exhausts Measured In Situ by Narrow-Line UV Absorption," *Proceedings of the Second Conference on CIAP*, 1972, pp. 214-228. Few, J.D., and Lowry, H.S., III "Reevaluation of Nitric Oxide Concentration in Exhaust of Jet Engines and Combustors," AEDC-TR-80-65, 1981.
17. Dash, S.M., Pergament, H.S. and Thorpe, R.D., "The JANNAF Standard Plume Flowfield Model: Modular Approach, Computational Features and Preliminary Results," *Proceedings of the JANNAF 11th Plume Technology Meeting*, CPIA Pub. 306, 1979, pp. 345-442.
18. 1990 Conditions Atmospheric Chemistry Data, Atmospheric and Environmental Research, personal communication, 1990.

19. The emission index for NO_x is reported as the mass equivalent of NO_2 . This notation ($\text{EI}_{(\text{NO}_2)}\text{NO}_x$) resolves any possible ambiguities associated with NO_x EIs and allows the reporting convention in terms of NO_2 to be explicitly indicated. Clearly, EIs for NO and NO_2 can only be meaningfully summed to NO_x if the preceding subscripts match.
20. An emission number of 5 was chosen as it represents a design goal of the NASA HSRP program and has been used in initial atmospheric impact assessment calculations—see Ref. 2.
21. Appleman, H.S., "The Formation of Exhaust Condensation Trails by Jet Aircraft," *Bull. Amer. Met. Soc.*, Vol. 34, January 1953, pp. 14-20. Also U.S. Air Force Air Weather Service, "Forecasting Aircraft Condensation Trails," Chapter 1 of the Air Weather Service Manual 105-100 (1960), reissued as Report No. AWS/TR-81001, September 1981.
22. DeMore, W.B., Sander, S.D., Golden, D.M., Molina, M.J., Hampson, R.F., Kurylo, M.J., Howard, C.J. and Ravishankara, A.R., "Chemical Kinetics and Photochemical Data for Use in Stratospheric Modeling," JPL Publication 90-1, Jet Propulsion Laboratory, Pasadena, CA, January 1990.
23. Ahkter, M.S., Chughatai, R.A. and Smith, D.M., "Reaction of Hexane Soot with $\text{NO}_2/\text{N}_2\text{O}_4$," *J. Phys. Chem.*, Vol. 88, 1984, pp. 5334-5342.
24. Smith, D.M., Welch, W.F., Jassim, J.A., Chughatai, A.R. and Stedman, D.N., "Soot-Ozone Reaction Kinetics: Spectroscopic and Gravimetric Studies," *Appl. Spectros.*, Vol. 42, Nov./Dec. 1988, pp. 1473-1482.
25. Hallett, J., Hudson, J.G. and Rogers, C.F., "Characterization of Combustion Aerosols for Haze and Cloud Formation," *Aerosol Sci. Tech.*, Vol. 10, 1989, pp. 70-83. Also Hudson, J.G., Hallett, J. and Rogers, C.F., "Field and Laboratory Measurements of Cloud-Forming Properties of Combustion Aerosols," *J. Geophys. Res.*, Vol. 96, June 1991, pp. 10,847-10,859.
26. CIAP, 1975, Monograph 2 "Propulsion Effluents in the Stratosphere," DOT-TST-75-52, 485 pp. NTIS, Springfield, VA.
27. CIAP, 1975, Monograph 3 "The Stratosphere Perturbed by Propulsion Effluents," DOT-TST-75-53, 765 pp. NTIS, Springfield, VA.
28. Hoshizaki, H.L., Anderson, L.B. and Conti, R.J., "High Altitude Aircraft Wake Dynamics," *Proc. 2nd Conf. on CIAP*, DOT-TSC-OST-73-4, 1972, pp. 263-284.
29. Holdeman, J.D., "Dispersion and Dilution of Jet Aircraft Exhaust at High-Altitude Flight Conditions," *J. Aircraft*, Vol. 11, 1974, pp. 483-487.
30. Nielsen, J.N., Stahara, S.S. and Woolley, J.P., "Injection and Dispersion of Engine Exhaust Products by Trailing Vortices for Supersonic Flight in the Stratosphere," Paper AIAA 74-42 from AIAA 12th Aerospace Sci. Meeting, 1974.
31. Farlow, N.H., Watson, V.R., Lowenstein, M. and Chan R.L., "Measurement of Supersonic Jet Aircraft Wakes in the Stratosphere," Second Int. Conf. on Environmental Impact of

Aerospace Operations in the High Atmosphere, Am. Meteorology Soc., Boston, 1974, pp. 53-58.

32. Scorer, R.S. and Davenport, L.J., "Contrails and Aircraft Downwash," *J. Fluid Mech.*, Vol. 43, 1970, pp. 451-464.
33. Donaldson, C. DuP. and Bilanin, A., "Vortex Wake of Conventional Aircraft," AGARD-GRAPH 204, 1975.
34. Widnall, S.E., "The Structure and Dynamics of Vortex Filaments," *Annual Rev. Fluid Mech.*, Vol. 7, 1975, pps. 141-165.
35. Bera, R.K., "Do Inviscid Vortex Sheets Roll-up?" Project Document CF 9010, National Aeronautical Laboratory, Bangalore, India, May 1990.
36. Liu, H.T. and Srnsky, R.A., "Laboratory Investigations of Atmospheric Effects on Vortex Wakes," Flow Research, Inc., Flow Tech. Rep. No. 497, February 1990.
37. Schetz, J., *Injection and Mixing in Turbulent Flow*, *Prog. Aero. and Astro.*, Vol. 68, 1980, pp. 52-61.
38. Morton, B.R., Taylor, G.I. and Turner, J.S., "Turbulent Gravitational Convection from Maintained and Instantaneous Sources," *Proc. Royal Soc. London A*, Vol. 234, 1956, pp. 1-23.
39. Dhanak, M.R. and DeBernardinis, B., "The Evolution of an Elliptic Vortex Ring," *J. Fluid Mech.*, Vol. 109, 1981, pp. 189-216.
40. Glezer, A. and Coles, "An Experimental Study of a Turbulent Vortex Ring," *J. Fluid Mech.*, Vol. 211, 1990, pp. 243-283.
41. Greene, G.C., "An Approximate Model of Vortex Decay in the Atmosphere," *J. Aircraft*, Vol. 23, July 1986, pp. 566-573.
42. Knollenberg, R.G., "Measurement of the Growth of the Ice Budget in a Persisting Contrail," *J. Atm. Sci.*, Vol. 29, October 1972, pp. 1367-1374.
43. Rosen, J.M. and McGregor, R., "Jet Engine Soot Emission Measured at Altitude," *J. Aircraft*, Vol. 11, 1974, pp. 243-245.
44. Hoffmann, D.J. and Rosen, J.M., "Balloon Observations of a Particle Layer Injected by a Stratospheric Aircraft at 23 km," *Geophys. Res. Letts.*, Vol. 5, June 1978, pp. 511-514.

APPENDIX A

Buoyant Turbulent Jet in a Co-flow

Consider the jet depicted in Fig. A1, issuing with some velocity and temperature excess into a parallel stream. A top-hat model of the distributions will be adopted for simplicity. The fluxes of axial momentum and of enthalpy will be conserved, while the vertical momentum flux increases with distance due to the buoyancy. The convection velocity will be approximated by the external velocity u_e . We then have

$$\rho_e u_e (u - u_e) \frac{\pi D^2}{4} = F = \text{constant} \quad , \quad (A.1)$$

$$\rho_e u_e c_p (T - T_e) \frac{\pi D^2}{4} = Q = \text{constant} \quad , \quad (A.2)$$

$$\frac{d}{dx} \left[\rho_e u_e w \frac{\pi D^2}{4} \right] = \rho_e \frac{T - T_e}{T_e} g \frac{\pi D^2}{4} \quad . \quad (A.3)$$

These equations must be supplemented by one which describes the turbulent diffusion and its effect on jet growth. In general,

$$u_e \frac{dD^2}{dx} = 4D_t \quad (A.4)$$

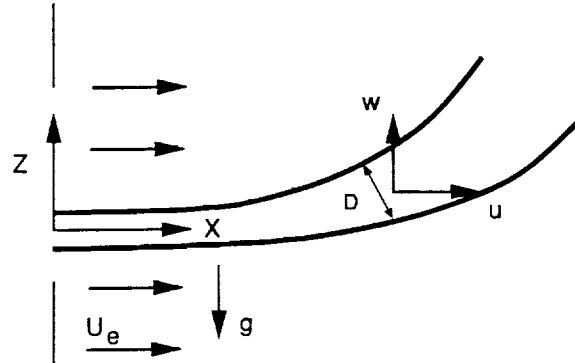


FIG. A1. Buoyant jet geometry.

Where D_t is the "turbulent diffusivity". For a non-buoyant jet, a reasonable approximation is³⁷ $D_t = kD(u - u_e)$, with $k \approx 0.016$. For a non-flowing cylindrical plume the Morton-Taylor-Turner³⁸ model gives $D_t = \alpha Dw$ ($\alpha \approx 0.3$). These two limiting forms can be interpolated by assuming

$$D_t = KD \sqrt{a^2 w^2 + (u - u_e)^2} \quad , \quad (A.5)$$

where $a = \alpha/K \approx 19$.

For the case of an engine exhaust in flight ($u_e = v$), F represents the engine's thrust, and Q its thermal energy output. Hence, if η_{ov} is the overall propulsive efficiency,

$$\frac{Fu_e}{Q} = \frac{\eta_{ov}}{1 - \eta_{ov}} \quad , \quad (A.6)$$

To integrate these equations, $u - u_e$ from Eq. (A.1) and w from Eq. (A.3) (after integrating) are substituted into (A.5) to give D_t as a function of D and x . This is then substituted in (A.4), and integration gives the results quoted in Eqs. (4a)-(4d).

APPENDIX B

A Model for Turbulent Vortex Ring Evolution

The similarity results obtained experimentally by Glezer and Coles⁴⁰ for the growth and slowing down of a turbulent vortex ring can be understood and extrapolated by a simple model based on an entrainment hypothesis. We assume:

a. The vortex core cross section increases at a rate proportional to its own radius and to the ring velocity. With reference to Fig. B1.,

$$\frac{d(\pi a^2)}{dt} = \beta a v \quad . \quad (B.1)$$

where β is an empirical constant.

b. Geometrical similarity is preserved, i.e., R and a grow in the same proportion:

$$\frac{a}{a_0} = \frac{R}{R_0} \quad . \quad (B.2)$$

c. The vertical momentum is preserved. In combination with (B.2), this gives

$$a^3 v = a_0^3 v_0 \quad . \quad (B.3)$$

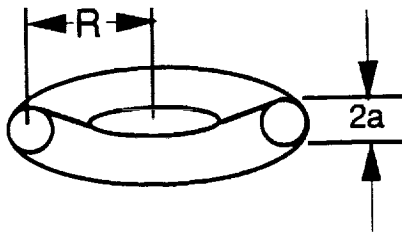


FIG. B1. Geometry of descending vortex ring.

Eqs. (B.1), (B.2) and (B.3) can be combined to obtain explicit laws for the time histories of the various quantities, including the distance x travelled by the ring. Ref. 37 introduced the distance x_0 and time t_0 which act as the origin for the measured self-similarity. These quantities are both negative, i.e., the "virtual origin" occurs upstream of the point of creation of the vortex ring. Our analytical results, of the same form as the data trends, are

$$\frac{a}{a_0} = \frac{R}{R_0} = \left(1 - \frac{t}{t_0}\right)^{1/4} \quad , \quad (B.4)$$

$$\frac{v}{v_0} = \left(1 - \frac{t}{t_0}\right)^{-3/4} \quad , \quad (B.5)$$

$$\frac{x}{x_0} = 1 - \left(1 - \frac{t}{t_0}\right)^{1/4} \quad , \quad (B.6)$$

where

$$t_0 = -\frac{\pi a_0}{2\beta v_0} \quad , \quad (B.7)$$

$$x_0 = -\frac{2\pi a_0}{\beta} \quad . \quad (B.8)$$

In Glezer's experiments,⁴⁰ $v_0 = 128$ cm/s for the piston producing the rings. For the ring itself, we take $v_0 = 64$ m/s. Also, $R_0 = 0.953$ cm, and $a_0 \simeq 0.2R_0$, as estimated from the data. The measured virtual origin parameters were

$$t_0 = -0.44 \text{ s} \quad , \quad x_0 = -145 \text{ cm} \quad .$$

Using these results, (B.5) gives $\beta = 0.00825$, while (B.6) gives $\beta = 0.0106$. Thus the model appears to give a reasonable description of the data using

$$\beta \simeq 0.01 \quad . \quad (B.9)$$

Chapter 3

Plume Chemistry and Dispersion Modeling to Evaluate the Atmospheric Effects of Stratospheric Aircraft *

INTRODUCTION

Our modeling of the dispersion of the wake has concentrated on: a) developing, testing and utilizing a Lagrangian air parcel model to simulate the behavior of chemical constituents in the wake regime of a plume; b) modifying and utilizing an existing radiation code at AER to calculate the net heating/cooling of aircraft plumes in the same regime. The wake regime starts after breakdown of the plume vortices; expansion of the plume is still controlled by internal energy dissipation in the wake regime. After about 1,000 - 3,000 seconds, the plume expansion and motion are controlled primarily by the dynamics of the background atmosphere.

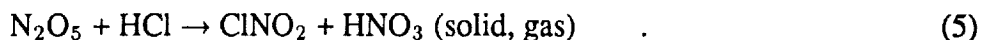
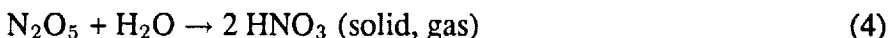
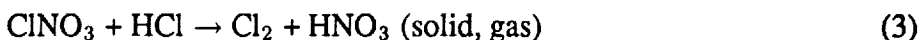
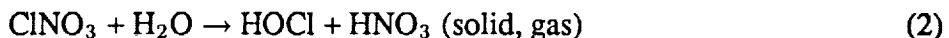
Lagrangian Box Model

The Lagrangian box model solves an equation of the form (Gelinas and Walton, 1974):

$$\frac{d n_i(t)}{dt} = P_i - L_i - \left(\frac{d \ln V(t)}{dt} \right) [n_i(t) - n_i^a(t)] + R_i(t) \quad , \quad (1)$$

where P_i and L_i denote the chemical production and loss for species i , $n_i(t)$ and $n_i^a(t)$ represent the concentrations of species i within the plume and in the background atmosphere, respectively, and R_i denotes other production/loss processes, such as, for example, denitrification. The factor $d \ln V(t)/dt$ represents the entrainment parameter, where the volume $V(t)$ is defined as that physical volume which contains all the initial plume molecules.

Previous calculations of the photochemistry in the wake regime (Gelinas and Walton, 1974; Hoshizaki *et al.*, 1975) concluded that very little photochemical activity took place during the wake regime, and the time development of the mixing ratios of trace species was controlled primarily by plume expansion and entrainment of air from the background atmosphere. Chemical schemes have however changed since that period of time, particularly in the kinetics of species such as ClNO_3 and N_2O_5 . Furthermore, the recent studies of the photochemistry of the polar stratosphere have indicated the importance of heterogeneous reactions occurring in the surface of Polar Stratospheric Clouds (PSCs). The following reactions have been suggested (Wofsy, 1978; Solomon *et al.*, 1986; McElroy *et al.*, 1986; Tolbert *et al.*, 1987; 1988a, b; Molina *et al.*, 1987; Leu, 1988a, b; Rodriguez *et al.*, 1988):



Reactions (2) - (5) have been observed on ice or nitric acid tri-hydrate particles at very fast rates. Fast rates for reaction (4) have been observed on sulfuric acid solutions, with the magnitude fairly independent of water content (Mozurkewich and Calvert, 1988; Van Doren *et al.*, 1991).

* Work performed by Atmospheric and Environmental Research, Inc. under subcontract to ARI.

The new kinetic data could change the conclusions of the assessment undertaken in the mid-70's. In particular, heterogeneous reactions occurring on contrails could alter the partitioning of nitrogen species, and favor production of nitric acid. Enhanced concentrations of nitric acid could in turn favor production of nitric acid tri-hydrate contrails, particularly since these tri-hydrates form at about 5K above the freezing point of water.

We have developed a Lagrangian box model which includes entrainment of background air. This model includes complete gas-phase chemistry of HO_x , NO_x , Cl_x , Br_x , ozone, methane and ethane. We also include in the model reactions (2) - (5). As discussed below, other heterogeneous processes have also been included for purposes of exploration of their impact. The model has been used to revisit the issues addressed by the CIAP panel during the mid-70's. In particular, we have addressed and will continue to address the following issues:

- a. What is the partitioning of nitrogen species during the wake regime, and in particular, how much NO_x is converted to HNO_3 ?
- b. What is the impact of heterogeneous chemistry on the conversion of NO_x to HNO_3 ?
- c. What is the impact of entrainment on the chemical development of species within the wake?
- d. What other heterogeneous processes could affect the chemical behavior of species in the wake?
- e. What is the ozone loss in the wake?
- f. What is the time development of other radiatively active species, such as water?

We have carried out exploratory calculations to address some of the above issues. These calculations and results are presented in the following. In particular, we look at two regimes: a) calculations are carried out for the first hour of the wake regime, assuming very fast entrainment, and testing the sensitivity to different assumptions about heterogeneous chemistry; b) the sensitivity of the calculations to the entrainment parameterization and scale-dependent dispersion is also examined; in particular, we extend some of the calculations to a time period of two days to illustrate the time development of important trace species for different dispersion rates. Some of the results described below were presented at the HSRP workshop in Virginia Beach, January, 1991; other results will be presented at the HSRP workshop in Virginia Beach, May, 1992.

Radiative Calculations

The final altitude of deposition of aircraft effluents depends on a whole suite of dynamical and radiative processes acting at both wake and synoptic scales. The ascent/descent of the aircraft plume and its dispersion is determined in part by processes such as buoyant rise, gravitational collapse, wind shear, and turbulent dispersion (Hoshizaki *et al.*, 1975; Miake-Lye *et al.*, 1991). The interaction among these processes is still poorly quantified, in part due to the scarcity of data on aircraft wakes at stratospheric altitudes.

Another potentially important process was suggested by Overcamp and Fay, (1973). These authors pointed out that the concentrations of radiatively important trace species, such as water and ozone, could be greatly perturbed in aircraft wakes. In particular, a decrease in ozone would reduce the amount of UV absorption and direct heating of the plume, yielding a net cooling of the plume.

Similarly, enhanced concentrations of water or CO₂ would increase the amount of IR cooling, and again yield a net cooling of the plume. Such net cooling could then lead to a net downward vertical velocity of the wake relative to the background atmosphere, as the perturbed air mass moves to maintain its potential temperature. The vertical velocity would be given by

$$w(\text{km/day}) = -\frac{Q}{G} \quad (6)$$

where w is the vertical velocity, Q (K/day) is the differential cooling rate of the wake relative to the background atmosphere, and G (K/km) is the so-called stability parameter, *i.e.*, the vertical gradient in potential temperature. The value of G is fairly close to 10 K/km in the lower stratosphere.

We have modified the radiative portion of our interactive 2-D model to calculate the expected differential cooling of aircraft wakes. We present calculations below of this differential cooling as a function of season and altitude, and for different assumptions about water enhancement and wake thickness.

PHOTOCHEMICAL CALCULATIONS

Calculations were carried out at an altitude of 18 km, for conditions representative of 47°N, June 1, starting at noontime. Our model of the wake regime will eventually be initialized from the results of the ARI model of the vortex regime. Since the ARI team has concentrated in modeling the jet regime, we have taken their calculated values for NO, NO₂, NO₃, N₂O₅ and HNO₃ at a distance of 2000 ft from the nozzle, and simply diluted them to obtain a factor of 100 dilution from the nozzle to the beginning of the wake regime. Values for ozone, HO_x species, as well as other calculated species were initialized to those calculated in our 2-D model for the above latitude and season. No dilution was applied to ozone, since the results of the ARI calculations at 2000 ft are very similar to the ozone concentrations in the background atmosphere. We also did not dilute OH and HO₂, since these species have very short photochemical lifetimes. Adopted initial conditions for NO + NO₂, HNO₃, N₂O₅, and O₃ are given in Table 1, as well as values for the background atmosphere taken from our 2-D model.

1. The first hour

a. Description of calculations

The chemical evolution of different trace species was first calculated for a period of 1 hour, with a time resolution of 50 seconds. This period of time was used to explore the sensitivity to heterogeneous processes, particularly on contrails, since it is unlikely that ice particles would last longer than one hour.

Entrainment of background air into the wake air mass can occur through turbulent diffusion controlled both by dissipation of the internal kinetic energy and the turbulence of the background atmosphere. There is very little information on these processes for conditions in the lower stratosphere. The calculations for the first hour assumed a constant value for the entrainment parameter:

$$\frac{d \ln V(t)}{dt} = \frac{1}{t} \quad (7)$$

We have adopted a value of 780 seconds for t , which corresponds to an expansion of the volume by a factor of 100 in 1 hour. Calculations in the next subsection show results for slower entrainment rates.

The cases considered in our calculations are summarized in Table 2. Cases 1 and 2 assume only gas-phase chemistry. Although large amounts of water are emitted by the aircraft, condensation into contrails and subsidence could remove a large portion of this water. We have therefore considered two extreme possibilities: all the water emitted by the engine has been condensed out, and the water mixing ratio is equal to that of the background atmosphere (Case 1), or the water emitted by the engine stays in the wake, and the mixing ratio is given by the appropriate dilution factor (Case 2).

The heterogeneous reactions (2) - (5) are included in Cases 3 and 4 at rates similar to those utilized in our modeling of the Antarctic stratosphere (Rodriguez *et al.*, 1989). In Case 3 we assume that no contrails are formed, and heterogeneous chemistry occurs only in the background sulfate aerosol layer presumably already entrained into the wake. In Case 4 we assume that all the water emitted by the aircraft has been condensed into cloud particles of $1 \mu\text{m}$ radius. We assume an initial concentration of 10^5 cm^{-3} for concentration nuclei, of which 1% are activated. With these assumptions, the available reacting surface concentration in the contrails is about a factor of 10^4 higher than in the background sulfate aerosol layer, and heterogeneous reactions could occur very fast. We assume that contrails last for the duration of the calculations, but allow the density of particles to decrease with time in inverse ratio to the increase in plume volume.

The reaction of N_2O_5 with water (reaction 4) could be an important contributor to the conversion of NO_x to HNO_3 . The rate of this reaction is however limited by the rate of conversion of NO_2 to NO_3 through the reaction



which is very slow for stratospheric temperatures. Experiments of uptake of NO_2 on liquid surfaces (Lee and Tang, 1988) indicate an uptake coefficient of 6×10^{-4} , although this value could be even higher. If uptake of NO_2 could lead to reaction (8) occurring heterogeneously, then the conversion of NO_2 to NO_3 , N_2O_5 and eventually HNO_3 could be accelerated. Cases 5 and 6 were chosen to study this possibility. We assume a reaction efficiency of 6×10^{-4} for reaction (8) at an ozone mixing ratio of 2.9 ppmv. Furthermore, we assume that this reaction efficiency is proportional to the ozone mixing ratio. In Case 5, the reaction is assumed to take place on background sulfate aerosols, while in Case 6 the reaction takes place on contrails.

b) Results

The first question we seek to address is how much repartitioning of nitrogen species occurs in the wake regime due to photochemistry. The results in Table 3 shed light on this issue. The table shows the ratio of calculated NO_x ($\text{NO}_x = \text{NO} + \text{NO}_2 + \text{NO}_3 + 2\text{xN}_2\text{O}_5 + \text{HO}_2\text{NO}_2 + \text{ClNO}_3$) and HNO_3 after 1 hour to that calculated if no chemistry took place, and mixing ratios of the above trace gases were only affected by entrainment of background air. We see that for the first three cases the results are essentially the same. Therefore, there is little photochemical repartitioning of nitrogen species if we adopt only gas-phase chemistry, or even with heterogeneous chemistry occurring only on background sulfate aerosols. On the other hand, considerable repartitioning occurs if we assume heterogeneous chemistry occurring on contrails (Cases 4, 5, and 6), with final concentrations of HNO_3 enhanced by up to a factor of 2 over the entrainment-only values.

The calculated time development of NO_x and HNO_3 is shown in Figures 1 and 2, respectively, for Cases 4, 5 and 6. The calculated concentrations of OH , NO_x , HNO_3 , and O_3 at the end of one hour are compared to values in the background atmosphere in Table 4. Inclusion of

heterogeneous chemistry on contrails leads to an enhancement of HNO_3 over background values, even if we allow for entrainment. Furthermore, heterogeneous conversion of NO_2 to NO_3 leads to further enhancement of HNO_3 and reductions in NO_x during the first fifteen minutes; if this reaction takes place on contrails, almost compete conversion occurs in the first few minutes (Case 6). We also note that, except for Case 6, NO_x concentrations are still enhanced relative to the background after 1 hour of the wake regime. This is due to the large initial concentrations of NO_x ; further entrainment and mixing in the mesoscale regime will eventually bring the NO_x concentrations to background values.

An interesting feature of the photochemistry in the wake regime is the behavior of OH . For Cases 1 - 3, the large concentrations of NO_x lead to reductions in OH relative to the background, due to the reaction of OH with NO_2 . In the presence of heterogeneous chemistry on contrails, however, the OH concentrations are enhanced. This is due to an increase in the HO_x source due primarily to reactions (2) and (4), followed by photolysis of HOCl and nitric acid. Such enhanced concentrations of OH accelerate the conversion of NO_x to HNO_3 . In Case 6, rapid conversion of N_2O_5 and ClNO_3 to HNO_3 reduces the magnitude of this source and the OH enhancement.

The calculated time development of ozone in the parcel is illustrated in Figure 3 for Cases 4 - 6. Ozone decreases during the first minute due to enhanced NO_x and HO_x cycles. The decrease in ozone concentration is at most 15% during this period of time. For the rest of the hour, entrainment from the background atmosphere bring the ozone values to background levels by the end of the hour. Direct removal of ozone in the wake will not contribute to ozone reductions on a global scale.

2. Scale-dependent Dispersion: The first two days

a. Description of Calculations

Our previous calculations assumed a constant, scale-independent entrainment time constant. We have also implemented a scale-dependent dispersion, following the formalism of Gelinas and Walton (1974). In this formalism, the wake is treated as a Gaussian plume, and its time-dependent volume, $V(t)$, is assumed to expand according to the expression:

$$\frac{d \ln V(t)}{dt} = \frac{K_h}{\sigma_h^2} + \frac{K_v}{\sigma_v^2}, \quad (9)$$

In (9), the vertical and horizontal dimensions σ_v , σ_h are given by the equations:

$$\begin{aligned} \frac{d\sigma_h^2}{dt} &= 2K_h(t) \\ \frac{d\sigma_v^2}{dt} &= 2K_v(t) \end{aligned} \quad (10)$$

The horizontal and vertical eddy coefficients K_h , K_v can be assumed constant, or be related to the dimensions by expressions consistent with similarity theory. In particular, Gelinas and Walton suggest the expression:

$$K = \left(\frac{1}{b\epsilon^{1/3}\sigma^{4/3}} + \frac{1}{K_m} \right)^{-1}, \quad (11)$$

where b is a constant of order 1, ϵ the energy dissipation rate, and K_m an asymptotic value for the eddy coefficient appropriate for large wake sizes.

It is difficult to obtain reliable estimates for the parameters in equation (11). The large-scale distribution of trace gases in the stratosphere can be obtained with horizontal "eddy" coefficients of order $10^9 - 10^{10} \text{ cm}^2 \text{s}^{-1}$ (Ko et al., 1985). At the same time, the length scale of the eddies responsible for these processes is much larger than that acting on aircraft wakes. Arguments from similarity theory suggest that horizontal eddy coefficients should be about as much as factor of 10^4 smaller for scales less than 1 km (Overcamp and Fay, 1973). Vertical eddy coefficients in the lower stratosphere are of order $10^3 \text{ cm}^2 \text{s}^{-1}$, and are expected to be maintained by small-scale processes. There is virtually no information on the energy dissipation parameter ϵ .

We carried out calculations of the time-development of aircraft wakes for a period of two days, using the initial conditions and chemistry of Case 2 (ie., enhanced water, but no heterogeneous chemistry), and with the following assumptions for the entrainment:

- i. No entrainment
- ii. "Slow" Entrainment: $K_{ym} = 10^4 \text{ cm}^2 \text{s}^{-1}$, $\epsilon = 10^{-2} \text{ ergs/sec}$; $K_{zm} = 10^3 \text{ cm}^2 \text{s}^{-1}$.
- iii. "Fast" Entrainment: As above, but with $K_{ym} = 10^8 \text{ cm}^2 \text{s}^{-1}$. Our choices for the "fast" and "slow" entrainment are similar to those in the Gelinas and Walton formalism. Since heterogeneous chemistry on contrails is not expected to occur over several days, we did not include heterogeneous processes in this set of calculations, but they can be easily incorporated in future calculations.

b. Results

The calculated entrainment time constant t (Equation 7) is shown in Figure 4 as a function of time, for the assumptions of slow (4a) and fast (4b) entrainment. Time constants for entrainment in the "slow" case increase from about 1 day at the beginning of the wake period to about 4 days after the 2-day calculation. The initial values for the time constant are about 30 minutes in the "fast" entrainment case, closer to the assumptions in our previous set of calculations. However, given the faster increase in wake size in this case, the final values for the time constants after two days are similar to the "slow" case. It must be emphasized that this agreement is a coincidence due to our choice of parameters and integration times.

Our calculations obtain dilution factors of 3 for the "slow" entrainment calculation, and 20 for the "fast" entrainment calculation after two days. Given the initial concentrations adopted in Table 1, we see that significantly perturbed conditions could still exist two days after the passing of an aircraft, with our choice of dispersion parameters. This is further illustrated in Figures 5-8, which show the calculated time development of HNO_3 (Figure 5), NO_x (Figure 6), ozone (Figure 7) and water (Figure 8) for cases with no entrainment, and "slow" and "fast" entrainment.

The calculated HNO_3 and NO_x (Figures 5 and 6) are within percents of what would be calculated if only entrainment were acting on these species. The conclusion from the two-day calculation is therefore similar to the one over the first hour: in the absence of heterogeneous chemistry, there is little chemical conversion of NO_x to HNO_3 in the wake. Concentrations of NO_x are still enhanced relative to the background, even after two days in the fast-entrainment case.

The maximum calculated ozone reduction is slightly larger in this set of calculations (25%) than in the 1-hour results, since our entrainment time constants are slower. Such reductions

can be maintained for 1 day or longer if "slow" entrainment takes place. The ozone quickly recovers to background values in the "fast" entrainment case after two days. The "no entrainment" calculations show ozone still decreasing, albeit at a slower rate than during the first 100 seconds. The slowing down of ozone loss is due to the conversion of ozone-removing NO to other forms of NO_x , such as NO_2 and N_2O_5 .

Water concentrations are assumed to be initially about a factor of 70 higher than background. Figure 7 shows that enhancements of water of between factors of 5 and 20 over the background value (about 4 ppmv) could be still observed 2 days after the passage of the aircraft. The results in Figures 6 and 7 thus indicate that large perturbations in radiatively important species could be maintained for several days. These conditions could have important consequences for the net displacement and final deposition of aircraft effluents, as discussed in the next section.

RADIATIVE CALCULATIONS

We have adapted the radiative subroutines in our 2-D interactive model (Schneider *et al.*, 1989) in order to assess the differential cooling of aircraft wakes due perturbations in radiatively active species. This code includes a parameterization of solar heating from absorption in the UV and near infrared by ozone and water, as well as cooling for CO_2 , O_3 and H_2O in the infrared. Parameterizations for overlapping bands are described in Wang and Ryan (1983). Calculated total heating rates with this code compare favorably with other calculations (Dopplick, 1970), although it is difficult to directly compare the contributions by different bands of species due to differences in adopted water and ozone profiles, and the apportioning of heating and cooling to different species in the spectral regions where bands overlap.

Our calculations take the background atmospheric densities and UV and IR fluxes from our interactive 2-D model, since we expect that the aircraft wake will not alter the large-scale radiation field in the atmosphere. We assume that the wake temperature is the same as that of the background atmosphere. This may not be the case if dispersion of initial plume heat has not achieved completion; as a matter of fact, a relationship between the wake water vapor concentration and temperature can be obtained (Miake-Lye *et al.*, 1991), indicating that temperatures at the beginning of the wake regime could be a few degrees higher than that of the surrounding atmosphere. We will include in our future work assessment of the effect of temperature differences on calculated cooling rates.

We have carried out calculations of the differential cooling rates at altitudes between 13 and 25 km, and for all latitudes and seasons. Modeling of the jet and wake regime and estimates of dilution factors indicate that concentrations of water could be as high as 300 ppmv (a factor of 70 enhancement over the background) at the beginning of the wake regime, in the absence of condensation in contrails (See Table 1 and discussion above). The results of our photochemical calculations indicate ozone reductions ranging from 15% to 25% (Figures 3 and 7). Based on this results, we have assumed for simplicity in our calculations water enhancements ranging from factors of 70 to 10, and ozone reductions of 20% over background values (2.9 ppmv). Although our code also includes the effects of CO_2 , preliminary estimates indicate that the impact of its enhancement would be minor compared to those of water and ozone.

Another parameter of importance is the thickness of the wake. Our original code was adapted for incorporation into our 2-D model, with a vertical altitude resolution of about 3.5 km. Calculations assuming an enhancement of 70 in water over 3.5 km indicate that some water bands saturate, and

a "cooling to space" approximation is not appropriate. Since such vertical extents do not seem realistic for a single wake (although such vertical extent could be typical of a flight corridor), we further modified our code to allow for insertion of a wake of arbitrary vertical thickness at a given level.

Our first set of calculations assumed a wake of 3.5 km thickness, with an enhancement in water by a factor of 70 and 20% reduction in ozone. This case is not considered to be realistic, and represents an upper bound to the expected enhancement in water over a flight corridor. Results for differential cooling rates (K/day) are presented in Figures 9-12 for days 30 (Figure 9), 120 (Figure 10), 210 (Figure 11), and 300 (Figure 12). As discussed above, values for the vertical velocities can be obtained by dividing the numbers in Figures 9-12 by a factor of 10 (Equation 7). Vertical velocities as large as 0.4-0.5 km/day could be obtained for wakes deposited at altitudes above 22 km. Even at lower altitudes, vertical velocities of 0.2 km/day are obtained at mid-latitudes.

Calculations in Figures 13-16 are carried out for the same days and the same water enhancement as in the previous set, but assuming a vertical thickness of 500 m for the wake. Comparison of these two sets of calculations illustrates the effect of water band saturation. These effects are less pronounced for a wake of only 500 m thickness, and thus the calculated cooling rates (and vertical velocities) are actually larger. Vertical velocities close to 1 km/day are obtained at altitudes above 22 km, with about 0.5 km/day being calculated at lower altitudes.

The gas-phase concentrations of water assumed in the above calculations may be difficult to maintain without any condensation (see e.g., Miake-Lye *et al.*, 1991). We have thus carried out a third set of calculations, assuming only a factor of 10 enhancement in water. Results are shown in Figures 17-20. Vertical velocities ranging from 0.2 to 0.3 km/day are obtained in this case. We note that, even for a 500 m wake, the IR cooling rates do not scale linearly with water concentration, suggesting that saturation effects are still operant over this range. Work is in progress to further explore this issue.

The results presented in Figures 9-20, when combined with the time-development of water in Figure 8, indicate that the aircraft wake could sink 1-2 km during the first two days. These results, however, depend on several processes and parameters which are at present not well quantified. These include:

- i. Formation and lifetime of contrails, as well as possible removal of water by contrail subsidence.
- ii. Time constants for turbulent dispersion of the wake.
- iii. Other processes contributing to wake dispersion and deformation. In particular, the impact of wind shear in reducing the smallest dimensions of the wake to a size when molecular diffusion becomes important should be considered (Prather and Jaffee, 1990).

DISCUSSION AND CONCLUSIONS

We have developed a Langrangian box model to study time development of trace species in the wake regime of an aircraft plume. This model has been used in preliminary calculations in order to assess the amount of conversion of NO_x to HNO_3 . Our calculations corroborate the CIAP results of the mid-70's (Gelinis and Walton, 1974; Hoshizaki *et al.*, 1975) i.e., that

there is very little conversion of NO_x to HNO_3 if only gas-phase chemistry is assumed to occur. Substantial conversion could occur, however, if heterogeneous chemistry takes place on contrails which could provide large enhancement in available surfaces for heterogeneous reactions. In particular, heterogeneous conversion of NO_2 to NO_3 could accelerate the NO_x to HNO_3 conversion by heterogeneous reactions. Heterogeneous chemistry, particularly reactions (2) and (4), provide an additional source of HO_x and lead to enhanced concentrations of OH in the wake.

We stress that these calculations presented here are of an illustrative nature. The duration of heterogeneous chemistry has been exaggerated, since we do not expect contrails to persist for one hour. There are also varying degrees of uncertainty in the rates of the heterogeneous reactions (2) - (4), depending on the composition of the reacting surface. The heterogeneous conversion of NO_2 to HNO_3 has not been experimentally established.

We have also extended our calculations to a time-period of two days, and investigated the sensitivity of our results to different assumptions about scale-dependent dispersion. Our calculations indicate that a chemically-perturbed environment could persist for two days after passage of the aircraft. In particular, concentrations of radiatively important species such as ozone and water could be reduced by about 20% and enhanced by factors of 4-70 respectively during this period of time.

The above results motivated an examination of the radiative balance in aircraft wakes. Enhancements in water and reductions in ozone yield differential cooling rates relative to the background which could be as large as 10 K/day. Calculated downward vertical velocities range from 0.2 to 1 km/day, depending on the altitude of wake deposition and the assumed water concentration. The net vertical displacement of the wake will be a sensitive function of the rate of dispersion of the wake.

We stress that the implications of both our photochemical and radiative results depend crucially on the adopted rates of dispersion. Information about this parameter is at present practically non-existent. Furthermore, other processes not directly included in this formation could be equally important. Prather and Jaffee (1990) examined the dispersion of chemically-perturbed polar air masses due to random shear in a turbulent field. This model actually predicts a decrease with time in the smallest dimension of the air mass, leading to an elongated "ribbon" which probably wraps around itself. When the smallest dimension of this ribbon reaches values of tens of meters, molecular diffusion becomes important, and the perturbed air mass mixes with the background in a matter of hours.

The above picture presents an alternative and probably more realistic view of wake dispersion. The "volume" of the wake corresponding to equation (1) could be considered to be that containing all of the "ribbon" wrapped around itself. At the same time, this model allows for patchiness inside the wake, and thus dispenses with the assumption of a Gaussian profile. This wake patchiness could presumably alter the photochemical calculations. Modeling of this kind of process requires a different approach from the one utilized in this and previous studies, and could lead to faster time constants than assumed here. Still, it must be noted that the rate of random strain by a turbulent stratospheric wind field is still an unknown parameter; estimated time constants range from 1 - 10 days (Prather and Jaffee, 1990).

Our calculations point to areas which deserve further study. These include:

- a. Are contrails formed in the wake regime, and what is the expected lifetime?
- b. Do the enhanced concentrations of HNO_3 increase the probability of forming nitric acid tri-hydrate contrails?
- c. If contrails are formed, how big are the particles, and could their subsidence contribute to a redistribution of HNO_3 and water?
- d. What are the entrainment rates in the lower stratosphere, and how would they compete with heterogeneous chemistry and contrail formation?
- e. What are the roles of random strain and molecular diffusion in the final mixing of aircraft wakes, and what are the time constants for these processes?

REFERENCES

Dopplick, T. G. (1970) Global radiative heating of the Earth's atmosphere. Planetary Circulation Project Report 24. Department of Meteorology, MIT, Cambridge, MA.

Gelinas, R.J., and J.J. Walton (1974) Dynamic-kinetic evolution of a single plume of interacting species. *J. Atmos. Sci.*, 31, 1807.

Hoshizaki, H., L.B. Anderson, R.J. Conti, N. Farlow, J.W. Meyer, T. Overcamp, K.O. Redler, and V. Watson (1975) Aircraft wake microscale phenomena. Chapter 2 in CIAP Monograph 3, Department of Transportation, Washington, DC, DOT-TST-75- 53.

Ko, M. K. W., K. K. Tung, D. K. Weisenstein, and N. D. Sze (1985) A zonal mean model of stratospheric tracer transport in isentropic coordinates: Numerical simulations for nitrous oxide and nitric acid. *J. Geophys. Res.*, 90, 2313.

Lee, J.H. and I.N. Tang (1988) Accommodation coefficient of gaseous NO_2 on water surfaces. *Atmos. Environ.* 22, 1147-1151.

Leu, M.-T. (1988a) Laboratory studies of sticking coefficients and heterogeneous reactions important in the Antarctic stratosphere. *Geophys. Res. Lett.*, 15, 17.

Leu, M.-T. (1988b) Heterogeneous reactions of N_2O with H_2O and HCl on ice surfaces: Implications for Antarctic ozone depletion. *Geophys. Res. Lett.*, 15, 851.

McElroy, M.B., R.J. Salawitch, S.C. Wofsy, and J.A. Logan (1986) Antarctic ozone: Reductions due to synergistic interactions of chlorine and bromine. *Nature*, 321, 759.

Miake-Lye, R.C., M. Martinez-Sanchez, R.C. Brown and C.E. Kolb (1992) Plume and wake dynamics, mixing, and chemistry behind an HSCT aircraft. *J. Aircraft*, accepted for publication.

Molina, M.J., T.L. Tso, L.T. Molina and F.C.Y. Wang (1987) Antarctic stratospheric chemistry of chlorine nitrate, hydrogen chloride and ice: Release of active chlorine. *Science*, 238, 1,253.

Mozurkewich, M. and J.G. Calvert (1988) Reaction probability of N_2O_5 on aqueous aerosols. *J. Geophys. Res.*, 93, 15,889.

Overcamp, T. J., and J. A. Fay (1973) Dispersion and subsidence of the exhaust of a supersonic transport in the stratosphere. *J. Aircraft*, 10, 720-728.

Prather, M.J., and A.H. Jaffe (1990) Global impact of the antarctic ozone hole: Chemical propagation. *J. Geophys. Res.*, 95, 3473- 3492.

Schneider, H. R., Malcolm K. W. Ko, N. D. Sze, G.-Y. Shi, and W.-C. Wang (1989) An evaluation of the role of eddy diffusion in stratospheric interactive two-dimensional models. *J. Atm. Sci.*, 46, 2079-2093.

Rodriguez, J.M. M.K.W. Ko and N.D. Sze (1988) Antarctic chlorine chemistry: Possible global implications. *Geophys. Res. Lett.*, 15, 257.

Rodriguez, J.M. , M.K.W. Ko, and N.D. Sze, S.D. Pierce, J.G. Anderson, D.W. Fahey, K. Kelly, C.B. Farmer, G.C. Toon, M.T. Coffey, L.E. Heidt, W.G. Mankin, K.R. Chan, W.L. Starr, J.F. Vedder, and M.P. McCormick (1989) Nitrogen and chlorine species in the spring Antarctic stratosphere: Comparison of models with Airborne Antarctic Ozone Experiment observations. *J. Geophys. Res.*, 94, 16,683.

Solomon, S., R.R. Garcia, F.S. Rowland, and D.J. Wuebbles (1986) On the depletion of antarctic ozone. *Nature*, 321, 755.

Tolbert, M.A., M.J. Rossi, R. Malhotra, and D.M. Golden (1987) Reaction of chlorine nitrate with hydrogen chloride and water at anarctic stratospheric temperatures. *Science*, 238, 1258.

Tolbert, M.A., M.J. Rossi and D.M. Golden (1988a) Heterogeneous chemistry related to Antarctic ozone depletion chemistry: Reactions of N_2O_5 with H_2O and HCl on ice surfaces. *Science*, 240, 1018.

Tolbert, M.A., M.J. Rossi and D.M. Golden (1988b) Heterogeneous interactions of chlorine nitrate, hydrogen chloride, and nitric acid with sulfuric acid surfaces at stratospheric temperatures. *Geophys. Res. Lett.*, 15, 847.

Van Doren, J.M., L.R. Watson, P. Davidovits, D.R. Worsnop, M.S. Zahniser and C.E. Kolb (1991) Uptake of N_2O_5 and HNO_3 by aqueous sulfuric acid droplets. *J. Physical Chem.* In press.

Wang, W.-C., and P. B. Ryan (1983) Overlapping effect of atmospheric H_2O , CO_2 and O_3 in the CO_2 radiative effect. *Tellus*, 35B, 81- 91.

Wofsy, S.C. (1978) Temporal and latitudinal variations of trace gases: A critical comparison between theory and experiment. *J. Geophys. Res.*, 83, 364-378.

Table 1: Adopted Initial Conditions

Species	Initial conditions (mixing ratio)	Background atm.
NO + NO ₂	4.48 x 10 ⁻⁷	1.55 x 10 ⁻⁹
HNO ₃	2.80 x 10 ⁻⁸	4.75 x 10 ⁻⁹
N ₂ O ₅	2.20 x 10 ⁻¹⁰	2.60 x 10 ⁻¹⁰
O ₃	2.91 x 10 ⁻⁶	2.91 x 10 ⁻⁶

Table 2: Cases Considered

Case	H ₂ O	Heterogeneous chemistry
1	4.3 ppmv (backgd.)	No
2	3×10^{-4}	No
3	3×10^{-4}	On sulfate aerosols with "Antarctic" rates
4	4.3 ppmv	On contrails - (1 μ particles; 10^3 cm ⁻³ ; "Antarctic" rates
5	4.3 ppmv	As in Case 4, with heterogeneous conversion of NO ₂ to NO ₃ on sulfate aerosols.
6	4.3 ppmv	As in Case 5, but conversion on contrails.

Table 3: Photochemical Repartitioning of Nitrogen Species (after 1 hour)

Case	<u>NO_x(chem.+ ent.)</u>	<u>HNO₃(chem.+ ent.)</u>
	<u>NO_x(ent.)</u>	<u>HNO₃(ent.)</u>
1	1.03	0.96
2	1.03	0.96
3	1.03	0.96
4	0.78	1.33
5	0.67	1.49
6	0.19	2.20

Table 4: Comparison of Trace Species in Wake to Background Concentrations (after 1 hour)

Case	<u>OH</u>	<u>HNO₃</u>	<u>NO_x</u>	<u>O₃</u>
	OH(bckgd.)	HNO ₃ (bckgd.)	NO _x (bckgd.)	O ₃ (bckgd.)
1	0.52	1.00	2.61	0.998
2	0.63	1.00	2.60	0.999
3	0.65	1.07	2.60	0.999
4	2.83	1.39	1.96	0.998
5	2.84	1.56	1.69	0.998
6	0.80	2.30	0.47	0.997

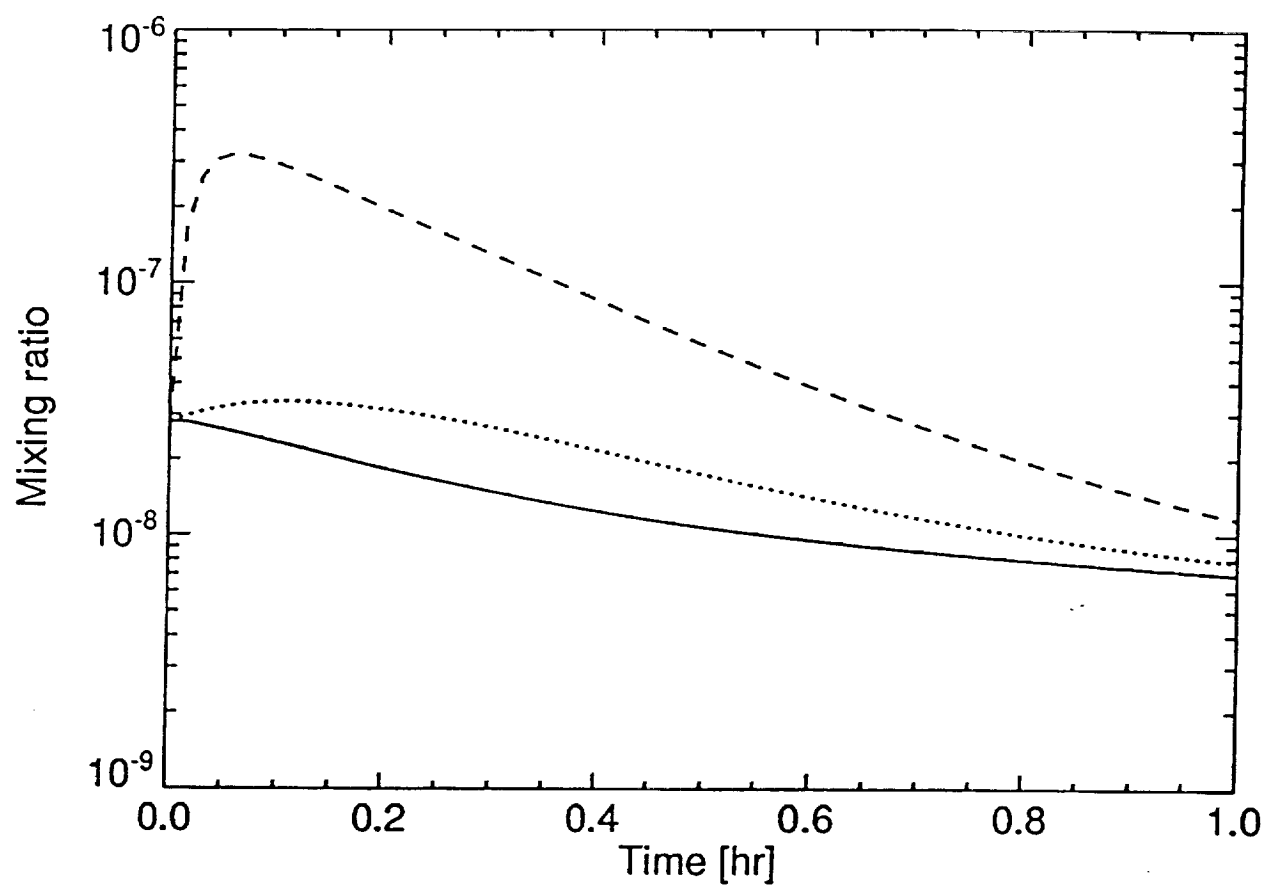


Figure 1: Calculated concentrations of HNO₃ during the first hour, for cases 4 (solid line), 5 (dotted line), and 6 (dashed line). See text for details

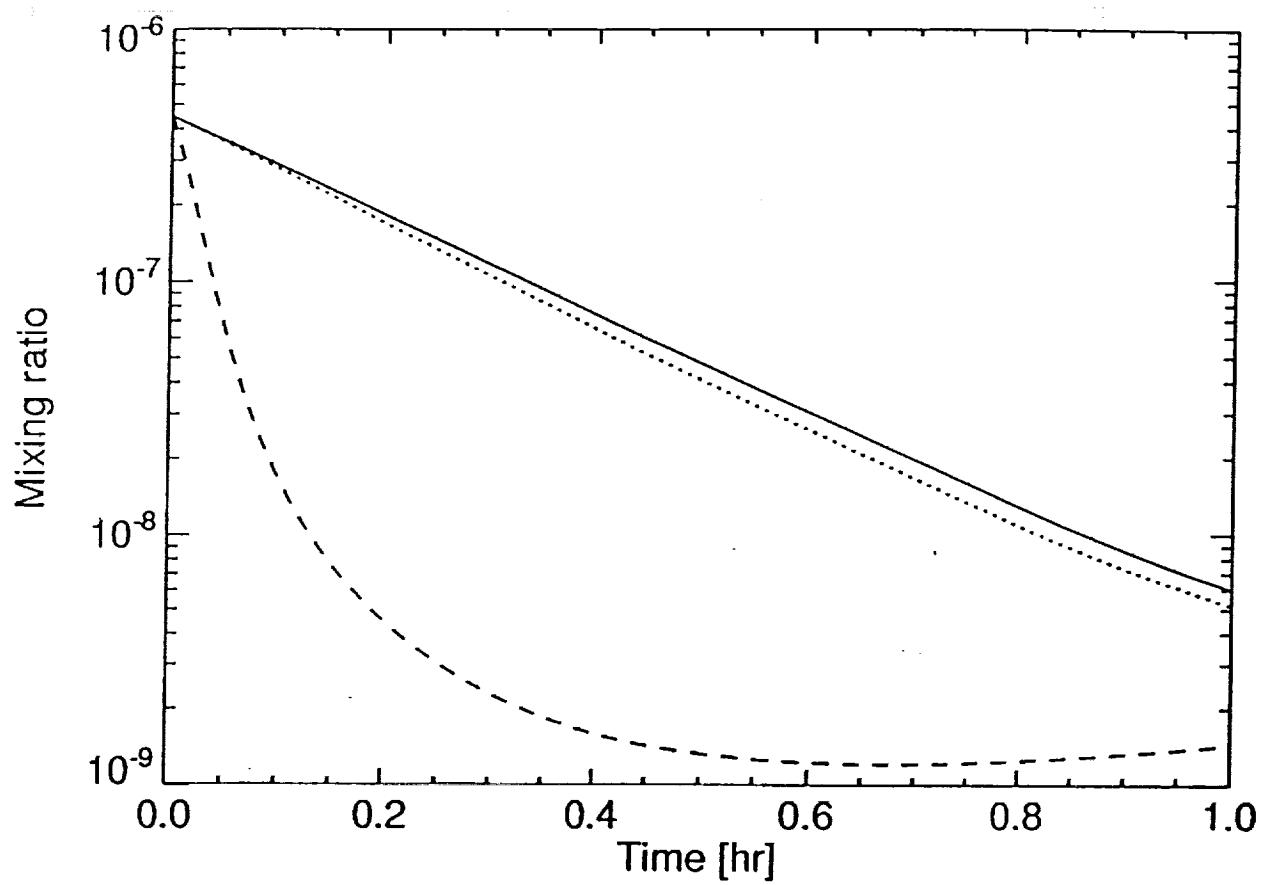


Figure 2: Same as Figure 1, except for NO_x .

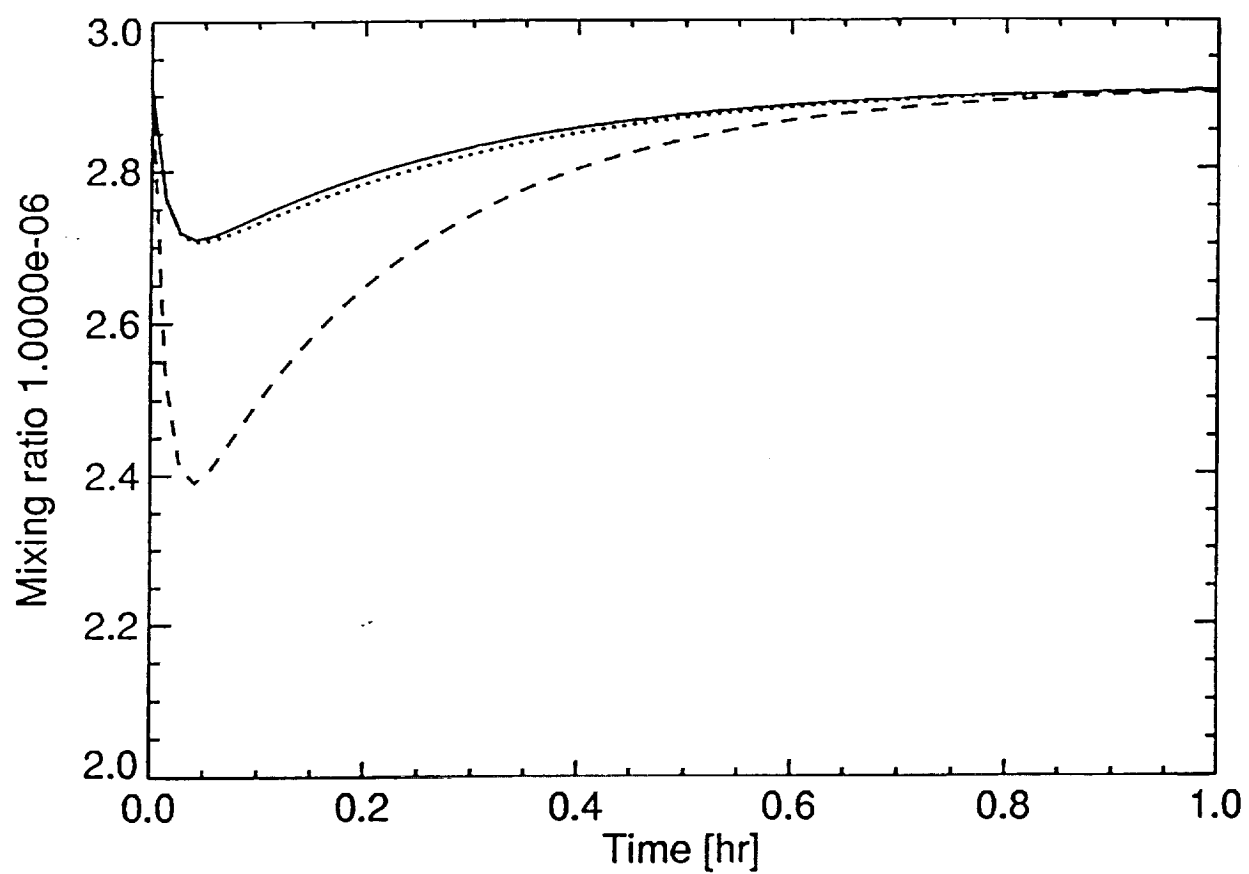
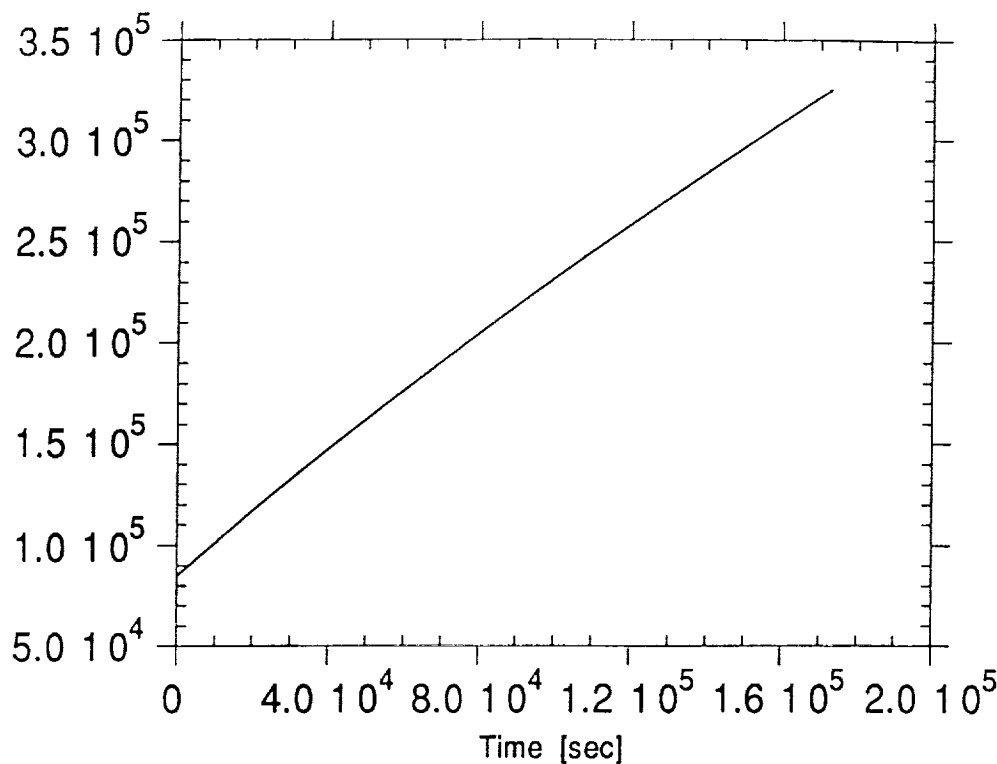
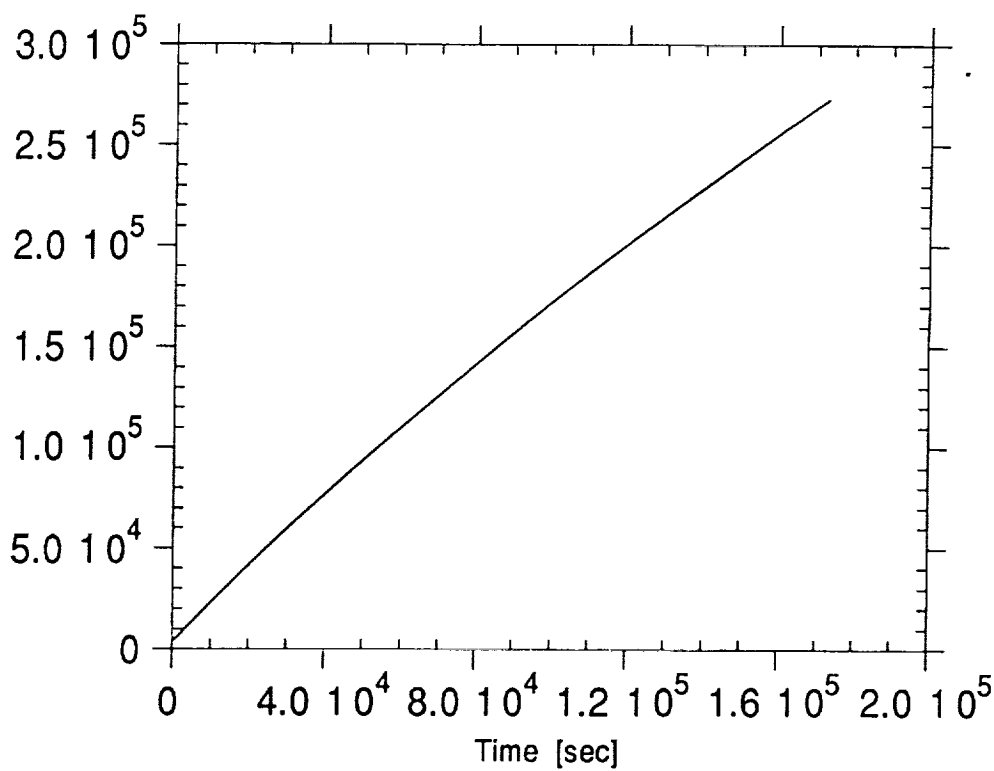


Figure 3: Same as Figure 1, except for ozone.



(a)



(b)

Figure 4. Calculated entrainment time constant τ (see equation 7) for the cases with scale-dependent diffusion as a function of time. Panel (a) shows the calculations for "slow" entrainment, while panel (b) denotes the calculated τ for "fast" entrainment. See text for details.

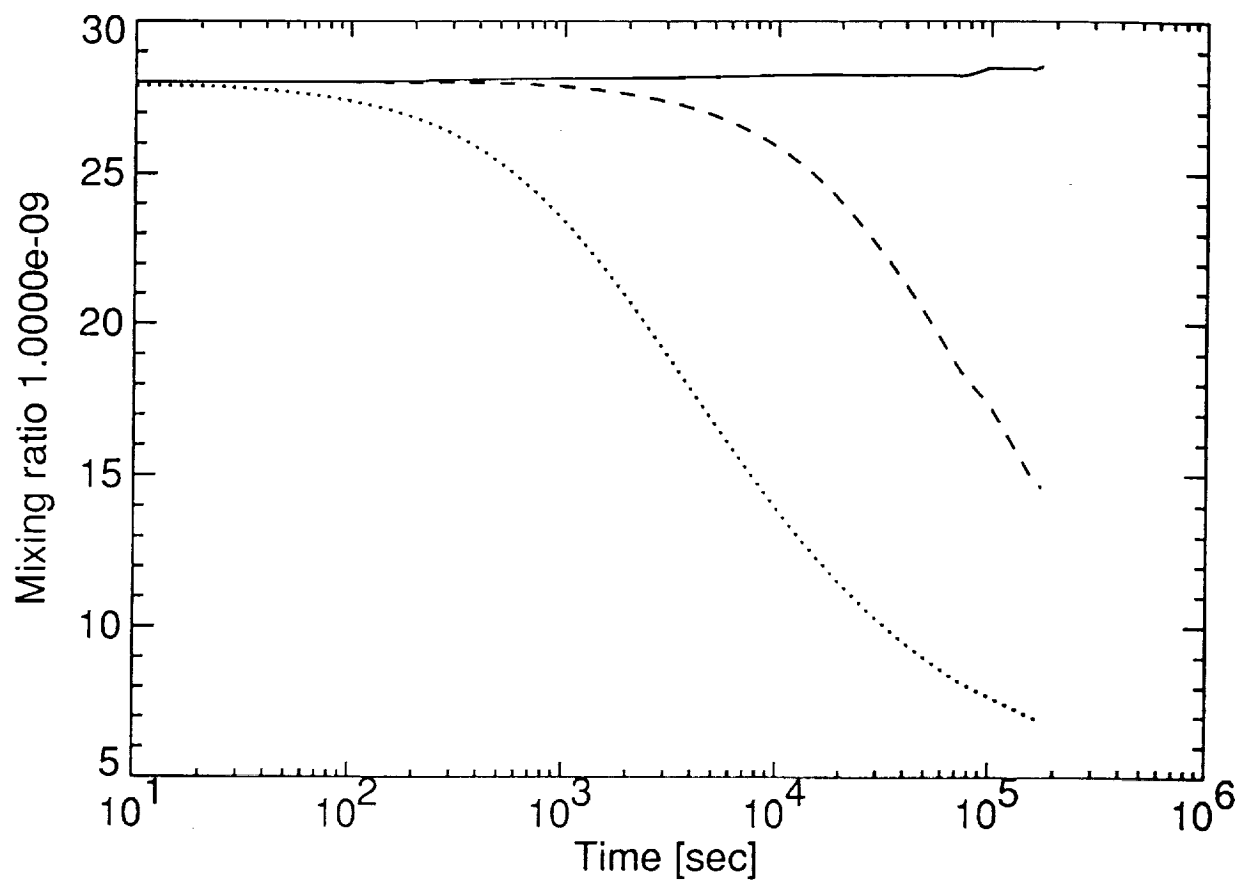


Figure 5. Calculated time development of nitric acid for the assumptions of case 2, except that a scale-dependent parameterization for entrainment is adopted. Results for no entrainment (solid line) and slow (dashed line) and fast (dotted line) scale-dependent dispersion are presented.

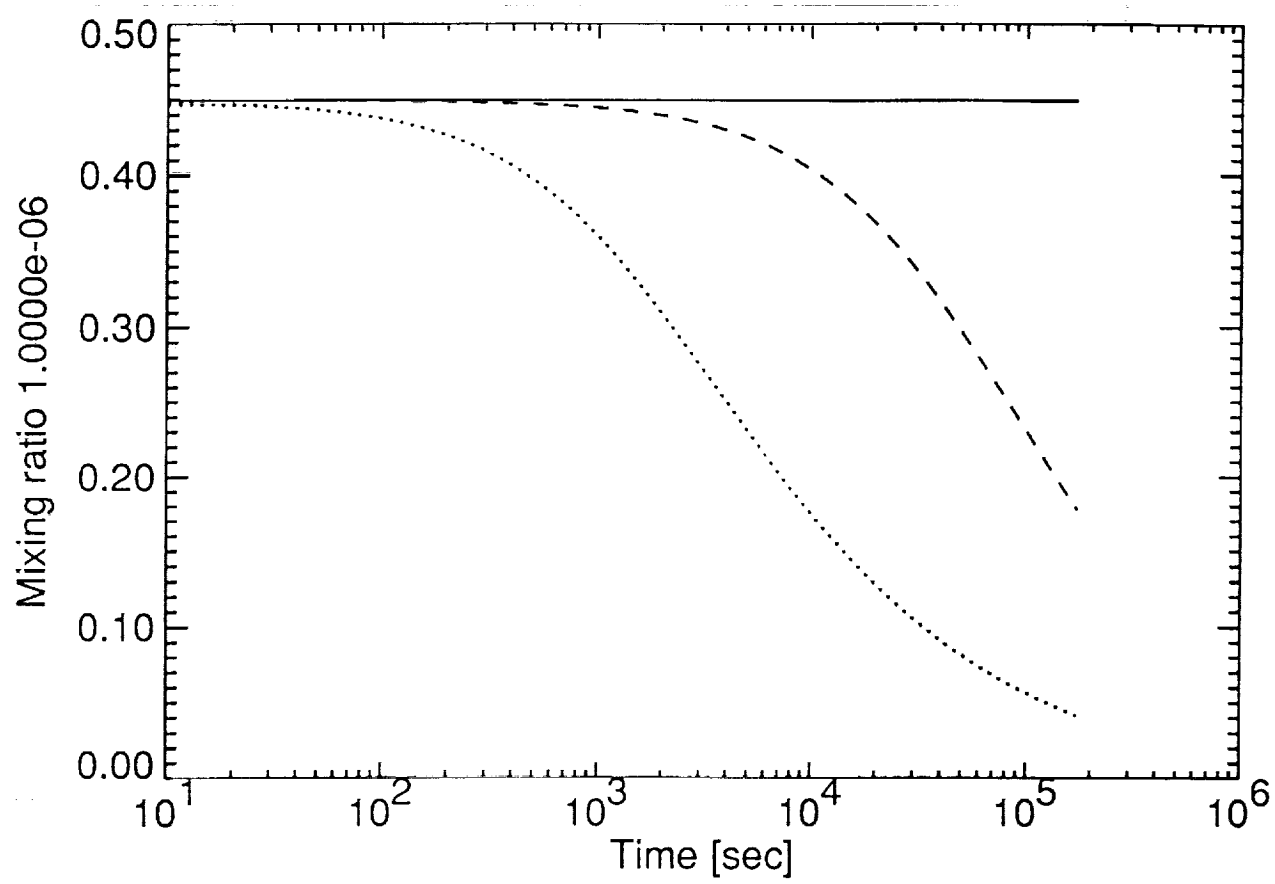


Figure 6. Same as Figure 5, except for calculated NOx.

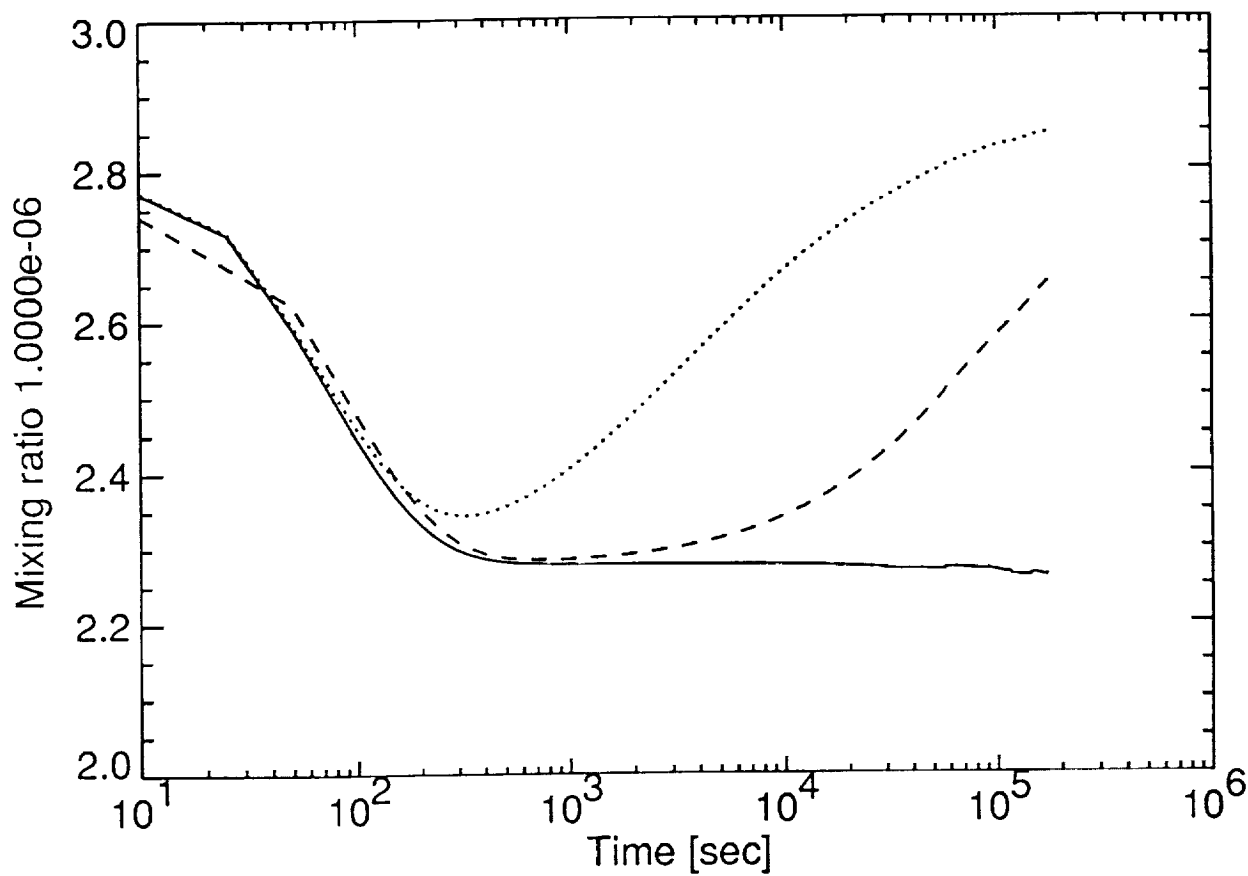


Figure 7. Same as Figure 5, except for calculated ozone.

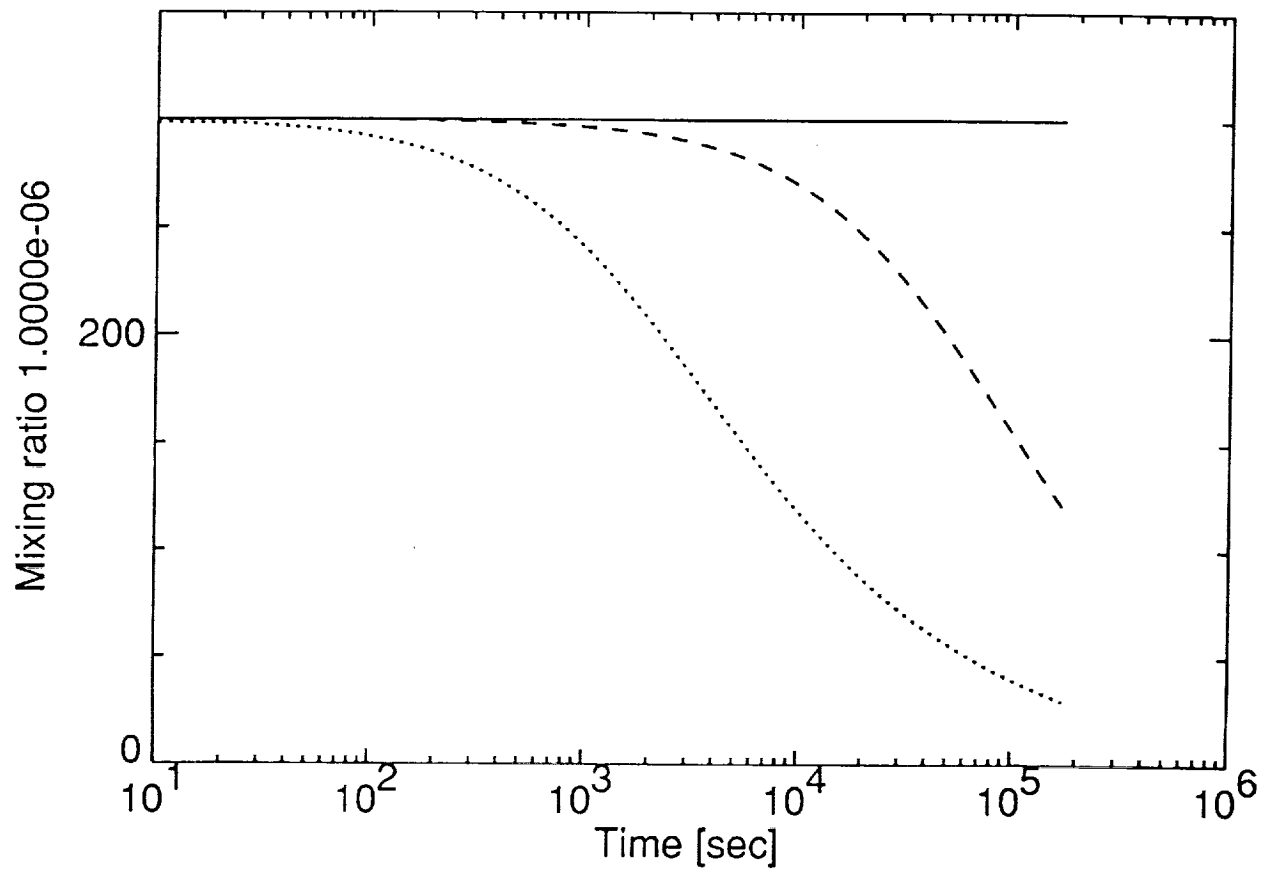


Figure 8. Same as Figure 5, except for calculated water.

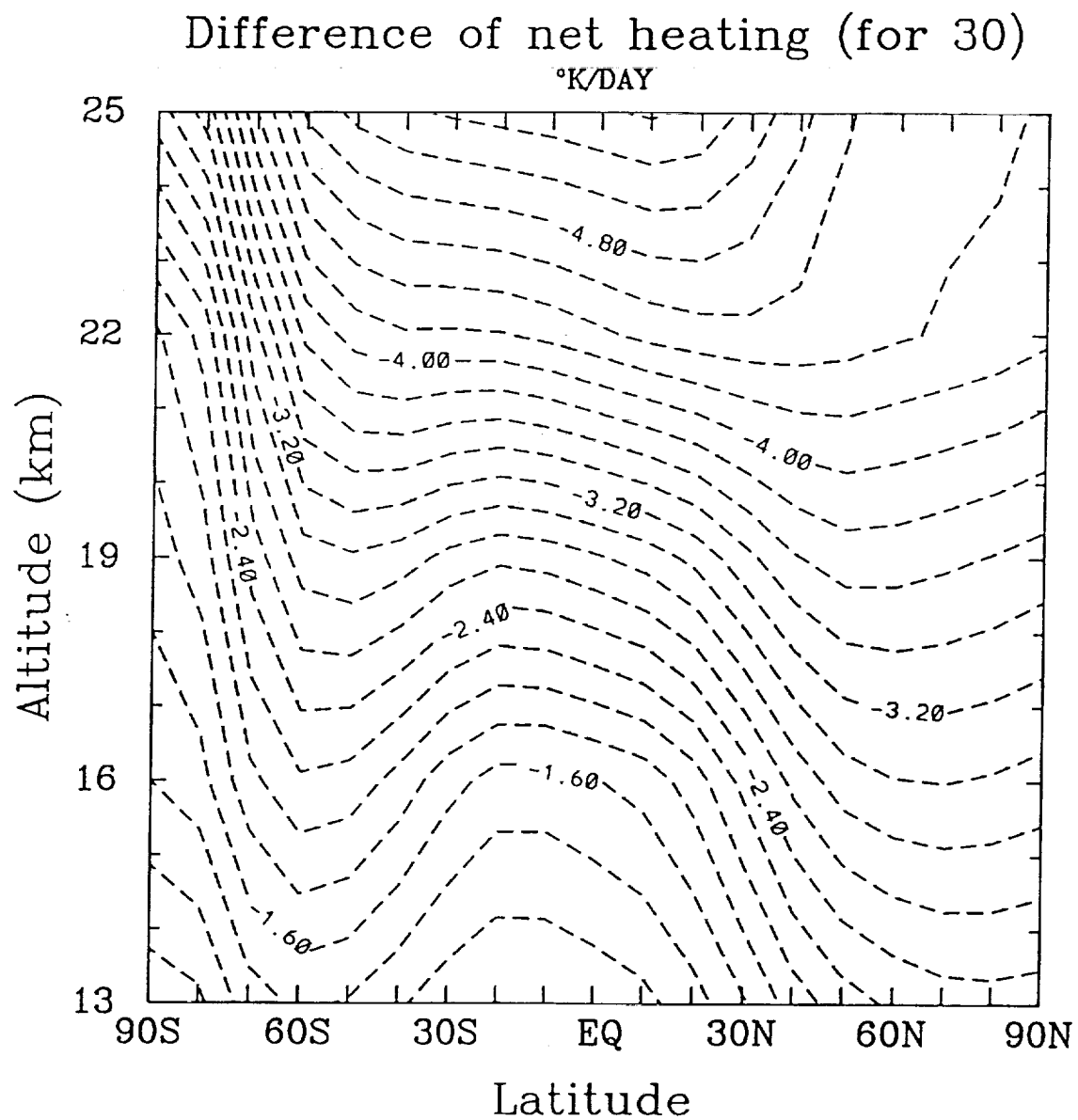
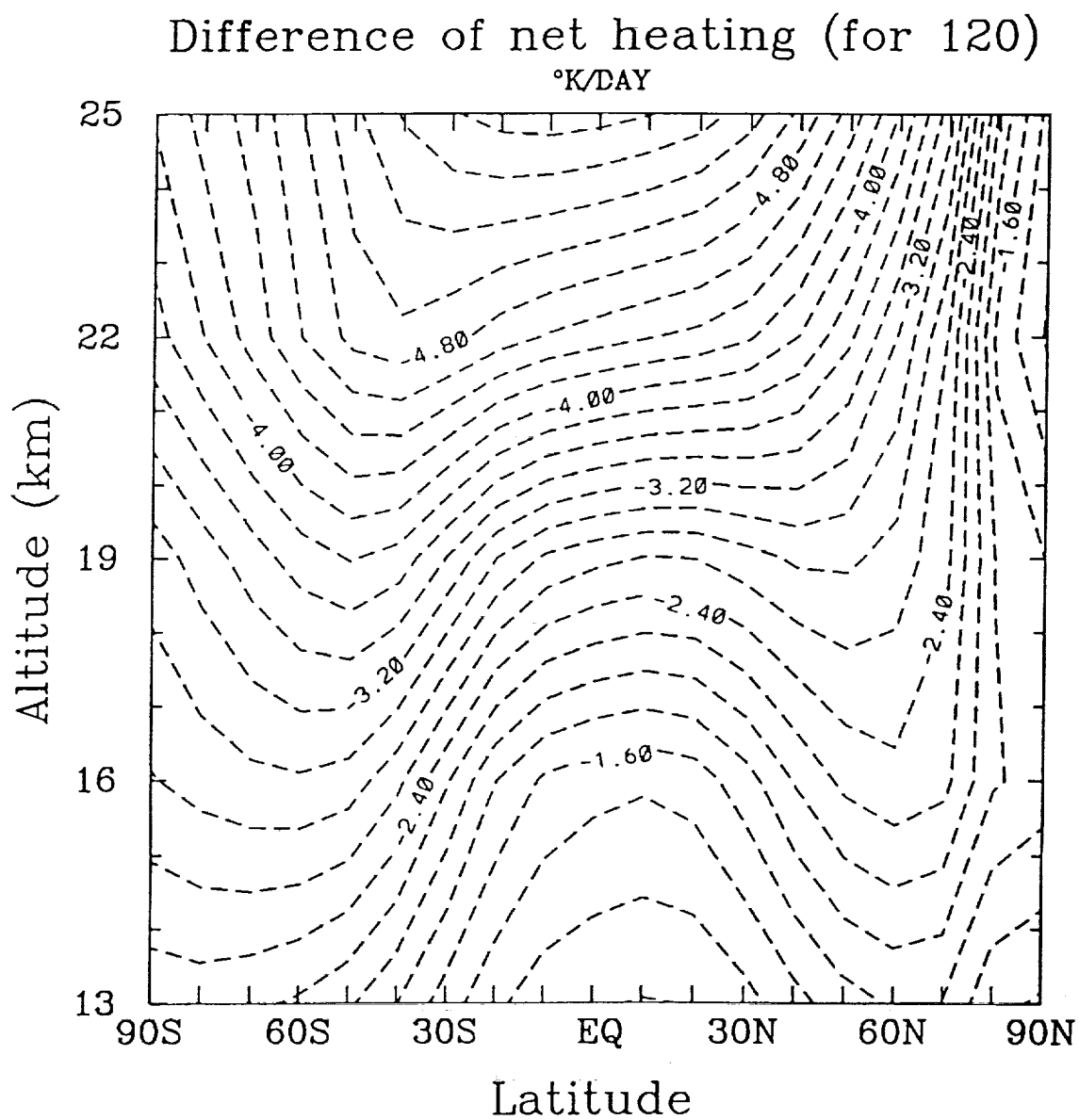
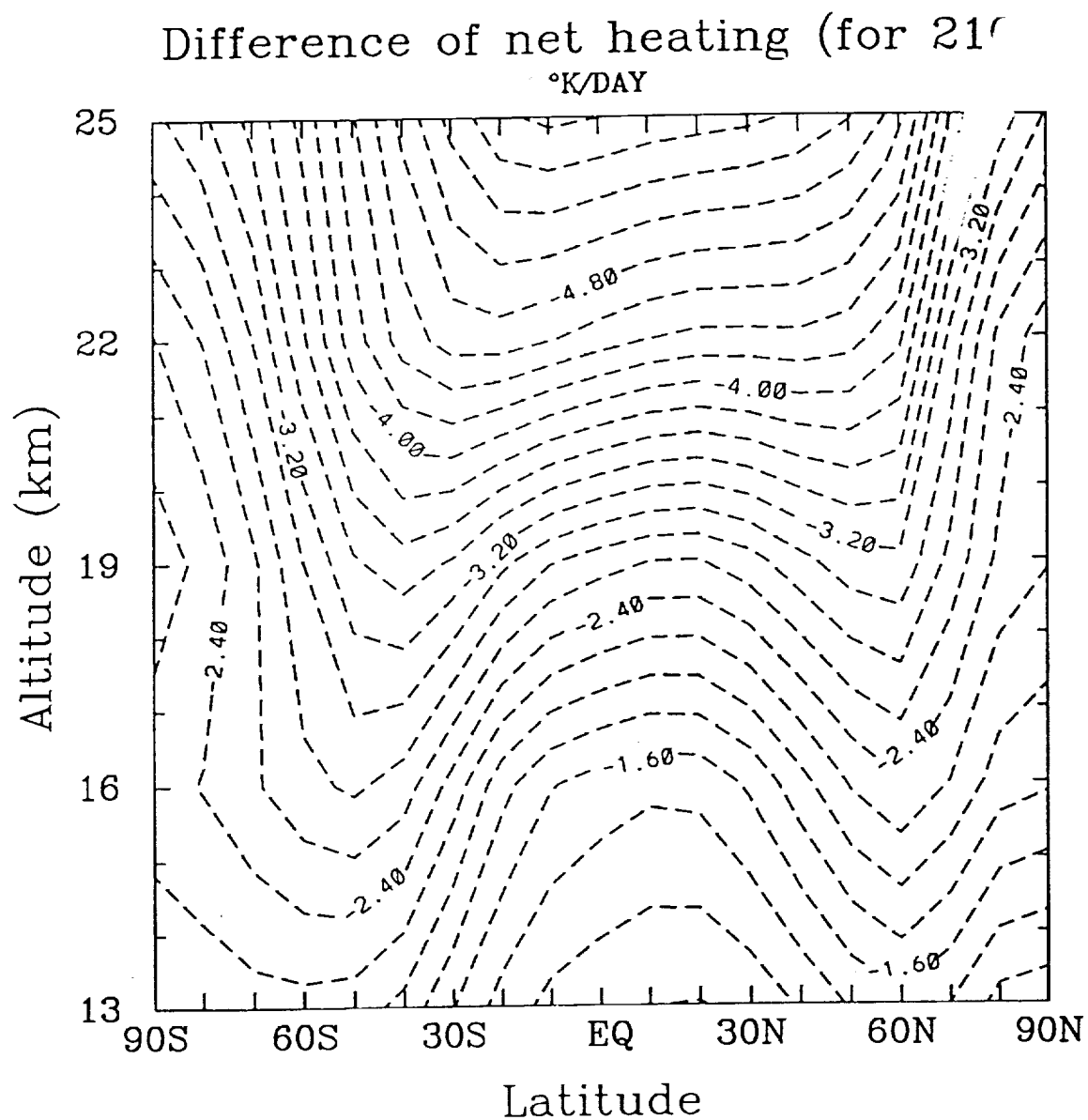


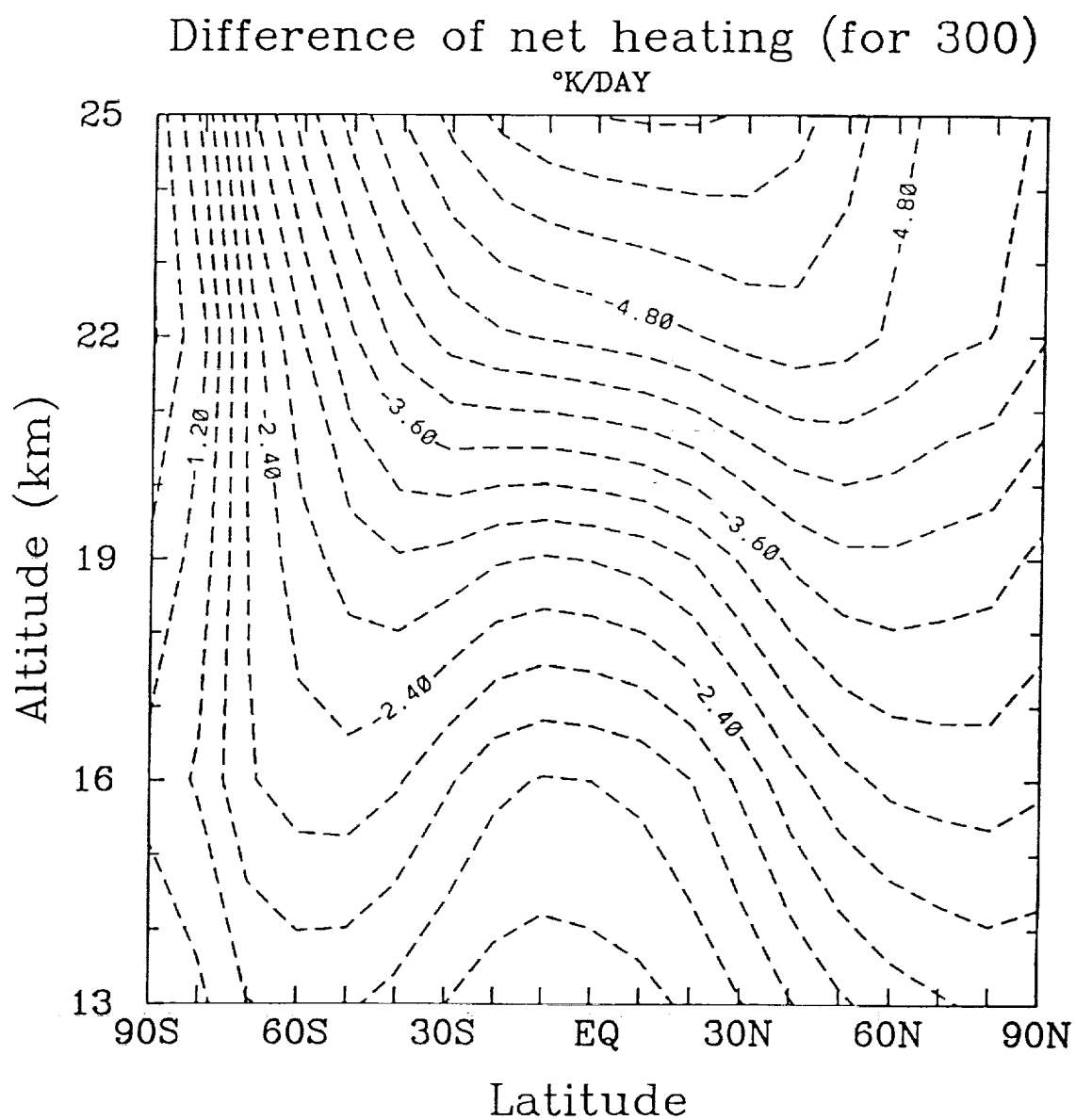
Figure 9. Differential heating rate ($^{\circ}\text{K}/\text{day}$) as a function of altitude and latitude, for day 30. We assume that the concentrations of water and ozone are respectively increased and decreased by factors of 70 and 0.8 over the background values. These increases are assumed to hold over the whole grid vertical width (3.5 km in our 2-D model).



Figures 10. Same as Figure 9, except for day 120.



Figures 11. Same as Figure 9, except for day 210.



Figures 12. Same as Figure 9, except for day 300.

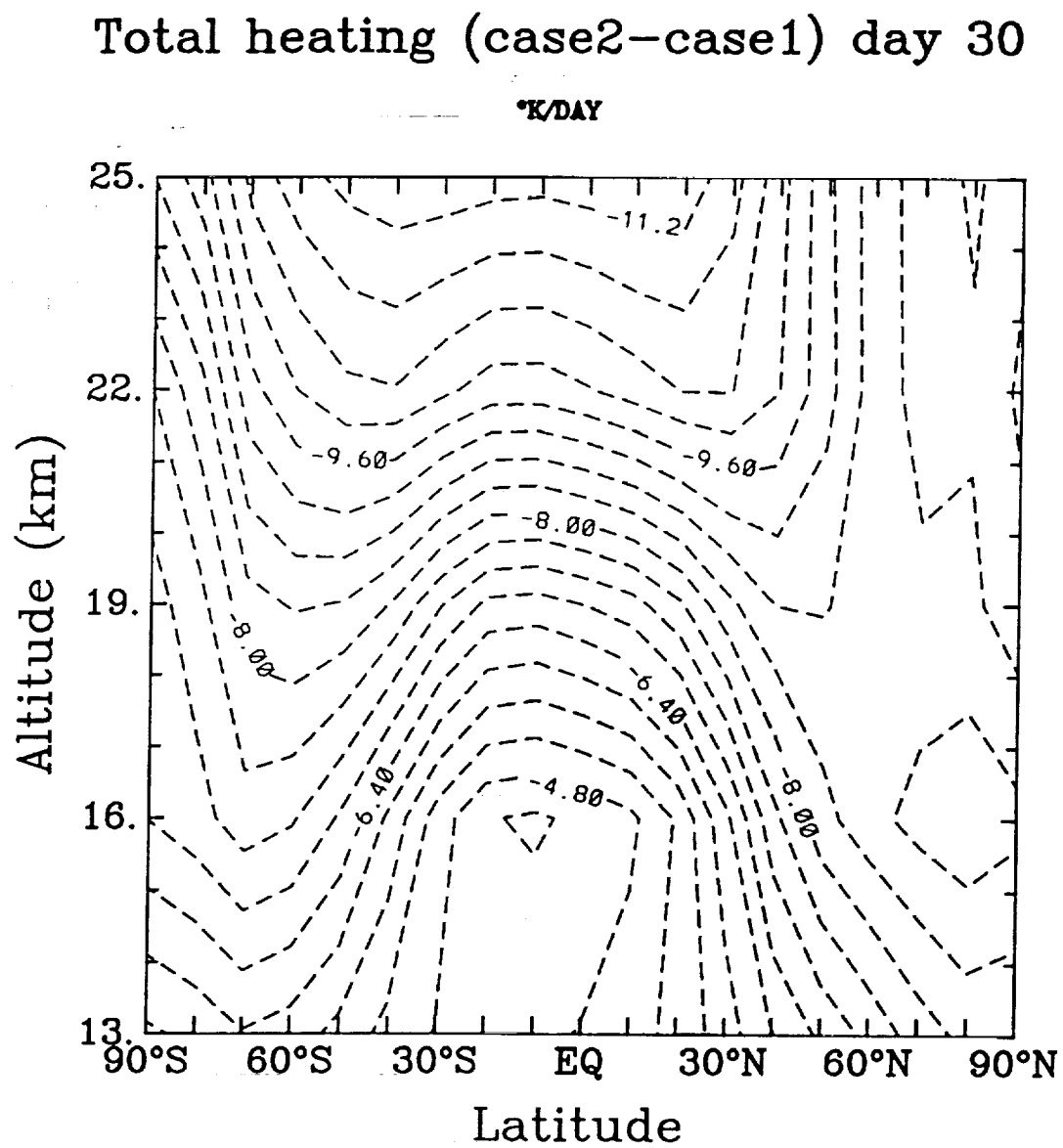


Figure 13. Same as Figure 9, except that the vertical thickness of the plume is taken to be only 500 m.

Total heating (case2-case1) day 120

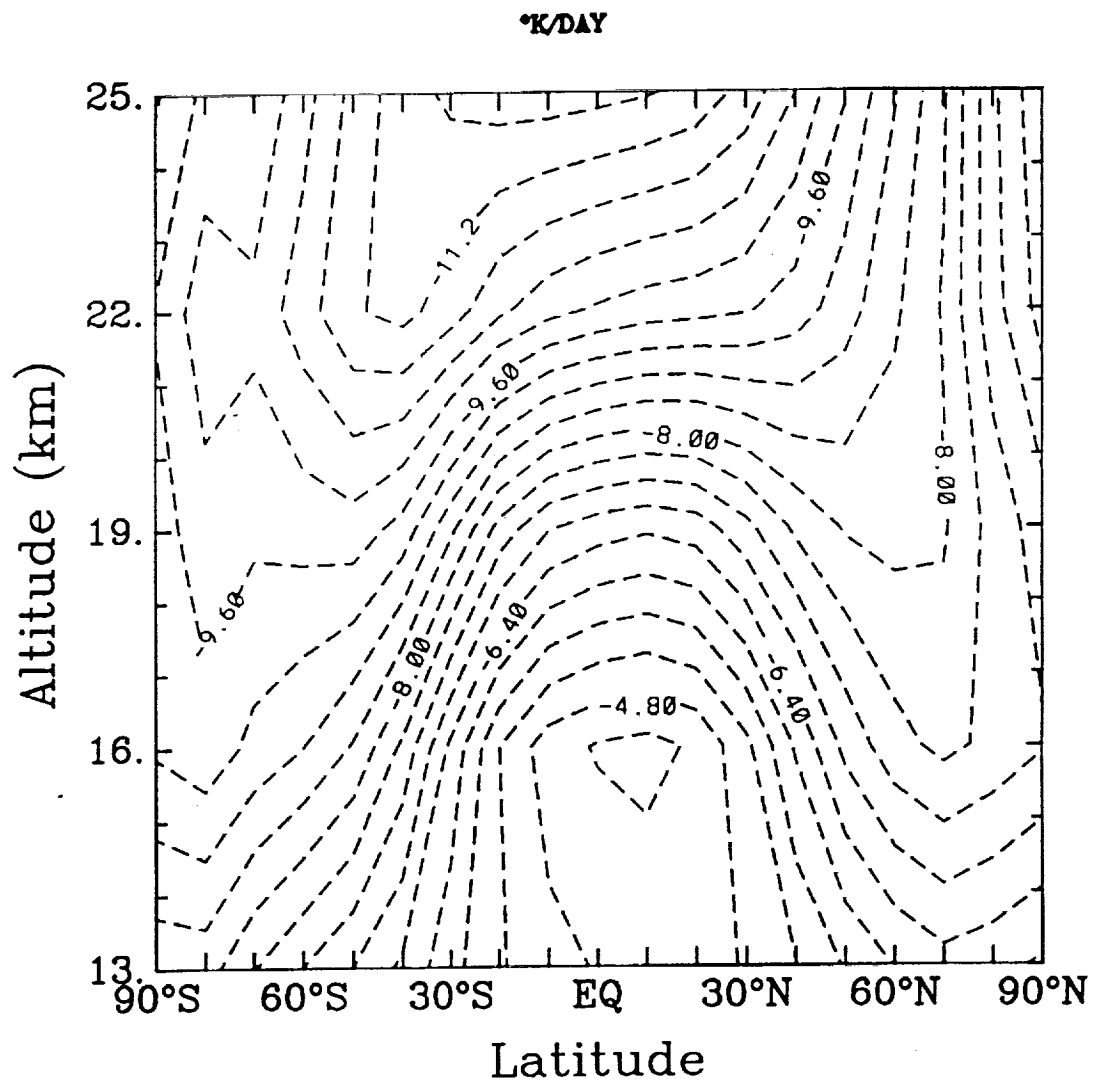


Figure 14. Same as Figure 13, except for day 120.

Total heating (case2-case1) day 210

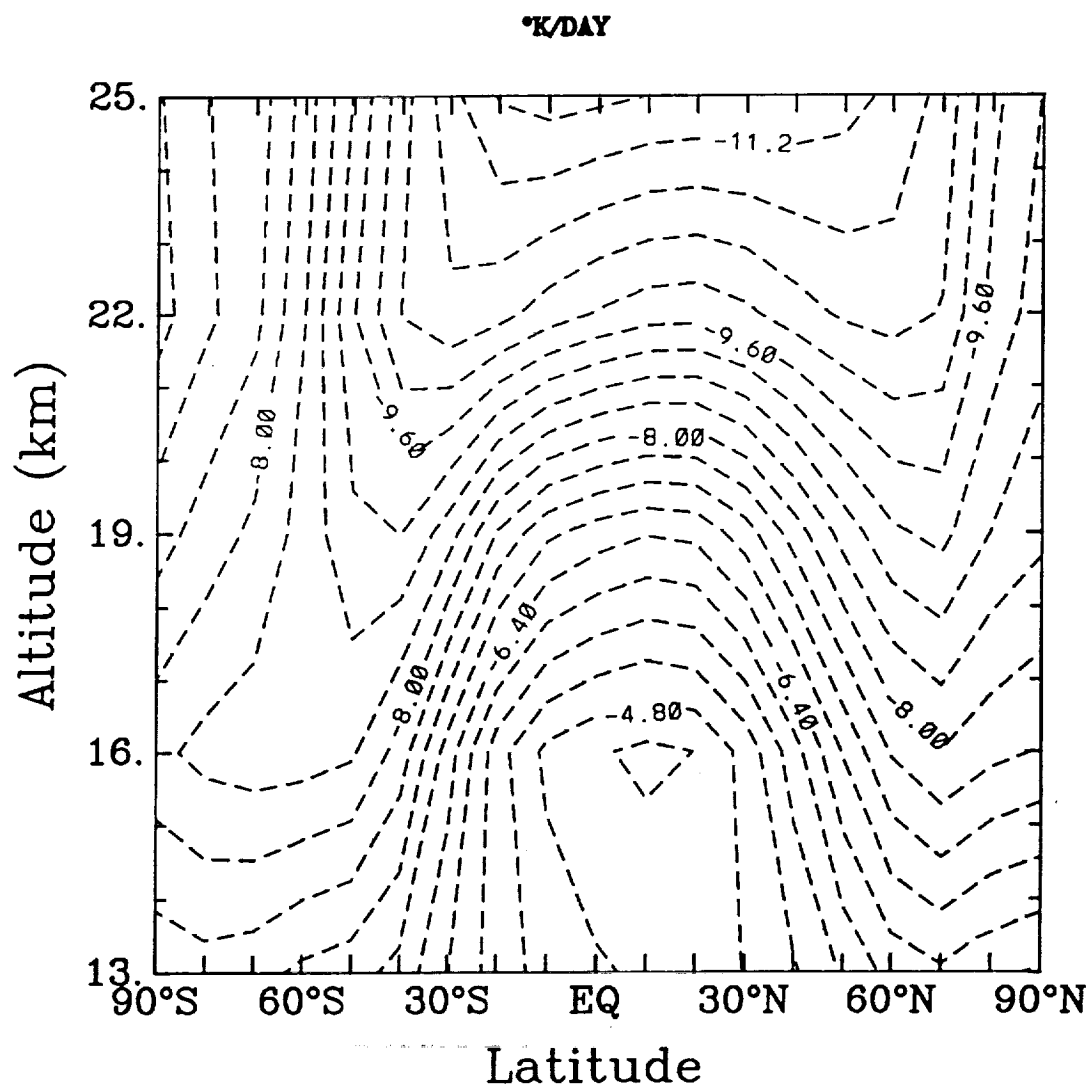


Figure 15. Same as Figure 13, except for day 210.

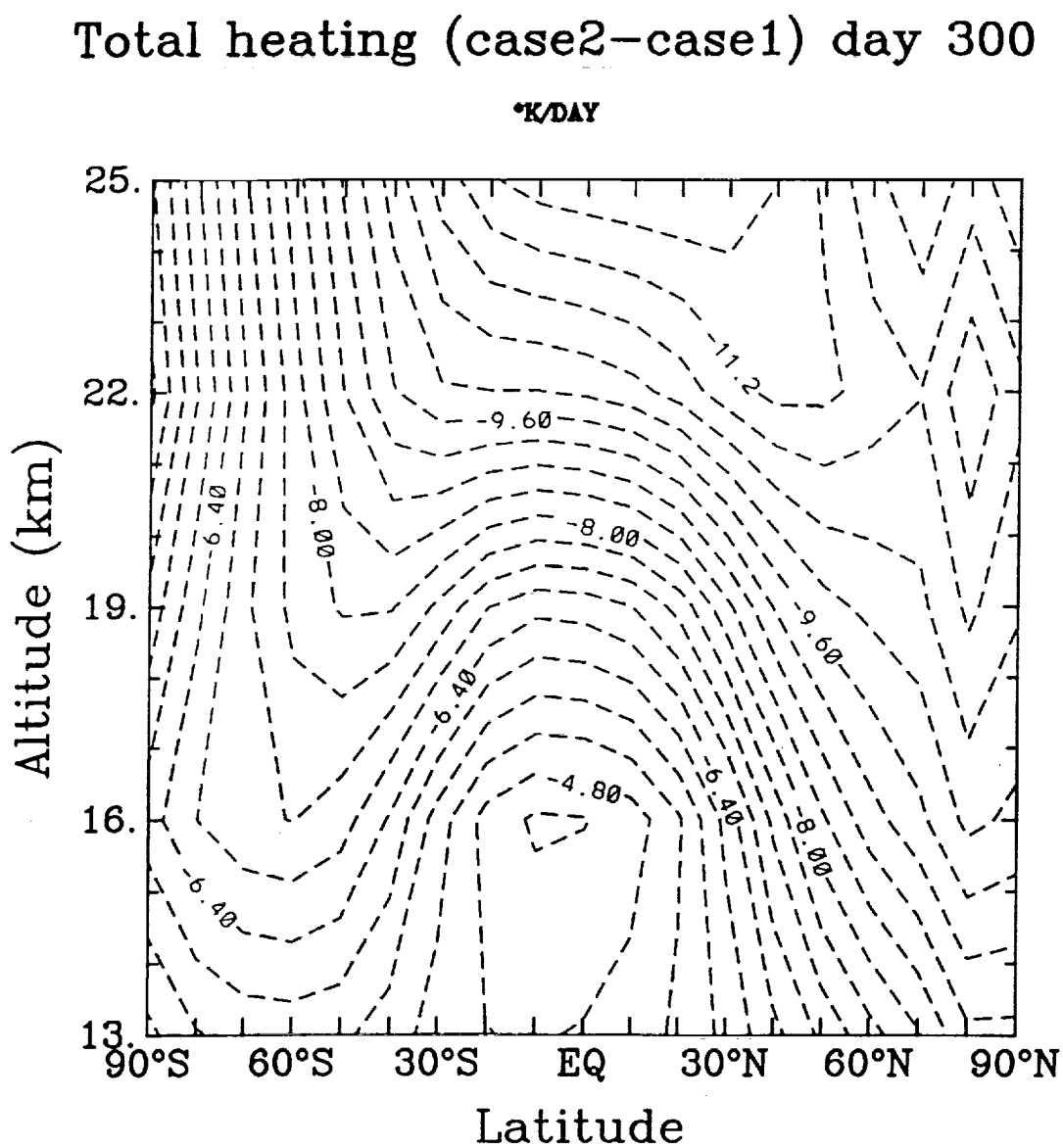


Figure 16. Same as Figure 13, except for day 300.

Total heating (case4–case1) day 30

°K/DAY

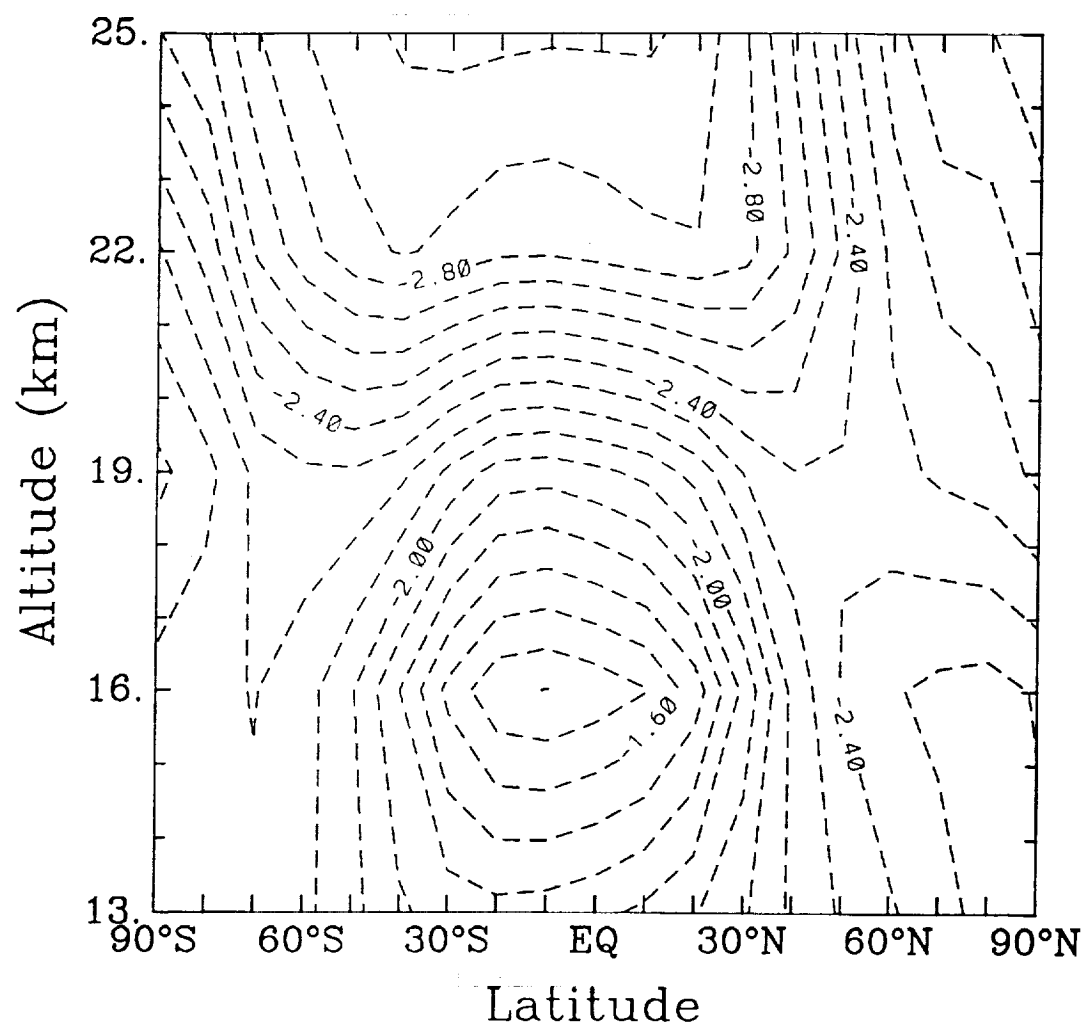


Figure 17. Same as Figure 13, except that the water is enhanced only by a factor of 10.

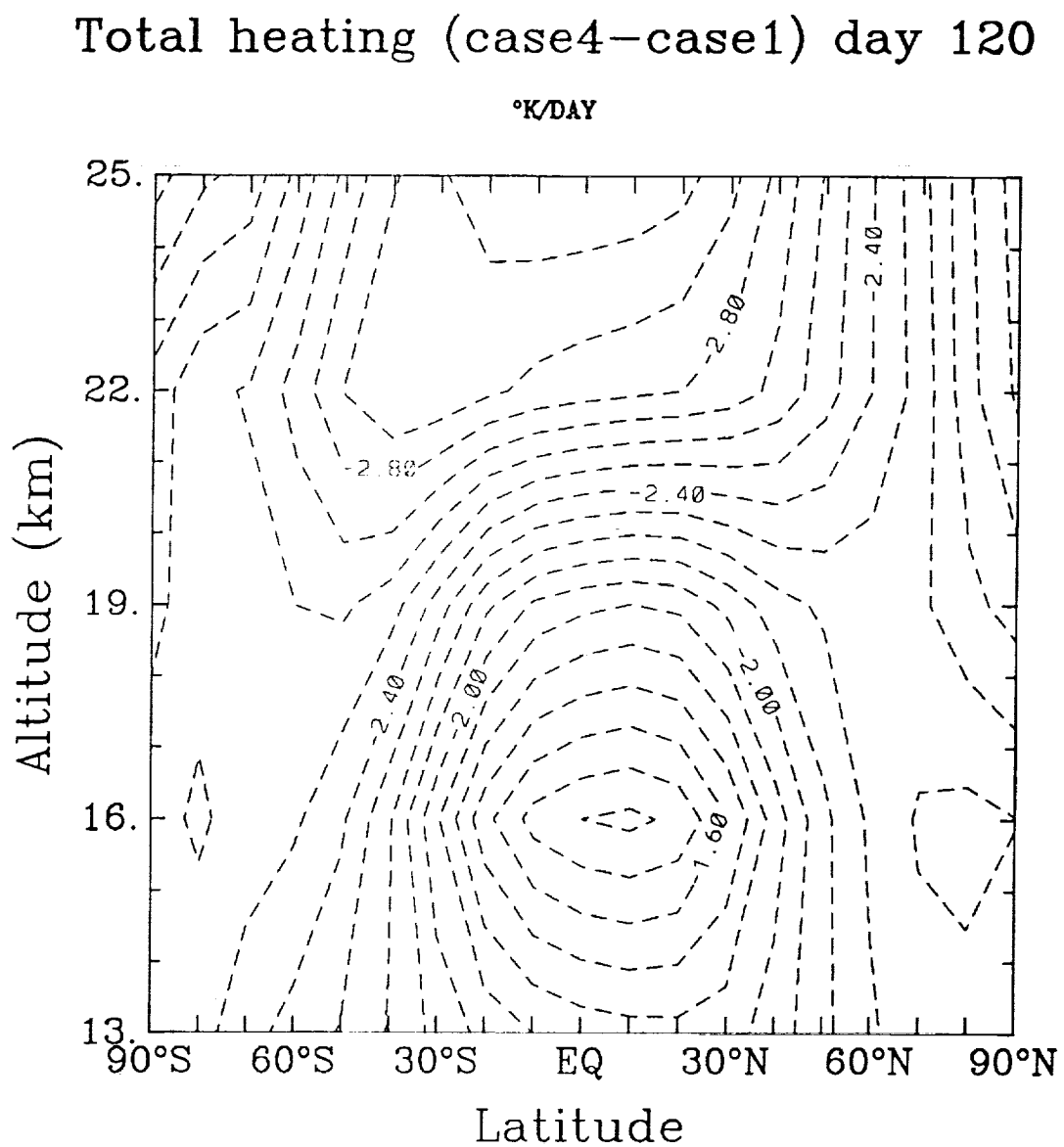


Figure 18. Same as Figure 17, except for day 120.

Total heating (case4-case1) day 210

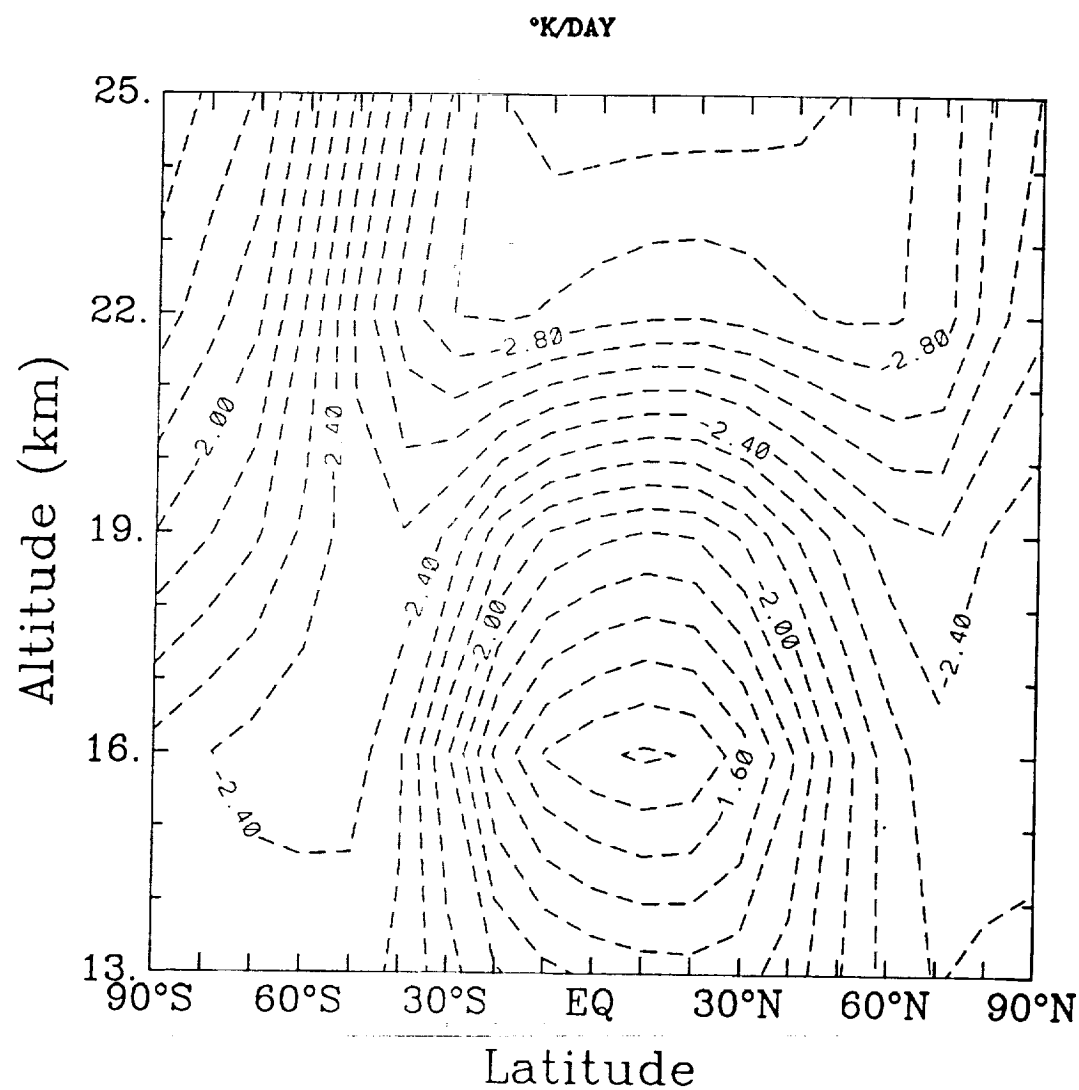


Figure 19. Same as Figure 17, except for day 210.

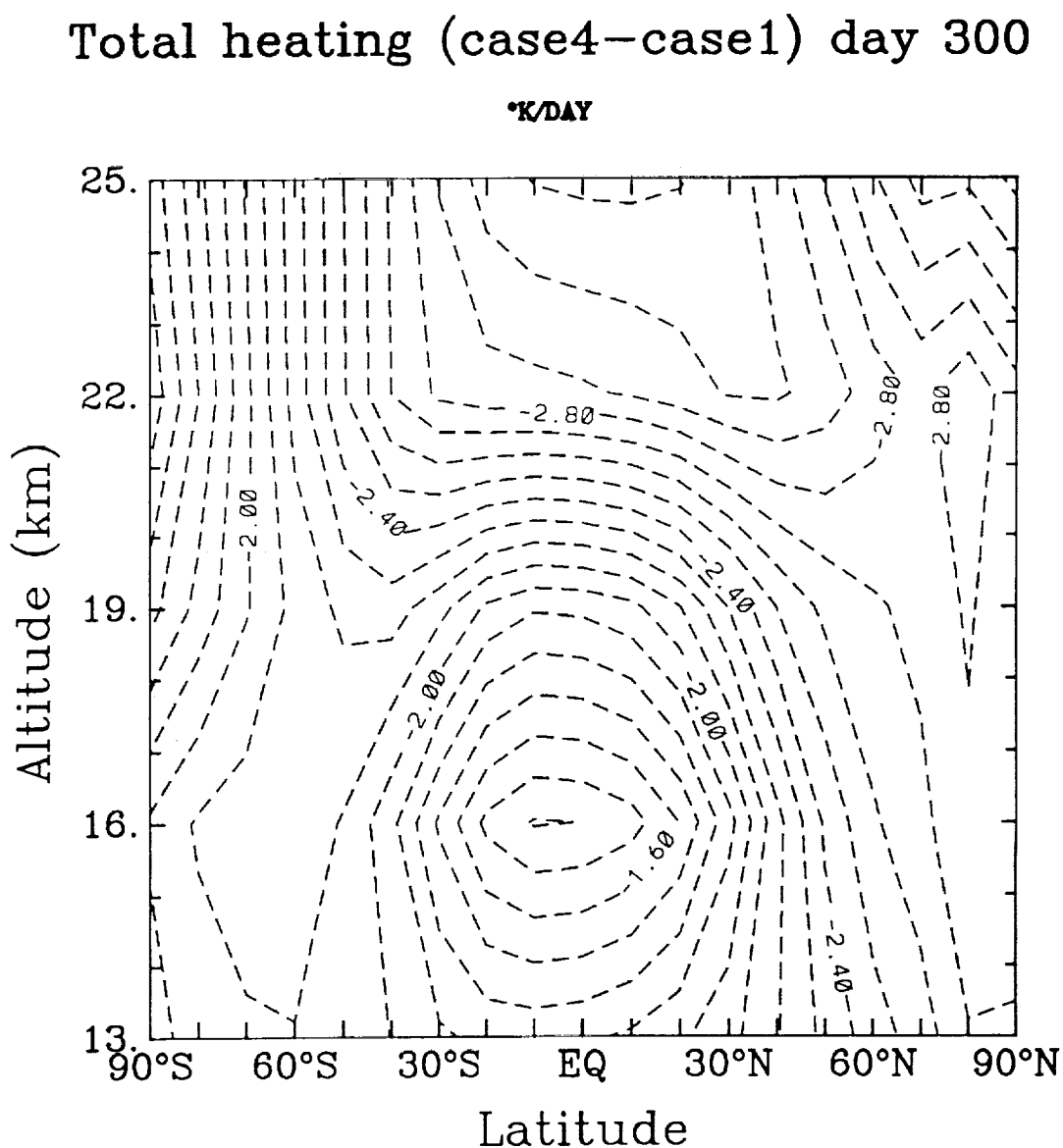


Figure 20. Same as Figure 17, except for day 300.

Chapter 4

Laboratory Studies of Stratospheric Heterogeneous Chemistry

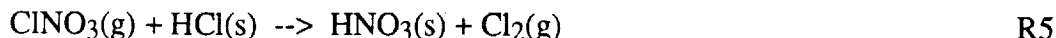
INTRODUCTION

The purpose of this aspect of our program is to evaluate the role of heterogeneous chemistry relating to the potential atmospheric effects of emissions from a fleet of supersonic aircraft flying in the stratosphere. Research needs in this area are motivated by a relative lack of knowledge of chemistry on or in aerosol particles compared to that of the homogeneous gas phase. Significant advances in our understanding of heterogeneous chemical mechanisms are required for quantitative prediction of stratospheric chemistry with or without added aircraft emissions.

The importance of heterogeneous chemical reactions on stratospheric aerosol surfaces was originally demonstrated by measurements and models of chemical constituents in the 1987 Antarctic spring (Brune et al., 1989; Fahey et al., 1989; Solomon, 1988; Salawitch et al., 1988). Subsequent arctic winter observations of ClO (Brune, 1989), NO_y (Fahey, 1989) and polar stratospheric clouds (Hofmann et al., 1989b) reinforced the theory that heterogeneous reactions on PSCs are responsible for both denitrification and chlorine activation which are necessary precursors for the large ozone depletions observed in the Antarctic polar stratosphere.

More recent analysis of Arctic data, directly correlating aerosol appearance and perturbation of (radical) chemical partitioning (Kawa et al., 1991a, 1991b), serves to highlight the complexity of the complete gas/aerosol system. Those studies have focused on discrepancies between Arctic and Antarctic aerosol observations and the H₂O/HNO₃ phase diagram (Hanson and Mauersberger, 1988a) that is believed to control aerosol appearance. These observations of apparent chemical perturbation via aerosols have been supported by a growing collection of laboratory data which have shown that heterogeneous processes are more rapid than previously believed and that chemical conversions on cold aqueous surfaces can result in gaseous products (Molina et al., 1987; Tolbert et al., 1987, 1988a, 1988b; Quinlan et al., 1990; Reils et al., 1990; Worsnop et al., 1988; Watson et al., 1990; Van Doren et al., 1990, 1991; Leu, 1988a, 1988b; Moore et al., 1990; Mozurkewich and Calvert, 1988). These data, coupled with the field measurements in the Arctic and Antarctic, provide a qualitative picture of the role of heterogeneous chemistry in the polar stratosphere.

Through the following reactions occurring on PSCs



the chlorine reservoir species ClNO₃ and HCl are converted to gas phase products which photolyze to eventually form ozone-reactive ClO. Denitrification of the stratosphere also occurs from the

conversion of ClNO_3 and N_2O_5 (and condensation of gaseous HNO_3) to $\text{HNO}_3(\text{s})$ which impedes the formation of ClNO_3 , thereby maintaining high levels of ClO .

A key question is the formation and chemical composition of the aerosol particles referred to as (s) in R1-R6. It was the presence of PSCs that correlated with the spring ozone depletion over Antarctica. At the coldest temperatures observed there (185 K), PSCs clearly are composed of ice particles, probably containing significant amounts of HNO_3 . At least some of these are large enough to precipitate, contributing to extreme denitrification and dehydration of the Antarctic stratosphere. Enhanced aerosol densities were also observed at higher temperatures, above the frost point of ice (McCormick et al., 1982). These were predicted to be composed of nitric acid trihydrate (NAT) solid solutions (Toon et al., 1986). Comparison of stratospheric mixing ratios of HNO_3 and H_2O with laboratory measurements of temperature dependent partial vapor pressures above $\text{H}_2\text{O}/\text{HNO}_3$ mixtures were consistent with this (Hanson and Mauersberger, 1988a, 1988b).

The results presented in this report have confirmed and extended the Hanson and Mauersberger (1988a, 1988b) results. In addition to reproducing their equilibrium vapor pressure diagram for NAT, our results have resolved non-equilibrium effects relating to slow diffusion within the condensed solid phase and to supersaturation of gas phase HNO_3 with respect to NAT nucleation. In the stratosphere, slow solid diffusion may result in non-homogeneous NAT/ice particles, especially in air parcels that cycle through cooling and warming events (Wofsy et al., 1990). As mentioned above, HNO_3 supersaturation can explain discrepancies between Arctic observation of aerosols as predicted by the equilibrium NAT phase diagram (Kawa et al., 1991b).

Over the past few years, these field and laboratory observations have spurred attempts to model the potential role of heterogeneous chemistry on a global scale in the stratosphere. Hofmann and Solomon (1989) estimated that the influx of sulfate aerosol into the stratosphere from the El Chichon volcanic eruption in 1983 may explain reduced NO_2 and O_3 levels observed in the northern hemisphere in the subsequent two years. Others have modeled potentially significant effects on global ozone levels by extrapolating simple parameterizations of (polar) heterogeneous chemistry to mid-latitudes (Rodriguez et al., 1988; Isaksen, 1989). At the same time, the diversity of in situ chemical and aerosol observations both in general and especially during the arctic winter have served to emphasize the complexity of the phenomena.

The problem with these modeling attempts is that they rely on rather crude parameterizations of heterogeneous reaction rate parameters based on the limited laboratory data available for reactions R1-R6. For example, Hofmann and Solomon (1988) and Isaksen (1989) used values from previous work in our laboratory for N_2O_5 reaction (R3) and reactivity coefficient data of Tolbert et al. (1988b) for ClNO_3 with and without HCl (R4 and R5) on sulfuric acid surfaces. Rodriguez et al. (1988) parameterized the effective reaction rates for R1 and R6 in terms of the equivalent gas phase reaction rate necessary to explain the high ClO levels observed in the Antarctic spring and then scaled those rates to the global stratosphere by scaling according to the total aerosol surface area.

Such parameterizations ignore both the diversity of the aerosol conditions in the stratosphere and the details of the experiments that measured the heterogeneous rates. Each experiment measures an effective heterogeneous rate that can depend on parameters such as trace gas density, gas-surface exposure time, and method of surface preparation. In our laboratory kinetic measurements we have shown that experimental rate determinations are often only a measure of gas solubility in the condensed phase. Likewise, our new vapor pressure measurements indicate that surface composition can deviate significantly from the interior solid, depending on gas/surface interactions (Worsnop et al., 1992). For reactive processes such as R5-R6, detailed knowledge of the chemical mechanism is needed to quantitatively relate laboratory kinetic data to atmospheric

conditions. Furthermore, that modeling must take into account the distribution of aerosol density and composition that will in general be variable in H_2O , HNO_3 and H_2SO_4 .

This need for more sophisticated treatment of both the atmospheric surfaces and the heterogeneous chemical kinetics is the backdrop on which potential heterogenous perturbations due to stratospheric aircraft need to be considered.

PERTURBATIONS FROM AIRCRAFT EMISSIONS

The HSRP program is indeed focusing much of its effort on development of stratospheric modeling programs, since the effect of aircraft emissions can only be predicted via model simulation. Clearly the first step involves improving the capability of modeling the present stratosphere. Along those lines, appropriate inclusion of heterogeneous chemistry is a major issue for model development. In fact, this has been demonstrated in a new calculation by the group at AER (Weisenstein, et al., 1991), which has included reaction R3 for N_2O_5 on global background H_2SO_4 aerosol. Using reaction rates for R3 measured in our laboratory (Van Doren et al., 1991) and others (Mozurkowich and Calvert, 1988), they predict that R3 shifts partitioning of NO_x to HNO_3 , which in turn shifts Cl_x/NO_x chemistry leading to O_3 depletion by Cl_x . This calculation actually predicts that NO_x emission from HSCT aircraft would increase O_3 by partially neutralizing the Cl_x destruction cycle. At this point, such a calculation re-emphasizes the need to treat stratospheric heterogeneous chemistry as completely as possible.

The impact of emissions from stratospheric aircraft must be considered at local and global levels. The aircraft fleet is projected to fly at altitudes between 18 and 23 km. This corresponds to the lower stratosphere, extending down to the top of the tropopause and overlapping the natural sulfate aerosol layer. The local temperature and trace gas profiles of aircraft plumes can be expected to have spatial and temporal scales of hundreds of meters and hours. Emission of high (relative to background stratospheric levels) densities of H_2O , NO_x , SO_2 , and condensation nuclei can be expected to significantly perturb aerosol density and composition within these plumes. These plumes are expected to mix on a timescale of days, giving a "zonal average" in aircraft flight corridors. Obviously on a longer timescale there is dispersion throughout the stratosphere as well as mixing down into the top of the troposphere.

Quantitative modeling of perturbed stratospheric profiles requires detailed coupling of both homogeneous and heterogeneous chemistry with transport models, which is the overall goal of the HSRP program. In this context, the plume mixing scenario represents an extension of the range of gas and temperature conditions that need to be investigated. In fact, the higher temperatures and trace gas densities associated with the aircraft plumes are somewhat easier to study in the laboratory than those of the unperturbed stratosphere. This may be particularly true for heterogeneous interactions of NO_x and SO_2 with aerosols

OVERVIEW OF EXPERIMENTAL PROGRAM

In separate collaborations with Boston College and Harvard University, Aerodyne Research has developed laboratory projects for measuring heterogeneous kinetic and thermodynamic parameters. Together with the group of Professor Paul Davidovits of Boston College, a technique based on coupling a fast-moving train of liquid droplets with a gas flow tube has successfully measured a number of gas/surface accommodation/reaction processes of tropospheric and stratospheric interest. Together with the group of Professor Steven Wofsy of Harvard an apparatus consisting of a cooled infrared absorption cell has been used for the determination of

vapor pressures of solid solutions. Both of these projects provide state-of-the-art experimental approaches to the difficult problems associated with studying heterogeneous processes.

At the same time, this collaborative approach provides a unusually broad perspective on the issues involved. Although the two experimental projects have been programmatically separate, they complement and synergistically interact on personnel, technical and scientific levels. The collaboration of Aerodyne staff members, Professors Davidovits and Wofsy, and students and postdoctoral associates from the academic groups has brought together a unique combination of physical and atmospheric scientists. On a technical level, the two projects utilize the same diode laser techniques for trace gas detection as well as bringing together different perspectives on the practical problems associated with preparing well-defined surfaces in the laboratory. Scientifically the issues of aerosol composition and chemistry obviously are deeply intertwined.

HETEROGENEOUS KINETIC STUDIES

Introduction

Because of the small surface area and cold temperature of stratospheric aerosols, it was believed until recently that the likelihood of significant stratospheric heterogeneous chemistry was very small. Field measurements correlating Antarctic ozone depletion with PSCs and surprisingly large heterogeneous rates measured in the laboratory have changed that view. However, a much more detailed understanding of the underlying chemical mechanisms is required before these results can be quantitatively applied to heterogeneous processes in the global stratosphere, with or without added perturbation from aircraft emissions. Below we discuss the issues involved in improving that understanding.

The rate of uptake of gas into a condensed phase can be expressed as a pseudo first order rate by the expression

$$k = \frac{\gamma \bar{c} A}{4} \quad (1)$$

where \bar{c} is the molecular velocity (cm s^{-1}) and A is the aerosol surface area density ($\text{cm}^2 \text{cm}^{-3}$). The parameter γ , often referred to as the "sticking coefficient", is the probability of gas uptake into a surface upon collision with the surface. More precisely, in the case of direct accommodation, as for HCl and HNO_3 in R1 and R2, γ is the mass accommodation coefficient; for uptake involving reaction, as for N_2O_5 and ClNO_3 in R3 and R4, γ is the reactivity coefficient.

Analysis of most laboratory data and its application to atmospheric modeling has been solely in terms of Eq. (1). Experimental uptake measurements are simply compared to the surface collision rate to extract a value of γ . This over-simplified interpretation ignores the fact that, even for simple accommodation processes such R1 and R2, experimentally observed gas uptake measurements in general involve a combination of processes. In particular, one must always evaluate the degree of saturation of the surface. In the case of bimolecular processes such as R5 and R6, the dependence of heterogeneous rates on gas concentration is obviously important, especially when laboratory densities are much higher than in the atmosphere.

Equation (1) does provide a simple framework to evaluate the potential role for heterogeneous processes. Under typical stratospheric conditions the surface area, A , peaks at about $10^{-8} \text{ cm}^2 \text{cm}^{-3}$ between 15 and 20 km altitude, decreasing to about 10^{-9} at 30 km (Turco et al., 1981). Thus, even in the limit of $\gamma = 1$, the maximum heterogeneous rate is on the order of 10^{-4} s^{-1} . In other words, heterogeneous processes in the stratosphere can be significant only for gaseous species with

long reactive lifetimes. Until recently it was generally believed that γ would be small at stratospheric temperatures, making heterogeneous kinetics unimportant.

The polar field observations and various laboratory results have changed that view. The correlation between ozone depletion and the presence of PSC's combined with laboratory measurements of $\gamma > 0.01$ even for bimolecular heterogeneous reactions such as R5 and R6 now indicate that heterogeneous processes can indeed be significant, at least under polar conditions. More generally, results from our laboratory have shown that direct mass accommodation for molecules such as HCl and HNO₃ on aqueous surfaces (R1 and R2) is efficient (Watson et al., 1990). The accommodation probability for a number of molecules has a negative temperature dependence so that γ approaches unity at stratospheric temperatures. This extrapolation is consistent with results for H₂O, HNO₃ and HCl accommodation on cold (200 K) ice and NAT surfaces which give lower limits on γ approaching unity within experimental limits (Leu, 1988a; Moore et al., 1990; Molina et al., 1987; Tolbert et al., 1988; Quinlan et al., 1990).

For such large values of γ , the rates of direct accommodation processes such as R1 and R2 become irrelevant. For small aerosol particles under stratospheric conditions, molecular density in the particles will equilibrate with the gas density on timescales much shorter than a second. Thus, for both atmospheric and laboratory conditions the important parameter is the gas solubility in the condensed phase.

A case in point is the uptake of HCl into aqueous sulfuric acid solution measured as a function of H₂SO₄ mole fraction. The decrease in observed HCl uptake with increasing H₂SO₄ mole fraction may be modeled by the equation

$$\gamma = \frac{\alpha}{1 + \frac{\alpha \bar{c}}{4 H^* RT} \left[\frac{D}{t} \right]^{1/2}} \quad (2)$$

The key parameters are the effective HCl Henry's law coefficient H* (which depends on the dissociation of HCl(aq) into H⁺ and Cl⁻), the liquid diffusion coefficient D, the gas/liquid exposure time (2 x 10⁻³ s in our experiment), and the true mass accommodation coefficient α . The data can be quantitatively modeled using bulk solution parameters, consistent with uptake limited by time-dependent, diffusion-limited saturation of the liquid surface. This mechanism is also consistent with data of Reihs et al. (1990). Applying this analysis to their HCl uptake data, one can extract a value of H*(D)^{-1/2} for HCl in 65 wt% H₂SO₄ solution at 205 K. The key question there is the physical state of the aqueous H₂SO₄ surface, which determines the value of D. Depending on whether the surface is frozen or not, the value of H* for HCl is 30 to 10⁴ times larger at 205 K than at 283 K.

The values of H* and D for HCl are also critical to evaluating the rates of the bimolecular reactions R5 and R6. In analogy with Eq. (2), one can derive an expression for γ that compares the rates of condensed phase reaction and re-evaporation due to saturation. In the limit of reaction rate limited uptake,

$$\gamma_R = \frac{4 H_R RT}{\bar{c}} \langle D k_R H^* RT [HCl(g)] \rangle^{1/2} \quad (3)$$

where H_R is the Henry's law solubility of reactant R and k_R is the bimolecular rate constant for condensed phase reaction of HCl with reactant R.

The heterogeneous rates reported for reactions such as R5 and R6 ($\gamma > 0.01$) need to be compared to Eq. (3). Again a key parameter is the diffusion coefficient for HCl(s). Originally D for HCl in ice was reported to be unusually large, $\sim 10^{-5}$ cm² s⁻¹ (Molina, 1987), which indicated that reactions R5 and R6 could access all HCl(s) dissolved in aerosol particles. However, in a separate study it was pointed out that HCl in single crystals of ice actually is slow, though HCl is readily adsorbed and transported along grain boundaries (Wolff et al., 1989). Using a typical value of $D = 10^{-11}$ cm² s⁻¹ in solid solution, assuming $H^*(HCl) = 10^{10}$ M atm⁻¹, and assuming diffusion limited k_R of 10^4 M⁻¹ s⁻¹, for [HCl(g)] = 10^9 cm⁻³, we obtain

$$\gamma = H_R \times 10^{-6}$$

This estimation is based on upper limits for the bulk phase parameters. For example, recent measurements indicate that the actual equilibrium solubility of HCl in ice may be significantly smaller (Hanson and Mauersberger, 1989). While little is known about the values of H_R for species such as ClNO₃ and N₂O₅, it is hard to reconcile the large observed rates for R5 and R6 ($\gamma > 0.01$). It is also significant that these rates appear to be more or less independent of the condensed surface, whether ice, NAT or aqueous H₂SO₄. This, combined with the fact that R5 and R6 rates are comparable to those for R3 and R4 reactions with H₂O(s) that is in huge excess, points toward a surprisingly efficient surface reaction.

Evaluation of surface reaction rates requires knowledge of surface concentrations of adsorbed reactant molecules. Turco et al. (1989) have discussed the thermodynamics of so-called adsorption isotherms and estimated that surface binding energies on the order of 10 to 20 kcal mol⁻¹ are required to give significant surface densities. In their analysis, they implicitly concluded that the reported efficiencies for reactions R3 to R6 were consistent with such surface densities. The rate of reaction of two adsorbed species such as HCl and ClNO₃ also is dependent on their mobility on the surface, which is related to the entropy change associated with the adsorption isotherm. It should be noted that in general the rate of such a bimolecular surface reaction is proportional to the product of the molecular surface densities, each of which is in general proportional to the respective gas densities. However, in the limit of high (e.g. laboratory) gas densities it is easy to saturate surface densities and observe heterogeneous rates that are independent of gas density.

This mechanism of surface adsorption is consistent with results from our laboratory for mass accommodation on aqueous surfaces. For the series of molecules H₂O₂, HNO₃, HCl and N₂O₅, a negative temperature dependence was observed that was consistent with surface binding energies of at least 5 to 10 kcal mol⁻¹ (Worsnop et al., 1989; Van Doren et al., 1990). In the case of SO₂, the density of the surface state was directly measured, again consistent with a surface binding energy on the order of 10 kcal mol⁻¹ (Jayne et al., 1990). These results were interpreted in terms of general accommodation mechanism involving initial adsorption on the liquid surface. The rate-limiting step for accommodation into the liquid was then the rate of solvation of the surface-bound molecule. The actual accommodation coefficient then reflected the competition between solvation and re-evaporation of the surface state.

These measurements need to be extended to lower temperatures for the chemical species and surfaces relevant to R1 - R6 in the stratosphere. If indeed heterogeneous chemistry occurs via surface adsorption, the surface densities will be observable using the experimental techniques developed in our laboratory. The key capability is the millisecond resolution for gas/liquid exposure times. This permits the resolution of the initial adsorption from the equilibration of adsorption on longer timescales.

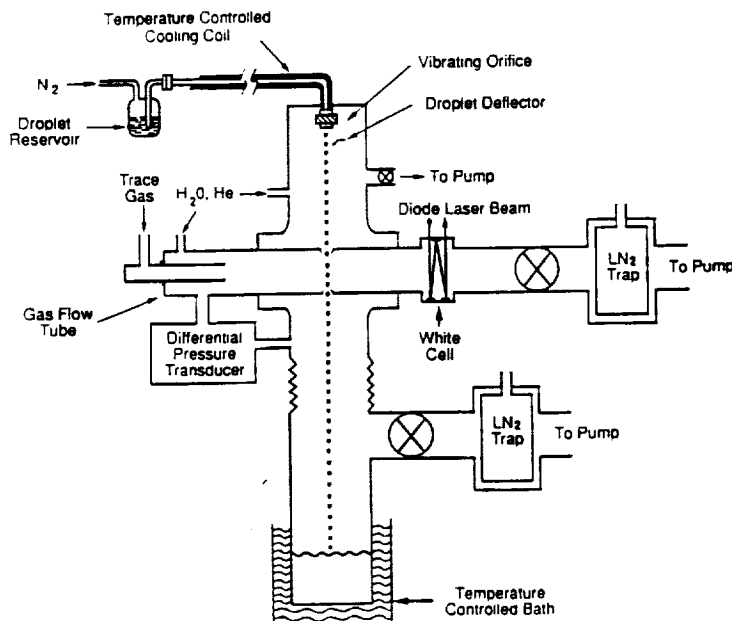
In this report we present experimental data on the uptake of HCl on cold sulfuric acid droplets. Understanding the uptake, coefficients in terms of the solubility of HCl is the first step in probing

surface reactivity of gas phase species on stratospheric sulfate aerosols reased by adsorption on aerosols.

Experimental Measurements of HCl Uptake On Sulfuric Acid Droplets

We have measured the uptake of gas phase HCl by droplets of sulfuric acid as a function of droplet temperature and concentration. A fast-moving (~3500 cm/s) train of concentrated sulfuric acid droplets (40, 50, and 70 wt%) is formed by passing pressurized acid through a 70 μm orifice in a thin platinum disk that is mechanically vibrated using a piezoelectric ceramic. The droplet surface area is varied by switching the droplet frequency which changes the diameter and spacing of the droplets (droplet diameter \approx 160 μm). The droplet train travels coaxially down a 30 cm long, 1.5 cm ID glass flow tube in which helium is used as the carrier gas. HCl mixed with helium is introduced using one of three Teflon loop injectors positioned downstream of the orifice.

The contact distances of HCl with the droplet stream are 5.5, 16.0, and 29.5 cm which, for a droplet velocity of 3500 cm/s, correspond to droplet-HCl exposure times of 1.6 - 8.4 ms. A White cell connected to the downstream end of the flow tube allows for tunable diode laser infrared absorption measurements of the HCl concentration as a function of the total surface area of the stream exposed to HCl.



A-852b

Figure 4.1. Schematic of the Apparatus for the Measurement of Uptake Coefficients

The acid is cooled to temperatures in the range 230 - 260 K using a refrigeration bath and a circulation pump. A thermocouple placed just above the nozzle is used to monitor the liquid temperature. Tunable diode laser infrared absorption measurements of the ambient water vapor in the flow tube are used to determine droplet temperatures and thereby calibrate the nozzle thermocouple.

In cases where the physical solubility of a gas in a liquid is limited, the slope of a plot of the inverse of the uptake coefficient (γ) versus the square-root of the gas-droplet contact time yields the Henry's law solubility constant and the intercept gives the gas-liquid mass accommodation coefficient. In Figure 4.2, γ^{-1} is plotted against $t^{1/2}$ for HCl on 50 wt% H_2SO_4 at four temperatures. Note that the slopes of the lines decrease as the temperature decreases, reflecting the increased solubility of a gas in a liquid at lower temperatures (slope $\propto H^{-1}$, where H is the Henry's law constant). In addition, $\gamma(0)$ increases as the droplet temperature decreases, in agreement with our model for mass accommodation on aqueous surfaces [Watson et al., 1990] which predicts that the mass accommodation coefficient (α) increases as the surface temperature of the liquid decreases (we believe that the 251 K experiment is consistent with the other data within experimental error). In Figure 4.3, the logarithm of the *effective* Henry's Law constant, H^* ($H^* = H(1+K_a/[H^+])$, where K_a is the HCl dissociation constant) is plotted against T^{-1} . Note that the data point at 283 K represented by the open square was obtained from an earlier set of experiments [Watson et al., 1990]. In Figure 4.4, a plot of $\log(\alpha/(1-\alpha))$ vs. T^{-1} is presented using data for HCl uptake by 40 and 50 wt% sulfuric acid as well as data for HCl uptake by water.

Experiments on HCl uptake by 40 wt% H_2SO_4 droplets reveal that γ is independent of HCl-droplet contact time (Figure 4.5). This is in contrast to the HCl uptake data at 50 wt% (Figure 4.2) which vary markedly with contact time. This behavior is consistent with earlier experiments at 283 K where it was determined that HCl solubility in sulfuric acid is limited by the rate of the acid dissociation reaction $\text{HCl(aq)} \rightarrow \text{H}^+(\text{aq}) + \text{Cl}^-(\text{aq})$. The more concentrated the acid solution, the

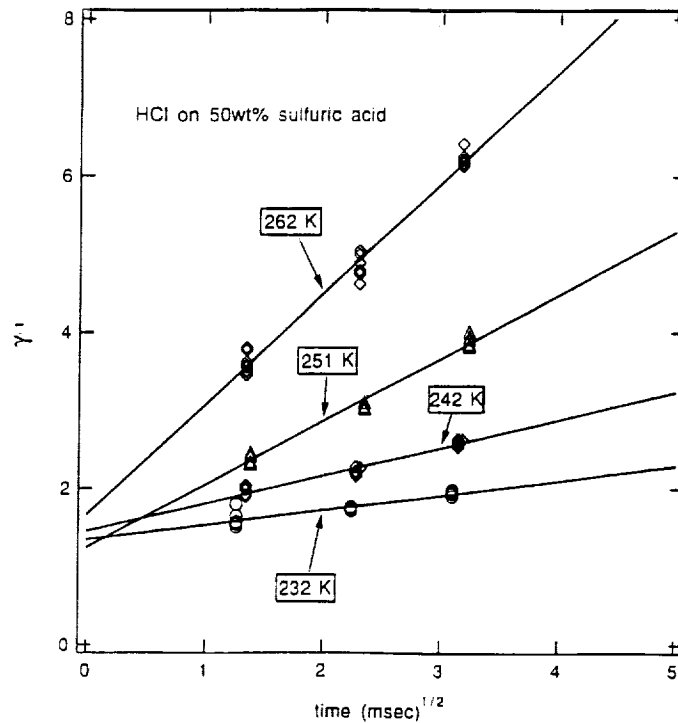


Figure 4.2. Plot of γ^{-1} Versus $t^{1/2}$ for 50 wt% H_2SO_4

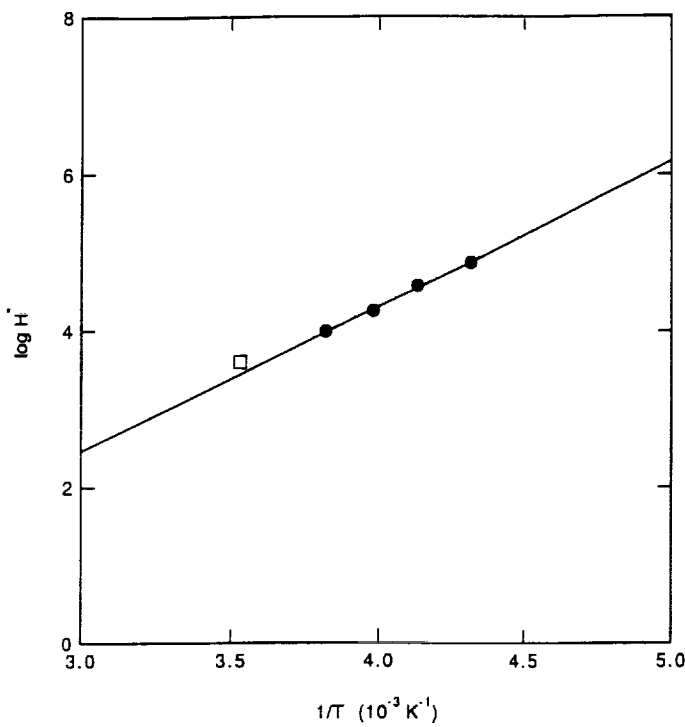


Figure 4.3. Plot of Effective Solubility H^* for HCl in 50 wt% H_2SO_4 Versus $1/T$

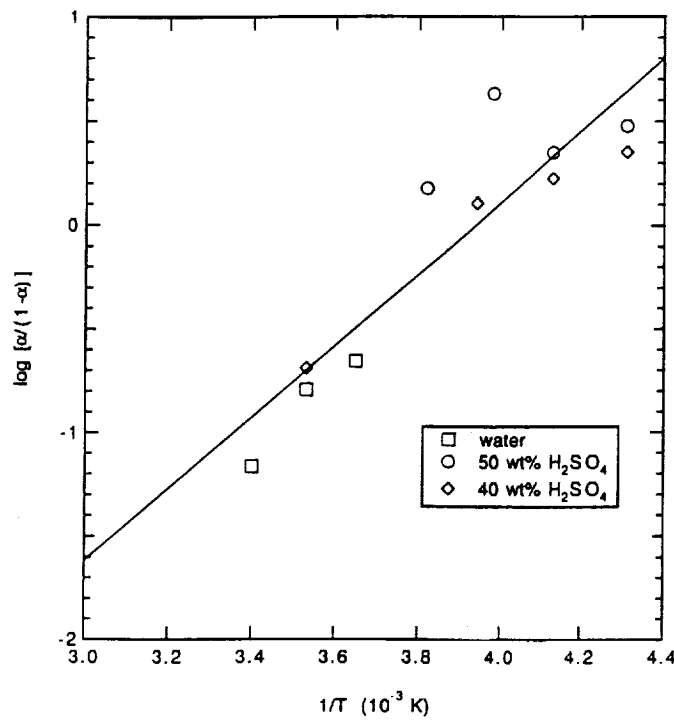


Figure 4.4. Plot of True Mass Accommodation Coefficient α Versus $1/T$

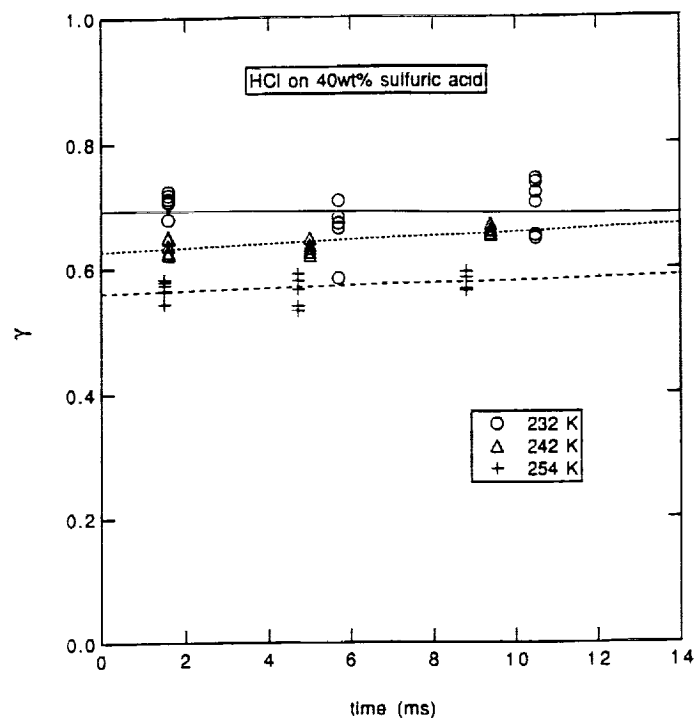


Figure 4.5. Plot of γ Versus t for 40 wt% H_2SO_4

less significant this reaction becomes. The flatness of the lines in Figure 4.5 indicates that the Henry's law constants for 40 wt% H_2SO_4 are too large to be determined from our data. In experiments on 70 wt% H_2SO_4 droplets at 238 K, on the other hand, no HCl uptake was detectable. Additional experiments are underway to complete the experimental matrix of temperature, wt% H_2SO_4 , and contact time. These data will lead to the best values for the solubility of HCl in H_2SO_4 under stratospherically relevant conditions.

STRATOSPHERIC AEROSOL THERMODYNAMICS

Introduction

Aerosols in the stratosphere are typically composed of aqueous H_2SO_4 particles whose composition depends on the local temperature and water vapor pressures. This behavior is summarized in the phase diagram shown in Figure 4.6, which plots water vapor pressure versus temperature. The contour lines correspond to water vapor pressure curves of aqueous H_2SO_4 solutions (labeled by their H_2SO_4 composition in wt %). The vertical scale on the right shows the corresponding altitude assuming a constant 5 ppm water vapor mixing ratio typical of stratospheric conditions, giving H_2SO_4 solutions in the 60 to 80 wt % range at temperatures of 205 to 225 K. These aerosol particles are typically < 0.1 mm in diameter and believed to be in a supercooled liquid state. Total aerosol surface area peaks at about $10^{-9} \text{ cm}^2 \text{ cm}^{-3}$ in the 15-20 km altitude range, forming the Junge aerosol layer. This general picture has been quantitatively confirmed by extensive balloon measurements (Hofmann and Rosen, 1983, 1984), particularly after the El Chichon volcanic eruption which significantly enhanced aerosol densities (Hofmann, 1987).

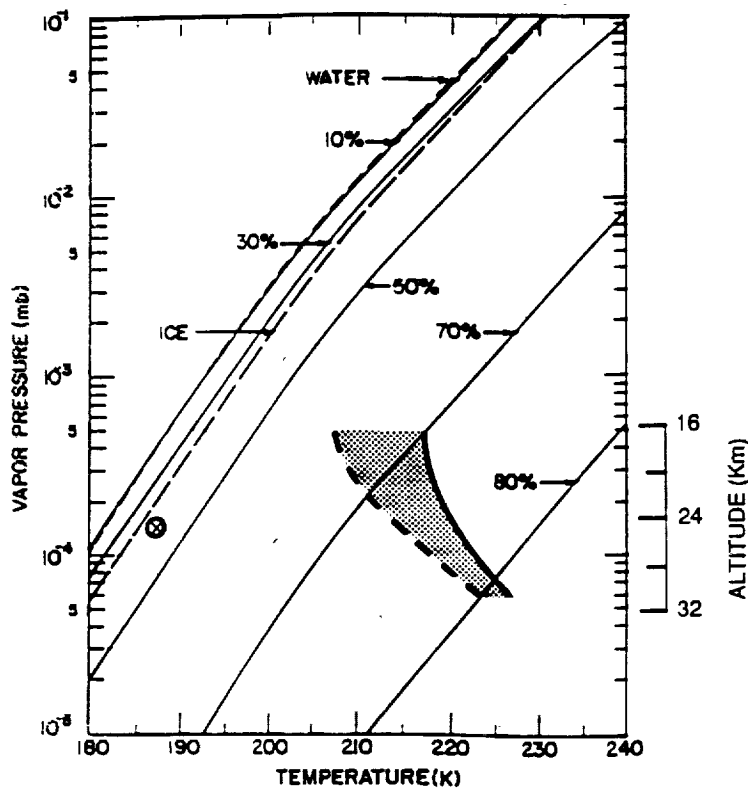


Figure 4.6. Phase Diagram for H_2O Vapor Pressure Versus T. Contour lines for Aqueous H_2SO_4 Solution (H_2SO_4 Concentration in Weight %).

Until recently it was believed that the only major exception to this behavior occurred near the poles where low temperatures in the winter led to the formation of PSCs containing ice particles (Stormer, 1929). One simply moved across the phase diagram to the circled x on the lower left of Figure 3.1. It was believed that as winter temperatures at high latitudes approached the frost point, PSCs grew by accretion of H_2O on the background H_2SO_4 nuclei (Steele et al., 1983).

With the observation of large springtime ozone depletions over Antarctica, however, detailed analysis of observations from the SAM II instrument on Nimbus 7 (McCormick et al., 1982) provided evidence of significant aerosol enhancement at temperatures above the water frost point. Toon et al. (1986) suggested that HNO_3 might be a major component of these PSCs, and that significant quantities of HCl might be incorporated as well. This led to attempts to construct phase diagrams for equilibria of H_2O , HNO_3 and HCl for stratospheric conditions (Wofsy et al., 1988; McElroy et al., 1986).

In the case of the binary $\text{H}_2\text{O}/\text{HNO}_3$ system, these phase diagrams have been well reproduced by laboratory vapor pressure measurements originally reported by Hanson and Mauersberger (1988a, 1988b) and now confirmed in our laboratory (Worsnop et al., 1992). The experimentally

measured phase diagram is shown in Figure 4.7. The lines increasing diagonally to the left represent NAT vapor pressures obeying the relation

$$P_{H_2O}^3 P_{HNO_3} = K_T$$

The dashed lines represent previous measurements of Hanson and Mauersberger (1988a) while the points and solid lines are from our laboratory. The bolder diagonal lines increasing to the right show vapor pressures measured over samples of coexisting phases as labeled. The agreement between measurements from the two laboratories is excellent.

The X in the center of Figure 4.7 corresponds to typical background HNO_3 and H_2O levels seen over Antarctica during field missions in August, 1987 (Fahey et al., 1989). That point intersects and NAT curve at 196 K, 6 K warmer than the 190 K frost point for ice found on the NAT/ice coexistence curve directly below it. Measurement of reduced stratospheric NO_y densities in those 1987 field missions were indeed consistent with NAT condensation at higher temperatures relative to ice as predicted by the phase diagram in Figure 4.7. In fact, the boundary of the perturbed

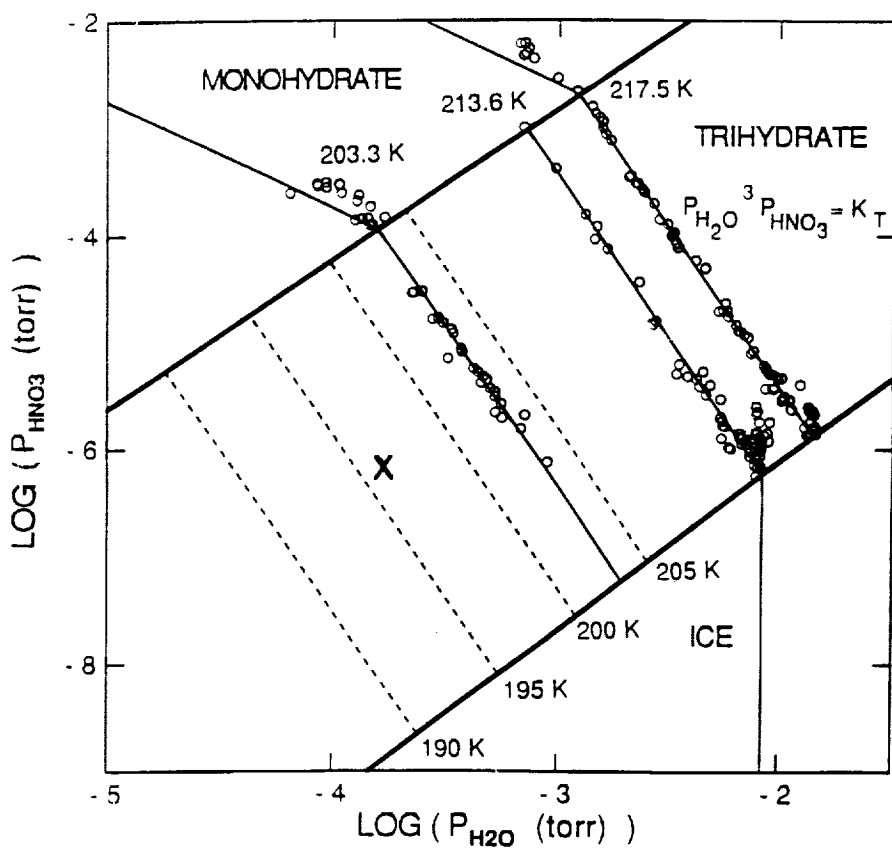


Figure 4.7. Phase Diagram for HNO_3 and H_2O Partial Pressure as a Function of T for HNO_3/H_2O Condensates. Points from Worsnop et al (1992); dashed lines from Hanson and Mauersberger (1988b).

a chemical region within the Antarctic vortex could be delineated by the NAT condensation conditions predicted by that phase diagram (Fahey et al., 1989).

In contrast, detailed analysis of Arctic field observations in the stratosphere indicates there is a discrepancy between NAT phase diagram predictions and aerosol formation (Kawa et al., 1991a, 1991b). Apparently aerosol free air is observed with HNO_3 vapor densities up to a factor of 10 higher than allowed by the NAT equilibrium relation (K_T). The authors hypothesize that this may reflect the degree of HNO_3 super saturation required to nucleate NAT on H_2SO_4 aerosol particles. The apparent difference in temperature threshold for aerosol formation between the arctic and Antarctic can be explained by differences in temperature history of the sampled air particles, with those observed in the Antarctic spring having been colder for longer periods of time. A related question is whether the physical state of the background H_2SO_4 aerosol plays a role. Under colder conditions, that aerosol may freeze, providing potentially better NAT nucleation sites relative to super-cooled liquid droplets (Dye et al., 1991).

Our laboratory results support this supersaturation effect. The experimental method and these results are discussed in the following sections.

Experimental Apparatus for Thermodynamic Measurements

Our method for measuring vapor pressures in equilibrium with solid solutions of HNO_3 , HCl , H_2O and H_2SO_4 is based on infrared absorption using a tunable diode laser and a cryogenic temperature multiple-pass absorption cell. The apparatus shown in Figure 4.8 consists of a 4-inch diameter, high-vacuum, pyrex inner chamber which contains the multipass-cell mirrors. The solid sample is deposited at the bottom of the chamber on a cold spot which is ~6 mm in diameter.

Cryogenic temperatures in the range 180 to 250 K are obtained by passing a regulated nitrogen gas flow through a heat exchanger immersed in a liquid nitrogen reservoir. This flow is then directed through a diffuser frit on the bottom of the surrounding stainless steel chamber. A heater on the diffuser frit regulates the temperature of a copper button which is epoxied onto the bottom of the pyrex inner chamber. A copper shield with a separate heater/sensor assembly is used to maintain the walls of the inner chamber and the mirrors at a temperature greater than the cold spot on the bottom. The entire assembly is enclosed in an evacuated stainless steel dewar for insulation.

The tunable diode laser infrared absorption system uses a Laser Analytics cold head, current and temperature control modules. A laboratory microcomputer is used to scan the laser current and to signal average the detector output to obtain direct absorptions with a sensitivity of 10^{-5} fractional absorption. The multipass mirrors in the cryogenic cell are of the off-axis resonator Herriott type and are set to obtain 40 passes with a base path length of 50 cm for a total pathlength of 2000 cm. The circular spot pattern is adjusted to minimize the amplitude of interference fringes arising from spill-over from adjacent spots (McManus and Kebabian, 1990). The gold coated pyrex mirrors are clamped concentrically to a 18 mm o.d. pyrex tube attached only to the top of the inner chamber. The clamping hardware is also gold coated so that only gold or pyrex surfaces are exposed to the gases during the vapor pressure measurements. Absorption line parameters and detection limits for selected gases are shown in Table 4-1.

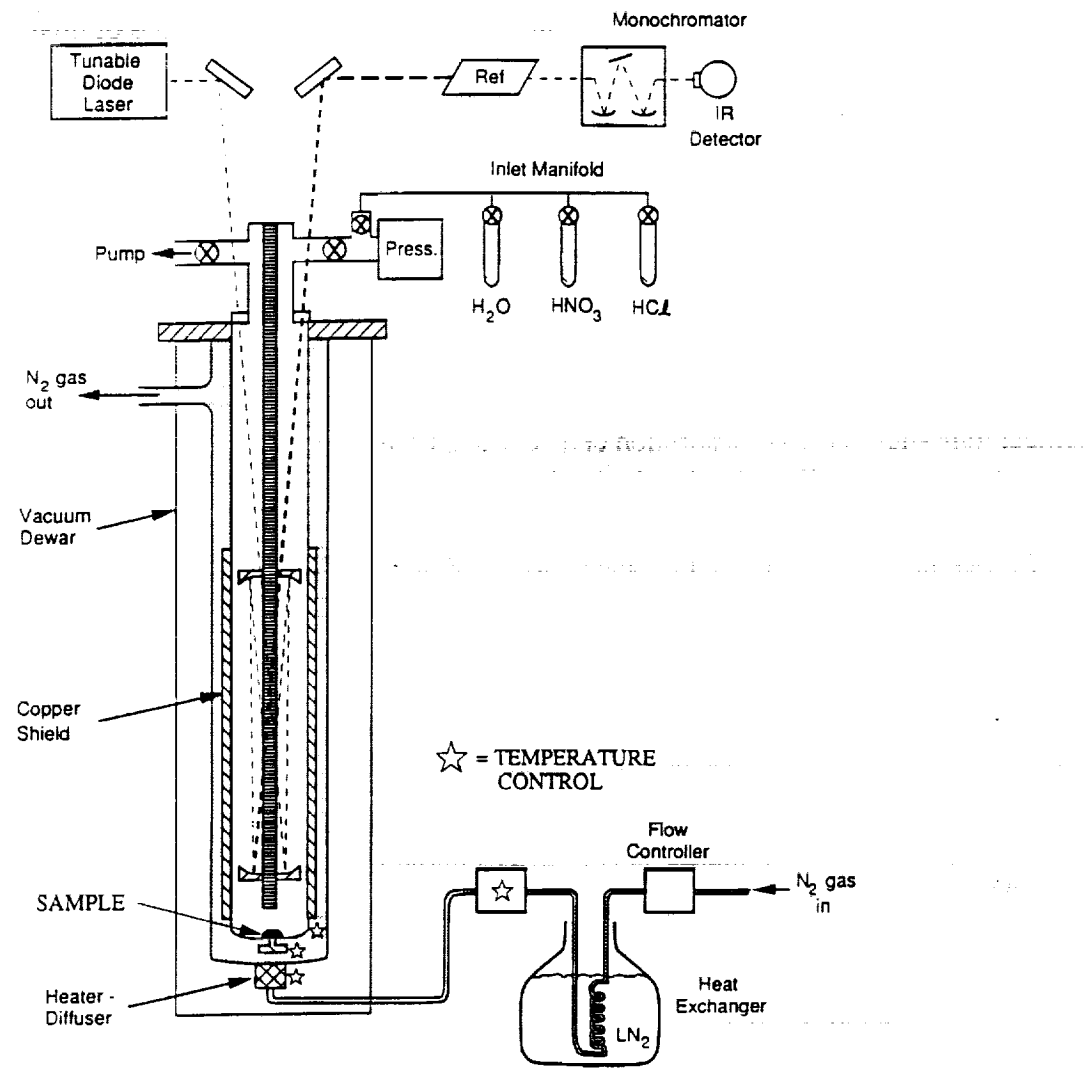


Figure 4.8. Experimental Apparatus for Vapor Pressure Measurements

Table 4-1 - Absorption Line Parameters and Detection Limits for Fugacity Measurements

Molecule	Line Position cm ⁻¹	Line Strength ^a cm ² molecule ⁻¹ cm ⁻¹	Detection Limit ^b molecule cm ⁻³
HCl	2821.570	3.1 (-19)	1.0(8)
HBr	2605.77	1.0 (-19)	2.0(8)
HNO ₃	1334.453	3.4 (-20)	3.1(8)
H ₂ O ₂	1302.506	2.5 (-20)	5.8(8)
H ₂ O	1591.673	1.7 (-21)	1.5(10)

^aLine strengths are from AFGL line compilation (Rothman et al., 1987) except for HNO₃ (May and Webster, 1987) and H₂SO₄ (Majkowski et al., 1978).

^bBased on a minimum detectable fractional absorption of $\Delta I/I_0 = 10^{-5}$ and a pathlength of 2000 cm.

All the exposed pyrex within the cells is covered with a hydrophobic C₆F₁₃C₂H₄Si-(O)₃- coating, which greatly reduces surface adsorption of H₂O/HNO₃ on the walls. This is critical to measurements of small trace gas concentrations, where it is important to eliminate wall effects which can dominate sample vapor pressures. A key aspect of the experimental design is the capability of independently controlling sample and absorption cell temperatures. Variation of the latter (controlled by the copper shield in Figure 4.8), while keeping sample temperature constant, can separate wall effects from sample vapor pressures.

CURRENT RESULTS AND STRATOSPHERIC IMPLICATIONS

HNO₃ supersaturations are observed in our laboratory measurements as seen in Figure 4.7. For the 213 K data, the points lying directly above the vertical ice line (in lower right hand corner) correspond to HNO₃ supersaturated over ice. We have observed HNO₃ supersaturations ≥ 5 that last 2-3 days over ice. Such observations are at least qualitatively consistent with the Arctic data discussed above.

In fact, HNO₃ supersaturation is repeatedly observed when an NAT free sample surface is prepared in our experiment. For example, Figures 4.9 and 4.10 show results of water addition to monohydrate (NAM) surfaces. In both figures the * points along an NAM line (above the NAM/NAT coexistence line) correspond to starting an experiment with a pure NAM surface. Adding H₂O vapor to the sample cell then increases the H₂O/HNO₃ ratio of the sample surface, moving vapor pressures into the NAT portion of the phase diagram. In Figure 4.9, at 203 K, after H₂O vapor addition to the cell, HNO₃/H₂O vapor pressures initially go to a metastable NAM/ice

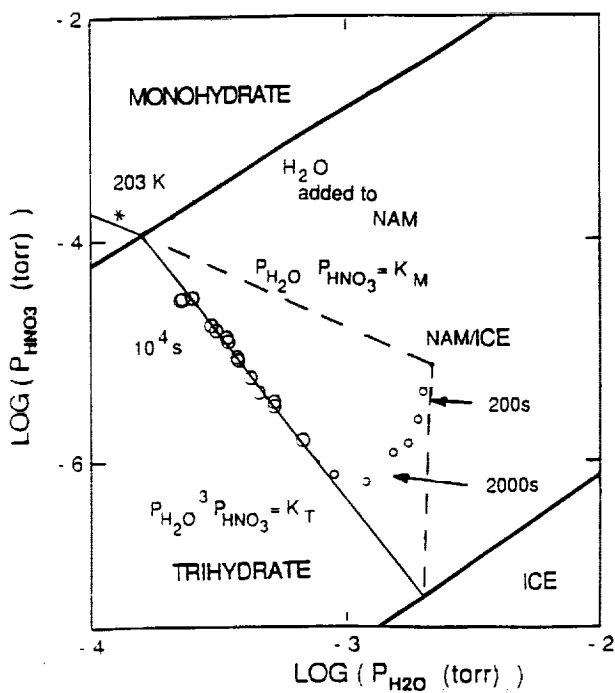


Figure 4.9. $\text{HNO}_3/\text{H}_2\text{O}$ Vapor Pressure at 203 K After Water Vapor Addition to NAM Sample (Labeled with *). Vapor pressures are close to a transient NAM/ice double point after 1 minute. Over the next hour (small circles) the vapor pressures relax to the NAT equilibrium line. Overnight (large circles) vapor pressures move toward NAM/NAT double point as the condensed surface sample equilibrates with the $\text{H}_2\text{O}/\text{HNO}_3$ ratio in the solid.

double point, found by the extending NAM and ice vapor pressures (dashed lines). Over the next hour or so the vapor pressures "relax" to the NAT equilibrium curve as an NAT layer is nucleated.

Figure 4.10 shows the result of a similar experiment performed at 213 K. The data points show $\text{HNO}_3/\text{H}_2\text{O}$ vapor pressures after successive small additions of H_2O vapor. The points fall along a line of slope 1/2, which is consistent with nitric acid dihydrate (NAD) formation. For the sample shown in Figure 4.10, further H_2O addition led to "relaxation" to the equilibrium NAT line as in Figure 4.9.

The behavior in Figures 4.9 and 4.10 can be interpreted in terms of the degree of HNO_3 supersaturation required for NAT nucleation. In Figure 4.9, the NAM/ice double point is supersaturated by over 100 in HNO_3 ; thus, NAT nucleation began on a time scale of minutes. In Figure 4.10, condensation of a NAD surface layer occurred until HNO_3 supersaturation of ~ 10 led to NAT nucleation. In both cases, metastable, transient phases (i.e., NAM/ice and NAD) were

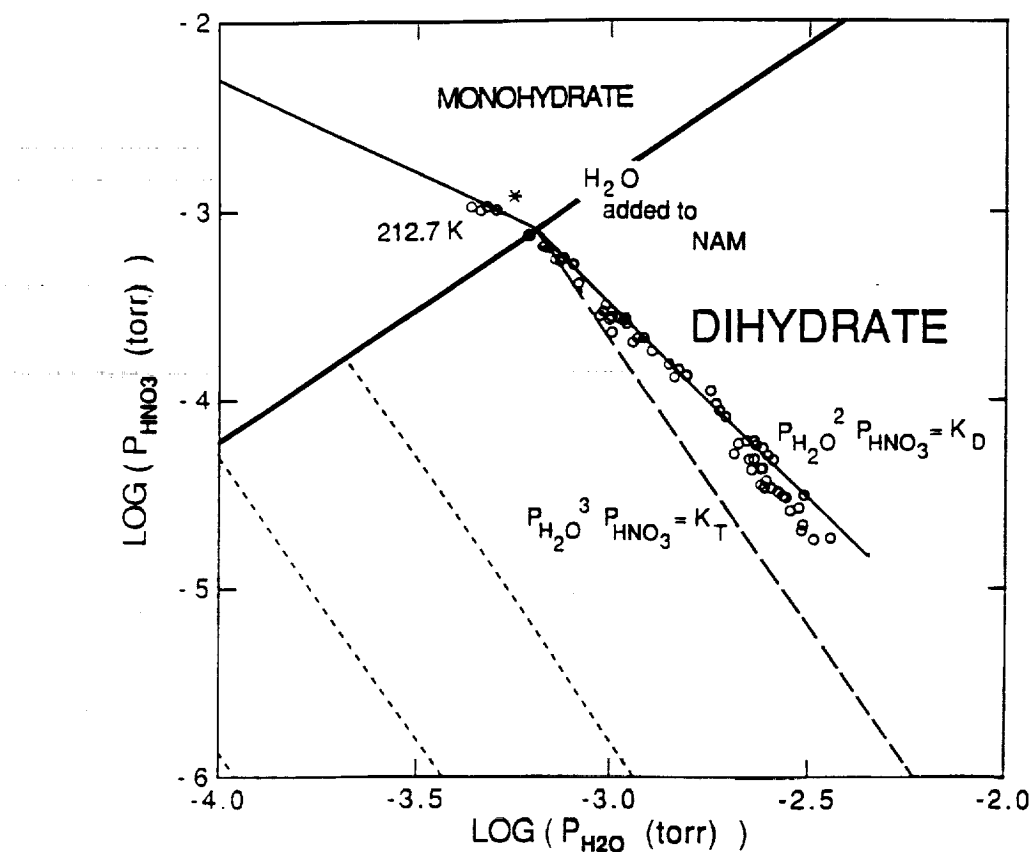


Figure 4.10. $\text{HNO}_3/\text{H}_2\text{O}$ Vapor Pressure at 213 K as a Function of Repeated Water Additions to NAM Sample (Labeled by *). Vapor pressures fall along a line of slope 1/2, corresponding to a dihydrate (NAD) phase. Further H_2O vapor addition (not shown) led to NAT equilibrium (as in Figure 3.3), since HNO_3 supersaturation (~10) was sufficient to nucleate NAT.

initially condensed on the surface. This behavior is typical of physical systems with significant free energy barriers to phase nucleation.

These results can be summarized as follows:

- (1) At least under laboratory conditions, non-equilibrium behavior is typically observed for $\text{HNO}_3/\text{H}_2\text{O}$ solid mixtures. For example, though not explicitly discussed above, the data indicates that surface and interior of solid samples are not equilibrated with the vapor conditions. Equilibration times of days for ~5 mm thick samples correspond to solid diffusion coefficients on the order of $10^{-13} \text{ cm}^2 \text{ s}^{-1}$.
- (2) Supersaturation factors of ~5-10 in HNO_3 vapor are required for nucleation of NAT over ice, NAM and NAD surfaces. This is consistent with Arctic observations of apparent HNO_3 supersaturation. The key question is whether similar behavior is true for H_2SO_4 surfaces (liquid or solid) that occur in the stratosphere.

- (3) Nitric acid dihydrate (NAD) is unstable with respect to NAT under stratospheric conditions. We have observed NAD at $T = 214$ K, but find no evidence that NAD is stable under stratospheric conditions. This indicates that the NAD crystalline phase observed via FTIR spectroscopy of thin films (Ritzhempt and Devlin, 1991; Koehler et al., 1991) probably does not occur in the stratosphere.
- (4) Under stratospheric conditions the equilibrium phase of the $\text{HNO}_3/\text{H}_2\text{O}$ system is pure NAT (or NAT/ice mixtures for $T \leq 190$ K), consistent with the thermodynamics implied by the K_T vapor pressure relation. Based on our observation of slow solid phase diffusion, we believe earlier reports of "water rich" NAT samples (Hanson and Mauersberger, 1988b) came from non-equilibrated solid samples.

RELEVANCE OF EXPERIMENTAL RESULTS TO STRATOSPHERIC FLIGHT

The overall goal for the HSRP program is to integrate variations in aerosol composition and distribution with the heterogeneous reaction chemistry represented by R1-R6.

The growing diversity of aerosol observations and apparent complexity of NAT nucleation is very relevant to the modeling of potential chemical perturbations due to aircraft emissions. Those emissions are projected to occur in the center of the background sulfate layer. Especially at lower temperatures at lower altitudes (< 20 km) near the tropopause and at higher latitudes in the winter, emission of H_2O vapor and condensation nuclei could significantly enhance aerosol formation, since background conditions there are already very close to NAT condensation predictions (Hamill and Fiocco, 1988). Combined with reports of possible observation of local ozone perturbations due to direct interaction with Arctic and Antarctic aerosols (Hofmann, 1989; Hofmann et al., 1989; Fiocco et al., 1989), it is important to quantitatively understand the vapor pressure diagrams for prediction of aerosol formation and growth.

Finally, it is also important to extend these vapor pressure measurements to trace vapor pressures over aerosol solutions containing $\text{HCl}/\text{H}_2\text{O}/\text{HNO}_3/\text{H}_2\text{SO}_4$. The measurements of Hanson and Mauersberger (1988c, 1989) of HCl solubility in ice and NAT solutions are indicative of the difficult nature of these experiments. These measurements are directly relevant to heterogeneous reactions such as R5-R6. To some extent, at higher temperatures these solubility measurements can provide important overlap with uptake experiments described in the previous section.

REFERENCES

Baldwin, A.C. and Golden, D.M., "Heterogeneous Atmospheric Reactions: Sulfuric Acid Aerosols as Tropospheric Sinks," *Science* 206, 562 (1979).

Brimblecombe, P. and Clegg, S.L., "The Solubility and Behavior of Acid Gases in the Marine Aerosol," *J. Atmos. Chem.* 7, 1 (1989).

Bromwich, D.H., "Snowfall in High Southern Latitudes," *Reviews of Geophys.* 26, 1 (1988).

Brune, W., "ClO Measurements in the Arctic Stratosphere," presentation at the CMA Flourocarbon Science Meeting, Stresa, April, 1989.

Chameides, W.L., "The Photochemistry of A Remote Marine Stratiform Cloud," *J. Geophys. Res.* 89, 4739 (1984).

Dye, J.E., Baumgardner, D., Gandrud, B.W., Kawa, S.R., Kelly, K.K., Loewenstein, M., Ferry, G.V. and Gary, B.L., "Particle Size Distributions in Arctic Polar Stratospheric Clouds: Growth and Nucleation of Sulfuric Acid Droplets and Implications for Cloud Formation," submitted to *J. Geophys. Res.* (1991).

Fahey, D.W., "Evidence of HNO_3 Condensation and Denitrification in the Winter Polar Stratosphere From Measurements of NO and NO_y ," presentation at the CMA Flourocarbon Science Meeting, Stresa, April, 1989.

Fahey, D.W., Kelly, K.K., Ferry, G.V., Poole, L.R., Wilson, J.C., Murphy, D.M., Loewenstein, M. and Chan, K.R., "In Situ Measurements of Total Reactive Nitrogen, Total Water, and Aerosol in a Polar Stratospheric Cloud in the Antarctic," *J. Geophys. Res.* 94, 11, 299 (1989).

Fiocco, Giorgio, Komhyr, W.D., and Fua, D., "Is Ozone Destroyed During the Antarctic Winter in the Presence of Polar Stratospheric Clouds?," *Nature*, 341, 426 (1989).

Hamill, P., and Fiocco, G., "Nitric Acid Aerosols at the Tropical Tropopause," *J. Geophys. Res.* 15, 1189-1192, 1988.

Hanson, D., and Mauersberger, "Laboratory Studies of the Nitric Acid Trihydrate Implications for the South Polar Stratosphere," *Geophys. Res. Lett.* 15, 855-858, (1988a).

Hanson, D., and Mauersberger, "Vapor Pressures of $\text{HNO}_3/\text{H}_2\text{O}$ Solutions at Low Temperatures," *J. Phys. Chem.* 92, 6167-6170 (1988b).

Hanson, D., and Mauersberger, "Solubility and Equilibrium Vapor Pressures of HCl Dissolved in Polar Stratospheric Cloud Materials: Ice and The Trihydrate of Nitric Acid," *J. Geophys. Res. Lett.* 15, 1507-1510 (1988c).

Hanson, D.R., and Mauersberger, K., "HCl/ H_2O Solid Phase Vapor Pressures and HCl Solubility in Ice," *J. Phys. Chem.* 94, 4700 (1990).

Harker, A.B. and Strauss, D.R., "Kinetics of the Heterogeneous Hydrolysis of Dinitrogen Pentoxide Over the Temperature Range 214-263 K," Rockwell International Science Center, Federal Aviation Administration Publication FAA-EE-81-3 (1981).

Hofmann, D.J., "Balloon-Borne Measurements of Middle Atmosphere Aerosols and Trace Gases in Antarctica (Paper 8R0029)," *Reviews of Geophys.* 26, 1 (1988).

Hofmann, D.J., "Direct Ozone Depletion in Springtime Antarctic Lower Stratospheric Clouds," *Nature*, Vol. 337, (1989).

Hofmann, D.J., Deshler, T.L., Aimedieu, P., Matthews, W.A., Johnston, P.V., Kondo, Y., Sheldon, W.R., Byrne, G.J., and Benbrook, J.R., "Stratospheric Clouds and Ozone Depletion in the Arctic During January 1989," *Nature*, Vol. 340, (1989a).

Hofmann, D.J., Rosen, J.M., Harder, J.W., and Hereford, J.V., "Balloon-Borne Measurements of Aerosol, Condensation Nuclei, and Cloud Particles in the Stratosphere at McMurdo Station, Antarctica, During the Spring of 1987," *J. Geophys. Res.* 94, 11,253 (1989b).

Hofmann, D.J., and Solomon, S., "Ozone Destruction Through Heterogeneous Chemistry Following the Eruption of El Chichon," *J. Geophys. Res.* 94, 5029 (1989).

Isaksen, I.S.A., "Modeling the Heterogeneous Chemistry of the Junge Layer Aerosols," presentation at the CMA Flourocarbon Science Meeting, Stresa, April, 1989.

Jacob, D.J., "Chemistry of OH In Remote Clouds and Its Role In the Production of Formic Acid and Peroxymonosulfate," *J. Geophys. Res.* 91, 9807 (1986).

Jayne, J.T., Davidovits, P., Worsnop, D.R., Zahniser, M.S., and Kolb, C.E., "Uptake of $\text{SO}_2(\text{g})$ by Aqueous Surfaces As a Function of pH: The Effect of Chemical Reaction at the Interface," *J. Phys. Chem.* 94, 6041 (1990).

Kawa, S.R., Fahey, D.W., Heidt, L.E., Solomon, S., Anderson, D.E., Loewenstein, M., Proffitt, M.H., Margitan, J.J. and Chan, K.R., "Photochemical Partitioning of the Reactive Nitrogen and Chlorine Reservoirs in the High Latitude Stratosphere," *J. Geophys. Res.* 97, 7905 (1992).

Kawa, S.R., Fahey, D.W., Kelly, K.K., "The Arctic Polar Stratospheric Cloud Aerosol: Aircraft Measurements of Reactive Nitrogen, Total Water, and Particles," *J. Geophys. Res.* 97, 7925 (1992).

Ko, M.K.W., Rodriguez, J.M., Sze, N.D., Profitt, M.H., Starr, W.L., Krueger, A., Browell, E.V., and McCormick, M.P., "Implications of AAOE Observations for Proposed Chemical Explanations of the Seasonal and Interannual Behavior of Antarctic Ozone," *J. Geophys. Res.*, 94, 16,705 (1989).

Koehler, B.G., Middlebrook, A.M. and Tolbert, M.A., "Characterization of Model Polar Stratospheric Cloud Films Using Fourier Transform Infrared Spectroscopy and Temperature Programmed Desorption," *J. Geophys. Res.* 97, 8065 (1992).

Leu, M.T., "Laboratory Studies of Sticking Coefficients and Heterogeneous Reactions Important in the Antarctic Stratosphere," *Geophys. Res. Lett.* 15, 17 (1988a).

Leu, M.T., "Heterogeneous Reactions of N_2O_5 with H_2O and HCl on Ice Surfaces: Implications for Antarctic Ozone Depletion," *Geophys. Res. Lett.*, 15, 851 (1988b).

McCormick, M.P., Steele, H.M., Hamill, P., Chu, W.P., and Swissler, T.J., "Polar Stratospheric Cloud Sightings by SAM II," *J. Atmos. Sci.*, 39, 1387-1397 (1982).

McCormick, M.P., "Aerosols and PSCs," presentation at the CMA Flourocarbon Science Meeting, Stresa, April, 1989.

McCormick, M.P., and Trepte, C.R., "SAM II Measurements of Antarctic PSCs and Aerosols," *Geophys. Res. Lett.*, 13, 1276-1279 (1986).

McElroy, M.B., Salawitch, R.J., and Wofsy, S.C., "Antarctic O_3 : Chemical Mechanisms for the Spring Decrease," *Geophys. Res. Lett.* 13, 1296 (1986a).

McElroy, M.B., Salawitch, R.J., Wofsy, S.C., and Logan, J.A., "Reductions of Antarctic Ozone Due to Synergistic Interactions of Chlorine and Bromine," *Nature*, 321, 759-762 (1986b).

McManus, J.B. and P.L. Kebabian, "Narrow Optical Interference Fringes for Certain Setup Conditions in Multipass Absorption Cells of the Herriott Type," *App. Optics* 29, 898 (1990).

Molina, M.J., Tso, T-L., Molina, L.T., and Wang, F.C-Y., "Antarctic Stratospheric Chemistry of Chlorine Nitrate, Hydrogen Chloride, and Ice: Release of Active Chlorine," *Science* 238, 1253 (1987).

Moore, S.B., Keyser, L.F., Leu, T-T. Turco, R.P., and Smith, R.H., "Heterogeneous Reactions on Nitric Acid Trihydrate," *Nature* 345, 333 (1990).

Mozurkewich, M. and Calvert, J.G., "Reaction Probability of N_2O_5 on Aqueous Aerosols," *J. Geophys. Res.* 93, 15889 (1988).

Parker, V.B., "Heats of Solution," in Handbook of Chemistry and Physics, 67th Edition, CRC Press, Inc. (Boca Raton), 1986, p. D-122.

Quinlan, M.A. Reihs, C.M., Golden, D.M., and Tolbert, M.A., "Heterogeneous Reactions on Model Polar Stratospheric Cloud Surfaces: Reaction of N_2O_5 on Ice and Nitric Acid Trihydrate," *J. Phys. Chem.* 94, 3255 (1990).

Reihs, C.M., Golden, D.M., and Tolbert, M.A., "Nitric Acid Uptake by Sulfuric Acid Solutions Under Stratospheric Conditions: Determination of Henrys Law Solubility," *J. Geophys. Res.* 95, 16,545 (1990).

Ritzhaupt, G. and Devlin, J.P., "Infrared Spectra of Nitric and Hydrochloric Acid Hydrate Thin Films," *J. Phys. Chem.* 95, 90-95 (1991).

Rodriguez, J.M., Ko, M.K.W., and Sze, N.D., "Anarctic Chlorine Chemistry: Possible Global Implications," *Geophys. Res. Lett.* 15, 257-260 (1988).

Rochester, C.H., Acidity Functions, Academic Press (New York), 1971.

Rosen, J.M., "The Boiling Point of Stratospheric Aerosols," *J. Appl. Meteorology* 10, 1044 (1971).

Rossi, M.J., Malhotra, R., and Golden, D.M., "Heterogeneous Chemical Reaction of Chlorine Nitrate and Water on Sulfuric Acid Surface at Room Temperature," *Geophys. Res. Lett.* 14, 127 (1987).

Salawitch, R.J., Wofsy, S.C. and McElroy, M.B., "Influence of Polar Stratospheric Clouds on the Depletion of Antarctic Ozone," *Geophys. Res. Lett.* 15, 871 (1988).

Schwartz, S.E., "Mass-Transport Considerations Pertinent to Aqueous Phase Reactions of Gases in Liquid-Water Clouds," in Chemistry of Multiphase Atmospheric Systems, NATO ASI Series, Vol. G6, ed. W. Jaeschke, Springer-Verlag (New York), pp 415-471 (1986).

Schwartz, S.E., "Mass Transport Limitation To the Rate of In-Cloud Oxidation of SO₂: Re-Examination In the Light of New Data," *Atm. Env.* 22, 2491 (1988).

Schwartz, S.E. and Freiberg, J.E., "Mass Transport Limitation to the Rate of Reaction of Gases in Liquid Droplets: Application to Oxidation of SO₂ in Aqueous Solutions," *Atmos. Environ.* 15, 1129 (1981).

Solomon, S., "The Mystery of the Antarctic Ozone Hole," *Reviews of Geophys.* 26, 1 (1988).

Steele, H.M., Hamill, P., McCormick, M.P., and Swissler, T.J., "The Formation of Polar Stratospheric Clouds," *J. Atmos. Sci.* 40, 2055 (1983).

Stormer, C., "Remarkable Clouds at High Altitudes," *Nature*, 123, 260-261 (1929).

Tolbert, M.A., Rossi, M.J., Malhotra, R., and Golden, D.M., "Reaction of Chlorine Nitrate with Hydrogen Chloride and Water at Antarctic Stratospheric Temperatures," *Science* 238, 1258 (1987).

Tolbert, M.A., Rossi, M.J., and Golden, D.M., "Anarctic Ozone Depletion Chemistry: Reactions of N₂O₅ with H₂O and HCl on Ice Surfaces," *Science* 240, 1018-1021 (1988a).

Tolbert, M.A., Rossi, M.J., and Golden, D.M., "Heterogeneous Interactions of ClONO₂, HCl, and HNO₃ with Sulfuric Acid Surfaces at Stratospheric Temperatures," *Geophys. Res. Lett.* 15, 847 (1988b). Values recently revised, Tolbert, M.A. (1989).

Toon, O.B., Turco, R.P., Jordan, J., Goodman, J. and Ferry G., "Physical Processes in Polar Stratospheric Ice Clouds," *J. Geophys. Res.* 94, 11,359 (1989).

Turco, Richard P., Toon, Owen, B., and Hamill, P., "Heterogeneous Physicochemistry of the Polar Ozone Hole," *J. Geophys. Res.* 94, 16, 493 (1989).

Turco, Richard P., Toon, Owen, B., and Hamill, P., "Effects of meteoric Debris on Stratospheric Aerosols and Gases," *J. of Geophys. Res.* 86, C2 (1981).

Van Doren, J.M., Watson, L.R., Davidovits, P., Worsnop, D.R., Zahniser, M.S., and Kolb, C.E., "Temperature Dependence of the Uptake Coefficient for HCl, HNO₃, and N₂O₅ On Water Droplets," *J. Phys. Chem.*, 94, 3265 (1990).

Van Doren, J.M., Watson, L.R., Davidovits, P., Worsnop, D.R., Zahniser, M.S., and Kolb, C.E., "Uptake of N_2O_5 and HNO_3 by Aqueous Sulfuric Acid Droplets," *J. Phys. Chem.* 95, 1684 (1991).

Watson, L., Van Doren, J.M., Davidovits, P., Worsnop, D., Zahniser, M.S., and Kolb, C.E., "Uptake of HCl Molecules By Aqueous Droplets As a Function of Sulfuric Acid Concentration," *J. Geophys. Res.* 95, 5631 (1990).

Weisenstein, D., Ko, M., Sze, Nien-Dak, Rodriguez, and Knowlton, L., "Sensitivity of Ozone Response to Aircraft Emissions in the Future Atmosphere: A 2-D Model Assessment," presented at HSRP HSCT Annual Meeting, Virginia Beach, January 1991.

Wolff, E.W., Mulvaney, R., and Oates, K., "Diffusion and Location of Hydrochloric Acid In Ice, "Implications for Polar Stratospheric Clouds and Ozone Depletion," *Geophys. Res. Lett.* 16, 487-490 (1989).

Wofsy, S.C., Salawitch, R.J., Yatteau, J.H. McElroy, M.B., Gandrud, B.W., Dye, J.E. and Baumgardner, D., "Condensation of HNO_3 of Falling Ice Particles: Mechanisms for Denitrification of the Polar Stratosphere," *Geophys. Res. Lett.* 17, 449-452, (1990).

Worsnop, D.R., Zahniser, M.S., Kolb, C.E., Gardner, J.A., Watson, L.R., Van Doren, J.M., Jayne, J.T., and Davidovits, P., "The Temperature Dependence of Mass Accommodation of SO_2 and H_2O_2 On Aqueous Surfaces," *J. Phys. Chem.* 93, 1159 (1989).

Worsnop, D.R., Fox, L.E., Zahniser, M.S., and Wofsy, S.C., "Vapor Pressures of Nitric Acid Hydrates: Implications for Stratospheric Clouds," *Science*, in press (1992).

REPORT DOCUMENTATION PAGE

Form Approved
OMB No 0704-0188

Pub. Report 2020. The burden of information is estimated to average 1 hour per response, including the time for reviewing instructions, searching existing data sources, gathering and maintaining the data needed, and completing and reviewing the collection of information. Send comments regarding this burden estimate or any other aspect of the collection of information, including suggestions for reducing this burden, to: Westover Headquarters Services Directorate for Information Operations and Reports, 1215 Jefferson Davis Highway, Suite 1274, Arlington, VA 22202-4102, and to the Office of Management and Budget, Paperwork Reduction Project (0704-0188), Washington, DC 20503.

1. AGENCY USE ONLY (Leave blank)	2. REPORT DATE	3. REPORT TYPE AND DATES COVERED	
	October 1992	Contractor Report	
4. TITLE AND SUBTITLE Stratospheric Aircraft Exhaust Plume and Wake Chemistry Studies		5. FUNDING NUMBERS C NAS1-19161 WU 537-01-20-01	
6. AUTHOR(S) R.C. Miake-Lye, M. Martinez-Sanchez, R.C. Brown C.E. Kolb, D.R. Worsnop, M.S. Zahniser, G.N. Robinson, J.M. Rodriguez, M.K.W. Ko, R-L. Shia, N.D. Sze, L. Fox, S.C. Wofsy and P. Davidovits		8. PERFORMING ORGANIZATION REPORT NUMBER ARI-RR-902	
7. PERFORMING ORGANIZATION NAME(S) AND ADDRESS(ES) Aerodyne Research, Inc. 45 Manning Road Billerica, MA 01821		10. SPONSORING / MONITORING AGENCY REPORT NUMBER NASA CR-189688	
9. SPONSORING / MONITORING AGENCY NAME(S) AND ADDRESS(ES) National Aeronautics and Space Administration Langley Research Center Hampton, VA 23665-5225		11. SUPPLEMENTARY NOTES Langley Technical Monitor: William L. Grose	
12a. DISTRIBUTION / AVAILABILITY STATEMENT Unclassified-Unlimited Subject Category 46		12b. DISTRIBUTION CODE	
13. ABSTRACT (Maximum 200 words) This report documents progress to date in an ongoing study to analyze and model emissions leaving a proposed High Speed Civil Transport (HSCT) from when the exhaust gases leave the engine until they are deposited at atmospheric scales in the stratosphere. Estimates are given for the emissions, summarizing relevant earlier work (CIAP) and reviewing current propulsion research efforts. The chemical evolution and the mixing and vortical motion of the exhaust are analyzed to track the exhaust and its speciation as the emissions are mixed to atmospheric scales. The species tracked include those that could be heterogeneously reactive on the surfaces of the condensed solid water (ice) particles and on exhaust soot particle surfaces. Dispersion and reaction of chemical constituents in the far wake are studied with a Lagrangian air parcel model, in conjunction with a radiation code to calculate the net heating/cooling. Laboratory measurements of heterogeneous chemistry of aqueous sulfuric acid and nitric acid hydrates are also described. Results include the solubility of HCl in sulfuric acid which is a key parameter for modeling stratospheric processes. We also report initial results for condensation of nitric acid trihydrate from gas phase H ₂ O and HNO ₃ .			
14. SUBJECT TERMS Stratospheric chemistry, Ozone, Aircraft emissions, Stratospheric aircraft, High-speed civil transport, Contrail, Vortex wake			15. NUMBER OF PAGES 105
			16. PRICE CODE
17. SECURITY CLASSIFICATION OF REPORT Unclassified	18. SECURITY CLASSIFICATION OF THIS PAGE Unclassified	19. SECURITY CLASSIFICATION OF ABSTRACT Unclassified	20. LIMITATION OF ABSTRACT